



저작자표시-비영리-변경금지 2.0 대한민국

이용자는 아래의 조건을 따르는 경우에 한하여 자유롭게

- 이 저작물을 복제, 배포, 전송, 전시, 공연 및 방송할 수 있습니다.

다음과 같은 조건을 따라야 합니다:



저작자표시. 귀하는 원저작자를 표시하여야 합니다.



비영리. 귀하는 이 저작물을 영리 목적으로 이용할 수 없습니다.



변경금지. 귀하는 이 저작물을 개작, 변형 또는 가공할 수 없습니다.

- 귀하는, 이 저작물의 재이용이나 배포의 경우, 이 저작물에 적용된 이용허락조건을 명확하게 나타내어야 합니다.
- 저작권자로부터 별도의 허가를 받으면 이러한 조건들은 적용되지 않습니다.

저작권법에 따른 이용자의 권리는 위의 내용에 의하여 영향을 받지 않습니다.

이것은 [이용허락규약\(Legal Code\)](#)을 이해하기 쉽게 요약한 것입니다.

[Disclaimer](#)

이학박사 학위논문

Unfolding the folding mystery:
How chaperonins shape the
protein folding pathway

샤페로닌 TRiC/CCT에 의한 단백질 접힘의
구조적 연구

2025년 2월

서울대학교 대학원

생명과학부 구조생물학 전공

박준선

Unfolding the folding mystery: How chaperonins shape the protein folding pathway

지도 교수 노 성 훈

이 논문을 이학박사 학위논문으로 제출함
2025년 2월

서울대학교 대학원
생명과학부 구조생물학 전공
박 준 선

박준선의 이학박사 학위논문을 인준함
2025년 2월

위원장 최 희 정 (인)

부위원장 노 성 훈 (인)

위원 윤 태 영 (인)

위원 고 준 석 (인)

위원 신 동 혁 (인)

Abstract

Unfolding the folding mystery: How chaperonins shape the protein folding pathway

Junsun Park

Department of biological sciences

The Graduate School

Seoul National University

Protein folding is a key process for maintaining cellular proteostasis, and molecular chaperones play a crucial role in ensuring proper folding. However, due to the heterogeneity and complexity of the folding process, studying the chemistry of protein folding and the roles of molecular chaperones at the molecular level remains extremely challenging. In this study, I aim to structurally investigate the mechanisms of protein folding assisted by the molecular chaperonin TRiC/CCT (or TRiC) and its cochaperones.

The folding process mediated by chaperonin TRiC can be divided into three major stages: substrate delivery, cochaperone cooperation, and substrate folding. The reconstitution of each folding process *in vitro* and subsequent cryo-EM heterogeneity analysis shed a light on resolving the structural dynamics of the complex. During substrate delivery, prefoldin (PFD) hands off the substrate to the central chamber of TRiC. In the cochaperone cooperation stage, PhLP2A cooperates with TRiC, undergoing large relocations upon ATP-dependent cycle. In the substrate folding stage, substrate folding is guided by domain-specific interactions between TRiC subunits and the substrate. Additionally, PhLP2A provides extra interactions with the substrate in the folding chamber, engaging in the folding process.

Collectively, through this study, I have elucidated the structural dynamics of TRiC and cochaperones, contributing to the understanding of the substrate folding mechanisms.

Keyword : Cryo-EM, Protein folding, chaperone network, structural biology

Student Number : 2019-29532

Table of Contents

Chapter 1. Introduction	1
1. 1. Study Background	1
1. 1. 1. Protein folding and Anfinsen’s dogma	1
1. 1. 2. Chaperones and Chaperonin	2
1. 1. 3. Chaperonin TRiC in eukaryotes	4
1. 1. 4. Asymmetric structural characteristics of TRiC	5
1. 1. 5. ATP-driven asymmetric conformational changes of TRiC	6
1. 1. 6. Substrate recognition by TRiC	7
1. 1. 7. Substrate delivery by co-chaperone PFD.....	7
1. 1. 8. Identified substrates for TRiC.....	8
1. 1. 9. Previous studies for substrate folding mediated by TRiC	9
1. 1. 10. Co-chaperone PhLP families and substrate folding..	11
1. 2. Purpose of Research	20
1. 2. 1. Limitation of previous research and unanswered questions.....	20
1. 2. 2. Significance and application.....	21
Chapter 2. Method	24
2. 1. Cryo-EM of TRiC, co-chaperone, substrate complex	24
2. 1. 1. Cryo-EM of grid preparation and data collection.....	24
2. 1. 2. Cryo-EM data processing.....	28
2. 1. 3. Atomic model building and Refinement.....	33
2. 2. Interaction mapping and AlphaFold prediction	35
2. 3. Sequence alignment and evolutionary analysis	35

Chapter 3. Result	38
3. 1. Structural study of substrate delivery to TRiC	38
3. 1. 1. Structural analysis of substrate-free apo open TRiC	38
3. 1. 2. Structural analysis of PFD: β -actin:TRiC complex.....	39
3. 2. Structural study of co-chaperone PhLP family and TRiC...48	
3. 2. 1. Structural analysis of PhLP2A and open TRiC	48
3. 2. 2. Structural analysis of PhLP1 and open TRiC	49
3. 2. 3. Structural analysis of PhLP2B and open TRiC	50
3. 2. 4. Structural analysis of PhLP2A and closed TRiC.....	51
3. 2. 5. Structural analysis of PhLP2A, PFD and TRiC complex	53
3. 2. 6. Structural analysis of truncated PhLP2A upon ATP cycle of TRiC	54
3. 3. Structural study of TRiC for substrate folding	79
3. 3. 1. Structural analysis of substrate-free apo closed TRiC	79
3. 3. 2. Structural analysis of closed β -tubulin TRiC complex	79
3. 3. 3. Folding intermediates guided by TRiC subunits.....	81
3. 3. 4. Evolutionary analysis of TRiC dependent substrate folding	83
3. 4. Structural study of co-chaperone and TRiC cooperation for substrate folding	97
3. 4. 1. Structural analysis of PhLP2A, substrate and TRiC ...	97
3. 4. 2. Evolutionary analysis of PhLPs and TRiC for substrate folding.....	98
Chapter 4. Conclusion.....	107
4. 1. Structural study of TRiC for substrate folding	107

4. 1. 1. The proposed mechanism of substrate delivery to TRiC folding	107
4. 1. 2. The proposed mechanism of substrate folding without co-chaperones	107
4. 1. 3. The proposed mechanism of substrate folding with co-chaperones	109
4. 2. Cooperation of TRiC and co-chaperones for proteomic complexities.....	110
4. 3. Structural comparison of TRiC mediated folding pathway among different substrates	110
4. 4. Future direction.....	112
 Bibliography.....	 119
 Abstract in Korean.....	 132

List of Figures

Figure 1.1 Free energy landscape of protein folding.

Figure 1.2 Protein folding assisted by chaperone network.

Figure 1.3 Structural architecture of Group I and Group II chaperonin.

Figure 1.4 Structure of TRiC and ATP-driven structural change.

Figure 1.5 Substrate recognition and delivery to TRiC.

Figure 1.6 Identified obligate substrates of TRiC.

Figure 1.7 TRiC-mediated substrate folding cycle remains elusive.

Figure 3.1 Cryo-EM workflow for apo-TRiC.

Figure 3.2 Cryo-EM structure of apo TRiC in open conformation.

Figure 3.3 Cryo-EM workflow for prefoldin: β -tubulin-TRiC.

Figure 3.4 Ternary prefoldin: β -tubulin:TRiC complex in the open conformation.

Figure 3.5 Tails and the central cavity of prefoldin: β -tubulin:TRiC complex in the open conformation.

Figure 3.6 Structural analyses on PhLP2A in an open TRiC complex.

Figure 3.7 Cryo-EM structure of the PhLP2A-open TRiC complex.

Figure 3.8 Analyses on ATP binding pocket in an open TRiC-PhLP2A complex.

Figure 3.9 Molecular contacts between PhLP2A and open TRiC chamber.

Figure 3.10 AlphaFold-adopted model building and crosslinking assay of PhLP2A.

Figure 3.11 Cryo-EM structure of open PhLP1-TRiC.

Figure 3.12 Cryo-EM structure of open PhLP2B-TRiC.

Figure 3.13 Cryo-EM structure of PhLP2A in closed TRiC.

Figure 3.14 Analyses on ATP binding pocket in a closed TRiC-PhLP2A complex.

Figure 3.15 Structure of PhLP2A inside TRiC chamber after chamber closing.

Figure 3.16 Relocation of PhLP2A upon ATP dependent TRiC cycle.

Figure 3.17 PhLP2A modulation on the PFD-TRiC network.

Figure 3.18 The direct competition between PFD and PhLP2A.

Figure 3.19 Domain-wise characteristics of PhLP2A in relationship with TRiC.

Figure 3.20 Cryo-EM processing workflow of truncated PhLP2A :TRiC complex.

Figure 3.21 Cryo-EM structure of apo closed TRiC.

Figure 3.22 Cryo-EM workflow and analysis for TRiC: β -tubulin.

Figure 3.23 Cryo-EM identifies β -tubulin folding intermediates in ATP-driven closed TRiC chamber.

Figure 3.24 TRiC and β -tubulin interaction in a domain-specific manner.

Figure 3.25 TRiC chamber spatially orients and restrains β -tubulin.

Figure 3.26 The directed folding of β -tubulin intermediates by specific CCT interactions.

Figure 3.27 Evolutionary analysis and the directed folding of β -tubulin intermediates.

Figure 3.28 Tubulin coevolved with TRiC for directed folding process.

Figure 3.29 Cryo-EM structure of PhLP2A-actin encapsulated closed TRiC.

Figure 3.30 Cryo-EM structure of closed TRiC with folded actin and PhLP2A.

Figure 3.31 Conservation on phosducin-like protein family and the proposed mechanism of chaperone-in-chaperonin mediated folding

cycle.

Figure 3.32 Evolutionary analysis on phosphatidylethanolamine transferase-like protein family.

Figure 4.1 Proposed mechanism of chaperonin TRiC mediated folding pathway.

Figure 4.2 Mechanism of TRiC and cochaperone PhLP2A mediated substrate folding pathway.

Figure 4.3 Substrate-specific interaction in the TRiC folding chamber.

List of Table

Table 1. Cryo-EM image collection, map reconstruction, and model refinement (Tubulin related).

Table 2. Cryo-EM image collection, map reconstruction, and model refinement (PhLP2A related).

Chapter 1. Introduction

1.1. Study Background

1. 1. 1 Protein folding and Anfinsen' s dogma

Protein folding is the process by which the newly translated nascent polypeptide adopts its native 3D structure to become biologically functional. There are about ~20,000 human protein-coding genes identified¹⁻³, and each protein adopts its unique 3D structures. The correct 3D structures of proteins are fundamental for proper function. Protein misfolding can lead to loss of function and cellular toxicity, encompassing conditions from cancer to neurodegenerative disorders such as Alzheimer' s and Parkinson' s disease⁴⁻⁷. Thus, the process of protein folding in living organisms is crucial for proteostasis and maintenance of proteome balance. Yet, understanding protein folding remains a central enigma in the field of biology.

The protein folding problem emerged in the 1950-1960s. Levinthal noted that the number of possible 3D structures that a nascent chain can adopt is extremely large to arrive at its correct native conformation. For instance, a nascent chain composed of around 100 amino acids can theoretically adopt more than 10^{30} conformations, making protein folding a highly complicated process (Levinthal' s paradox)⁸. The fundamental insight into protein folding was provided by Anfinsen, who proposed the thermodynamic hypothesis, or Anfinsen's dogma. He showed small protein refold spontaneously *in vitro*, stating that the native structure of a protein is determined by its amino acid sequence and that proteins can spontaneously fold without the aid⁹. Nowadays, protein folding is understood to be driven by various noncovalent interactions and hydrophobic forces. Importantly, the collapse of the hydrophobic core and the burial of nonpolar amino acids leads to entropic stabilization, helping the protein achieve its native, functional structure.

The widely accepted concept of protein folding is explained by the free-energy landscape model, where the vertical axis represents the protein's free energy, and the horizontal axis represents the diversity of protein conformations. The typical energy landscape of protein shows a funnel-shaped energy landscape^{10,11}. Higher positions on the vertical axis indicate higher free energy, and the protein can adopt a wide variety of conformations (Figure 1.1a). As the protein moves downward along the landscape, both the free energy and the number of conformations decrease, eventually reaching the native structure which is energetically most stable state.

The simplest form of protein folding follows a smooth funnel shape, which aligns with Anfinsen's dogma. However, in reality, certain proteins have complex structures and often challenged by structural frustration, leading to a rugged funnel shape (Figure 1.1b). Therefore, for proteins to reach their native state, they must overcome substantial kinetic energy barriers. In many cases, they become trapped in local energy minima. In such cases, the protein may partially fold, or misfold or aggregate, becoming energetically trapped in an intermediate state, preventing it from reaching the native state¹².

1. 1. 2 chaperones and chaperonin

Certain proteins, due to various kinetic reasons, cannot spontaneously fold and require assistance from molecular chaperone machinery (Figure 1.2a). Since the 1980s, the role of chaperones has been extensively studied, revealing that they interact with proteins to help them achieve a functionally active conformation^{12,13}. Key chaperones involved in de novo folding include the Hsp60, Hsp70, and Hsp90 systems, which are highly conserved and form a cooperative network to assist folding^{14,15} (Figure 1.2b). These chaperones promote substrate folding through ATP-dependent mechanisms. During the ATP-regulated cycles, chaperones recognize exposed hydrophobic residues to prevent aggregation¹⁶ and rescue misfolded proteins, to achieve their native state.

Among chaperone networks, chaperonins, or Hsp60, are large multisubunit complexes with a molecular weight of around ~1 MDa. Typically, chaperonins consist of two ring structures stacked back-to-back, forming a cylindrical nano-cage with a central cavity^{17,18}. Chaperonins are also known as the Anfinsen cage as they provide a secluded environment to prevent aggregation, offering a favorable environment for protein folding. Chaperonins are classified into Group I and Group II. Group I chaperonins include bacterial cytosol chaperonin (GroEL), mitochondrial chaperonin (Hsp60), and chloroplast chaperonin (Cpn60). Group II chaperonins include archaeal chaperonin (Thermosome) and eukaryotic chaperonin (TRiC/CCT).

The most extensively studied Group I chaperonin is the bacterial GroEL, which is involved in the folding of approximately 10% of the *E. coli* proteome^{17,19}. GroEL consists of seven 60 kDa subunits forming one ring, with two rings connected to form a 14-subunit structure (Figure 1.3a). It works in cooperation with GroES, a lid-shaped cofactor composed of seven 10 kDa subunits that binds to either end of GroEL, completing the isolated chamber. GroEL subunits are divided into three domains: apical, intermediate, and equatorial¹⁹. The subunit of GroEL has ATPase activity and ATP cycle takes about 2 seconds²⁰. ATP binding induces a conformational change in GroEL subunits, promoting GroES binding to the apical domain of the GroEL subunit^{21,22}. GroEL subunits are allosterically regulated²², and the apical domain specifically recognizes hydrophobic residues, promoting substrate binding. GroEL can act passively by preventing aggregation during substrate folding, but many studies have also suggested that it plays an active role in facilitating substrate folding by unfolding mechanism^{23,24} and exhibits direct binding to the negatively charged chamber²⁵. Unlike GroEL and mitochondrial Hsp60, chloroplast chaperonin Cpn60 forms a hetero-oligomeric complex with multiple subunits²⁶.

Group II chaperonins are primarily found in archaea and the eukaryotic cytosol. They consist of two stacked rings, each composed of eight subunits, with molecular weights ranging from 50

to 60 kDa^{18,27-30}. Group II chaperonins are often hetero-oligomers, such as the thermosome, which consists of alpha and beta subunits. Like Group I chaperonins, their subunits are divided into apical, intermediate, and equatorial domains (Figure 1.3b). However, Group II chaperonins differ in that they have a built-in lid mechanism, a long helical protrusion in the apical domain, which allows them to close the folding chamber without the need for an external co-chaperone like GroES. This inherent lid mechanism enables Group II chaperonins to fold substrates *in vitro* without requiring accessory proteins^{31,32}.

1. 1. 3 Chaperonin TRiC in eukaryotes

The ring-shaped chaperonin TCP-1 ring complex (TRiC/CCT, or TRiC) is a eukaryotic chaperonin known to play a central role in the chaperone network. TRiC supports the folding of approximately 10% of the eukaryotic proteome^{33,34}. Like other chaperonins, TRiC undergoes an ATP-dependent cycle, transitioning between open and closed states to create an isolated environment within its chamber for protein folding. TRiC is particularly associated with various diseases, including neurodegenerative disorders and cancer^{4,6}. Biochemical experiments have shown that TRiC reduces the aggregation of mutant huntingtin exon 1 (mhtt), which is linked to Huntington's disease^{35,36}. Additionally, cryo-tomography studies have revealed that TRiC suppresses the aggregation of amyloid proteins by capping filaments formed by aggregation³⁷ and *in situ* study confirmed TRiC is localized near poly-GA aggregation³⁸. TRiC is also linked to Alzheimer's and Parkinson's diseases^{39,40}.

Furthermore, TRiC is involved in the folding and assembly of viral proteins related to the capsid formation and replication⁴¹⁻⁴³. In cancer, TRiC plays a role in folding of oncoproteins like Von Hippel-Lindau (VHL)⁴⁴, p53⁴⁵, and signal transducer and activator of transcription 3 (STAT3)⁴⁶, all of which are linked to tumor development. Likewise, altered expression levels of TRiC have been reported in various cancer patients⁴⁷. Additionally, TRiC is involved

in the folding of proteins such as cyclin E, B, Cdc20, and Cdh1, indicating that it also has direct and indirect regulatory roles in the cell cycle⁴⁷.

Thus, TRiC plays a highly diverse and central role as a eukaryotic chaperonin *in vivo* and is directly linked to several diseases, making it a crucial regulator in both cellular function and disease pathology.

1. 1. 4 Asymmetric structural characteristics of TRiC

TRiC is a 1 MDa double-ring hexadecane complex and each ring consists of 8 paralogous subunits, CCT1-8, (Figure 1.4a)^{28,30,48}. Although 8 subunits have only a 27-39% varying sequence identity, the general architecture of TRiC subunits shows a distinctive 3-domain structure which is conserved among Group II chaperonin^{18,30}. This architecture includes an apical domain, an intermediate domain, and an equatorial domain (Figure 1.4b). An apical domain contains the substrate recognition site and the lid-forming loop at the top of the subunit. The intermediate domain is positioned in the hinge part, communicating ATP cycling from the equatorial domain to drive movements in the apical domain. The equatorial domain has the ATP-binding site and is involved in the subunit assembly^{44,49-51}.

TRiC has its unique subunit arrangement in both inter-ring and intra-ring arrangement. In light of crystallography⁵²⁻⁵⁵ and cryo-electron microscopy (cryo-EM)^{27,56}, overall architecture and the structural transitions during the ATP cycle (Figure 1.4a) are identified but the low resolution of the structures and the pseudo-symmetry of the complex posed challenges to determine the subunit arrangement and structural analysis. Recent combinatorial structural approaches using crosslinking/mass spectrometry^{30,57} and cryo-EM experiments with additional bulk tags labeled to a specific subunit^{49,58,59} successfully resolved the ambiguities in the subunit arrangement. Each ring follows the identical order of CCT subunits (CCT 2-4-1-3-6-8-7-5). Additionally, CCT6 and CCT2 from one ring are aligned back-to-back with CCT6 and CCT2 from the

opposite ring, making C2 symmetry (Figure 1.4c). This confirmed that TRiC has a fixed subunit arrangement and confirmed by yeast experiments conducted *in vivo*³⁰.

The structural features of TRiC are conserved across eukaryotes, but yeast and mammalian TRiC exhibit slight structural differences. Cryo-EM studies have revealed that in yeast TRiC, the CCT2 subunit is bent, causing the apical domain to attach to CCT5, and together with the CCT2 in the opposite ring, it forms a Z-shaped structure⁵⁸. However, in mammalian TRiC, CCT2 is not bent and extends straight, showing distinct structural features in the apo state in each species (Figure 1.4d).

1. 1. 5 ATP-driven asymmetric conformational changes of TRiC

When ATP binds to TRiC, it induces a more compact and rigid open conformation. Particularly, for yeast TRiC, ATP binding triggers conformational changes in CCT2 and CCT7^{58,60}. Interestingly, the conformational changes of CCT subunits respond differently depending on the concentration of ATP, demonstrating allosteric cooperativity of the CCT subunits upon ATP binding⁶¹. Subsequent ATP hydrolysis leads to a large conformational change in the apical domain, leading to the closure of the lid. In the closed conformation, subunits make tight contacts, forming an isolated chamber for protein folding. The lid closure forms an asymmetric charge distribution on the chamber wall; CCT5-2-4 and CCT3-6-8 create negative and positive hemispheres (Figure 1.4e), which are highly conserved and essential for TRiC function³⁰.

Asymmetric use of ATP is a key feature for the cooperativity of TRiC subunits. Single molecule studies showed that only seven or eight ATP are hydrolyzed at once, potentially indicating uneven hydrolysis of ATP on TRiC subunits⁶². Cryo-EM studies also showed that even in the closed TRiC, ADP occupies the pocket of CCT8 while other subunits exhibit ADP-AlFx meaning that CCT8 did not undergo nucleotide exchange⁶¹. Crosslinking and ATP titration assay

has also revealed a hierarchy of ATP affinity: CCT5/4 showed the highest affinity for ATP followed by CCT1/2 and CCT7/8/6/3 showed low affinities⁶³ (Figure 1.4f). In a similar regard, mutations that hinders ATP binding in the P-loop motif of CCT7/8/6/3 did not show phenotype in yeast. However, mutations in CCT5/4/1/2 lead to the severe phenotypes and even lethal for CCT4⁶³. Taken altogether, the asymmetric use of ATP by TRiC suggests a sequential closure model, starting with the high-affinity CCT subunits (CCT5/4/1/2), and propagates through the remaining subunits.

1. 1. 6 Substrate recognition by TRiC

The principles governing substrate recognition by TRiC remain a subject of limited comprehension. *In vivo*, TRiC is responsible for folding a specific group of cellular proteins, implying a certain degree of specificity. However, the substrates also accommodate various functions and structures, suggesting the potential of the chaperonin to cover a wide spectrum of proteins. The current prevailing hypothesis proposes that individual subunits of TRiC's apical domain are responsible for recognizing specific motifs within the substrates, enabling efficient binding during the folding process⁵⁰. In the apical domain of each CCT subunit, the distinctive patterns of polar and hydrophobic residues serve as the foundation for their unique substrate binding capabilities (Figure 1.5a). This diversification of binding sites offers a flexible framework of binding specificities, facilitating the combinatorial recognition of substrate polypeptides^{34,44}. This unique characteristic likely contributes to TRiC's remarkable ability to fold substrates that are both structurally diverse and highly complex. Moreover, evolutionary analyses indicate that the diversification of TRiC subunits, which sets it apart from its simpler archaeal ancestors, was instrumental in allowing eukaryotic genomes to incorporate proteins with novel folds and functions (Figure 1.5b)⁵⁰.

1. 1. 7 Substrate delivery by co-chaperone PFD

PFD, also known as GimC, is a superfamily of proteins playing key roles for protein folding complexes⁶⁴. PFD is a heterohexameric molecular chaperone complex and is present in both archaea and eukarya, including the human system^{65,66}. The PFD molecule functions as a mediator in substrate delivery, collaborating closely with the TRiC chaperonin to form a functional chaperone complex.⁵⁹ This complex plays a pivotal role in ensuring the proper folding of nascent proteins with precision and accuracy.^{59,67,68} The interaction between PFD and TRiC relies on a conserved electrostatic interface, serving as a pivotal point in the process. This interaction is dynamic, shifting between an "open latched" state and an "engaged" state, ensuring precise alignment of the substrate-binding chambers within both TRiC and PFD. (Figure 1.5c)⁵⁹. Of note, PFD on the TRiC-actin complex significantly increases both the yield and velocity of the actin folding reaction⁵⁹ suggesting certain roles between substrate delivery and folding rate enhancement. However, the substrate delivery mechanism from PFD to TRiC remain an unresolved question.

1. 1. 8 Identified substrates for TRiC

TRiC holds a central role in the chaperone network and is involved in folding around 10% of the entire proteome^{33,34,69}. Mass spectrometry and proteomics studies have shown that many essential proteins exhibit an obligate dependency on TRiC to achieve proper folding^{33,34,69}. These potential clients span a wide range of biological functions, including cytoskeletal proteins, cell cycle regulation, DNA maintenance, replication, repair, metabolism, transcription, translation, RNA processing, cellular trafficking, signal transduction, and several viral proteins⁶⁹.

Many TRiC substrates are complex multidomain proteins with intricate topologies. These proteins often exhibit β -sheet folds prone to aggregation and slow folding kinetics³⁴. Additionally, many have enriched hydrophobic sequences, which contribute to a larger

hydrophobic core³⁴. This suggests that TRiC primarily assists proteins with complex folding pathways arising from their topological challenges.

Most TRiC substrates fall within the 40–75 kDa molecular weight range, aligning with the size of TRiC's internal chamber^{34,52}. Larger proteins, such as myosin II, which exceeds 100 kDa, are also known TRiC substrates³⁴. The most well-studied obligate substrates of TRiC are actin and tubulin, two cytoskeletal proteins that are among the most abundant in cells. In addition, proteins with WD40 beta propeller domains, such as G β ⁷⁰, CSA⁷¹, and WDR68⁷², as well as oncogenic proteins like p53⁴⁵, AML1-ETO⁷³, and STAT3⁴⁶, have also been identified as TRiC substrates. By assisting substrate folding, TRiC indirectly influences a variety of signaling pathways.

While TRiC substrates exhibit some common structural features, such as β -sheet folds and large hydrophobic cores, they do not share a highly conserved topology. For instance, when comparing actin, tubulin, G β , and sigma3, they lack high sequence similarity or identical structural domains (Figure 1.6). This diversity leaves the folding mechanism assisted by TRiC still largely unknown.

Beyond folding, TRiC also regulates the activity of its substrates. It interacts with proteins involved in actin filament dynamics, such as Arp2/3 and Gelsolin⁷⁴. TRiC binds Gelsolin within its chamber, modulating its activity and regulate actin filament severing⁷⁴. In this way, TRiC functions as both a foldase, facilitating protein folding, and a holdase, stabilizing substrates and preventing aggregation.

1. 1. 9. Previous studies for substrate folding mediated by TRiC

The substrate folding mechanism of TRiC has been a longstanding question in the field. Substrate folding via TRiC is driven by its ATPase cycle. Substrates initially bind to the open state of TRiC and, upon closure, are released into the internal cavity where folding occurs^{30,75}. Many biochemical and biophysical studies have been conducted to understand how TRiC assists the folding of specific

substrates.

Tubulin Folding

Tubulin, one of the earliest identified TRiC substrates^{64,76}, is an obligate substrate of TRiC. Tubulin is approximately 50 kDa in size and is ubiquitous and abundant in eukaryotic cells. After tubulin undergoes initial folding by TRiC, it undergoes a maturation step with tubulin-binding cofactors (TBC), eventually forming microtubules^{77,78}. However, how nascent tubulin polypeptides achieve their three-dimensional structure after being translated by the ribosome is not fully understood. Nonetheless, crystal structures have shown how tubulin binds to the open conformation of TRiC, revealing low-resolution density masses at the specific location of apical and equatorial domains⁵⁵. These studies, however, did not resolve the secondary structure, leaving the tubulin presumably unfolded at this stage.

Actin Folding

Actin is one of the most extensively studied obligate substrates of TRiC⁷⁹⁻⁸¹. Actin, a 42 kDa protein, is one of the most abundant cytoskeletal proteins in cells and folds into its monomeric G-actin before assembling into F-actin filaments. Actin's bacterial homolog, MreB, shares a similar structure and size, forming filamentous structures in prokaryotes and receiving folding assistance from group I chaperonin GroEL^{82,83}. The structural stability of actin depends on cations and nucleotides; when these are released, actin unfolds⁸⁴. Actin unfolds in three stages: first, loss of cations leads to the first intermediate state (I_1), followed by loss of nucleotides to form a quasi-folded second intermediate state (I_2). The final stage is an aggregation-prone third intermediate state (I_3), which is recognized by TRiC⁸⁵⁻⁸⁹. TRiC is essential for the transition from I_3 to I_2 . Indeed, alanine scanning experiments confirmed that actin is recognized and folded by TRiC through interactions with specific polar and charged residue⁹⁰. Consequently, a multistep actin folding model by TRiC has been proposed^{81,91}.

A major breakthrough in understanding TRiC-mediated actin folding came from the Hartl group's research⁴⁹. Using HDX-MS

experiments, they mapped the time-resolved folding of actin domains, showing that certain subdomains fold as early as the bound state, with most of the actin structure after ring closure. The C-terminus helix of actin folds next, followed by the folding of the β -sheet region of the N-terminus subdomain SD1.

Other Substrates

Other substrates, such as mLST8, have been shown to partially fold and bind within the central cavity between TRiC rings⁹². Additionally, the encapsulated structure of sigma3 inside the closed TRiC chamber provides insights into how substrates interact with the charged internal surface of TRiC during folding⁴².

Despite numerous attempts to understand the TRiC-mediated folding cycle, the overall mechanism of folding for such diverse substrates remains elusive. Typically, the varying structural features of TRiC substrates suggest that it may provide different folding mechanisms depending on the nature of the substrate.

1. 1. 10. Co-chaperone PhLP families and substrate folding

Another critical aspect of TRiC function is its interaction with co-chaperones, which forms a network to assist in substrate folding. TRiC collaborates with various co-chaperones, notably the PhLP (Phosducin-like protein) family, which are about 30 kDa cytosolic proteins that directly or indirectly contribute to TRiC-mediated protein folding. The PhLP homologs share a central thioredoxin-like domain, with their structure consists of an N-terminal domain made up of several helices, as well as a C-terminal tail⁹³. The length of N-terminal domain varies significantly across subtypes⁹⁴.

Each PhLP exhibits unique characteristics and shows distinct specificity for TRiC substrates. PhLPs are exclusive to eukaryotes, with their subtypes varying across species. In humans, PhLPs are divided into three main subgroups: Subgroup I includes Pdc and PhLP1, Subgroup II includes PhLP2A and PhLP2B, and Subgroup III includes PhLP3⁹³. PhLP1 is universally expressed across most tissues and cell types and plays a role in folding of G β , forming a

complex with G β -G γ ⁹⁵⁻⁹⁷. Pdc does not directly bind to TRiC but is specifically expressed in photoreceptor cells and, like PhLP1, forms a complex with G β -G γ ⁹⁵. PhLP2A is broadly expressed⁹⁸, like PhLP1, whereas PhLP2B is tissue-specific⁹⁹. Both are implicated in actin folding^{99,100}. PhLP3 is less well understood but has been reported to assist in the folding of both tubulin and actin¹⁰¹. In yeast, only two types, plp1 and plp2, exist, suggesting an evolutionary diversification of PhLP subtypes across species¹⁰². PhLPs are known to influence TRiC activity and are involved in the folding of specific substrates, although the exact mechanisms remain unclear¹⁰¹.

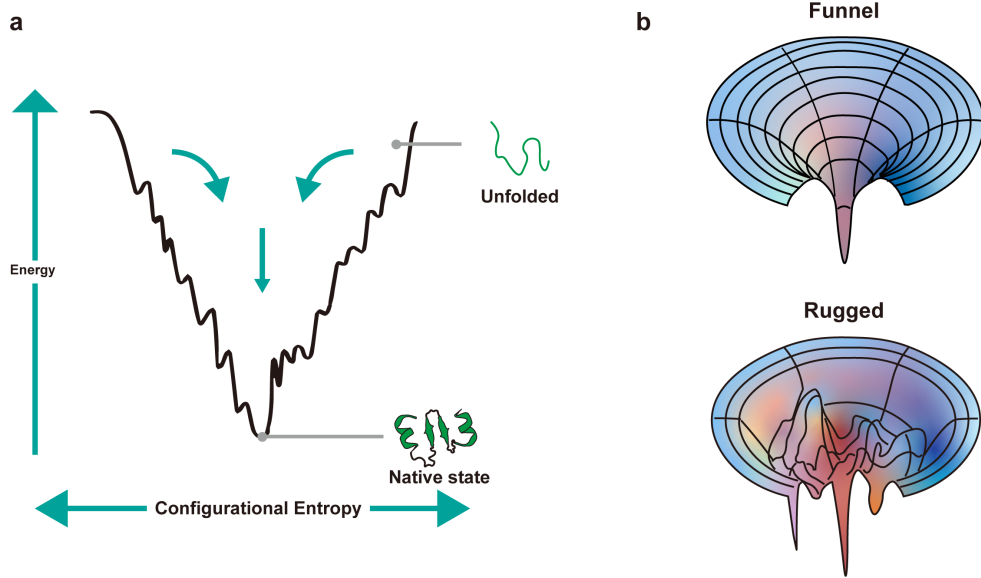


Figure 1.1 Free energy landscape of protein folding. **a** A schematic diagram of representative free energy landscape of protein folding. Vertical axis represents free energy while horizontal axis represents configurational entropy. **b** (top) A typical smooth funnel-shape energy landscape for a fast folder. (bottom) a rugged energy landscape by structural frustration of proteins.

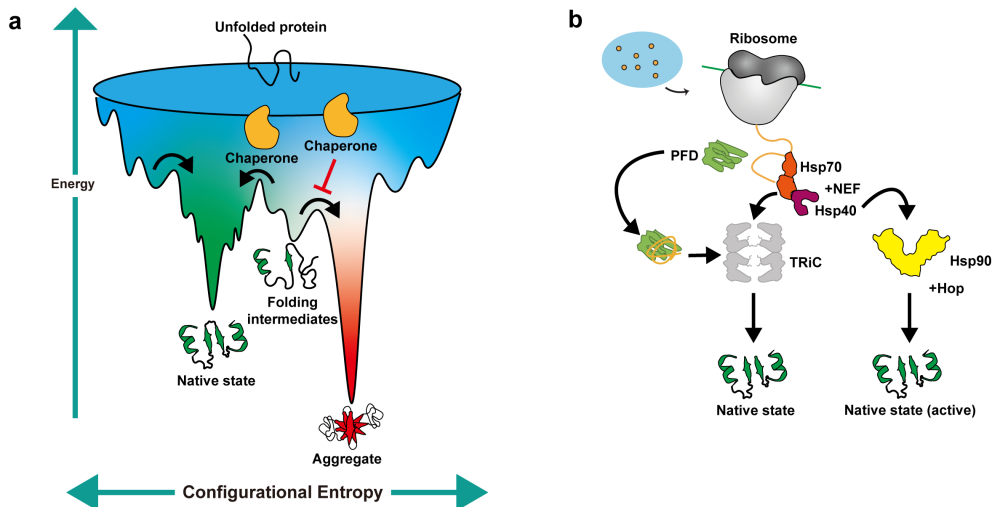


Figure 1.2 Protein folding assisted by chaperone network. **a** Energy landscape of protein folding process mediated by chaperone. In the unfolded state, proteins can adopt various conformations, gradually progressing toward a thermodynamically favorable state in confined structures. Due to various kinetic issues, the reaction proceeds to off-pathway or become kinetically trapped in non-native conformations. Molecular chaperone networks help prevent protein aggregation and assist proteins in overcoming free-energy barriers, ultimately guiding proteins toward its native state. **b** Chaperone network for protein folding in cytosol. Many nascent polypeptides synthesized by ribosomes require the assistance of chaperones for proper folding. Initially, chaperones like Hsp70 and Hsp40, or prefoldin (PFD), capture these nascent chains and stabilize them to prevent premature misfolding or aggregation. Then, PFD transfer these polypeptides to TRiC, which facilitates further folding. After this initial capture and stabilization, Hsp70 collaborates with the Hsp90 and its cochaperone Hop system to ensure activation and folding completion.

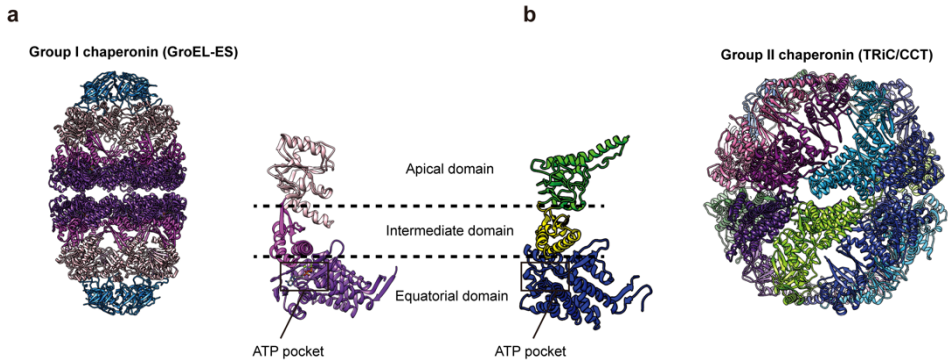


Figure 1.3. Structural architecture of Group I and Group II chaperonin **a** Crystal structure of Group I chaperonin GroEL-ES complex (PDB:4pko)¹⁰³. A subunit of GroEL is zoomed in and color coded according to the domain architecture (equatorial domain: medium purple, intermediate domain: magenta, apical domain: pink). **b** Cryo-EM structure of Group II chaperonin TRiC (PDB: 8I1U)¹⁰⁴. A subunit of TRiC is zoomed in and color coded according to the domain architecture (equatorial domain: blue, intermediate domain: yellow, apical domain: green). The black box indicates ATP binding pocket in the equatorial domain.

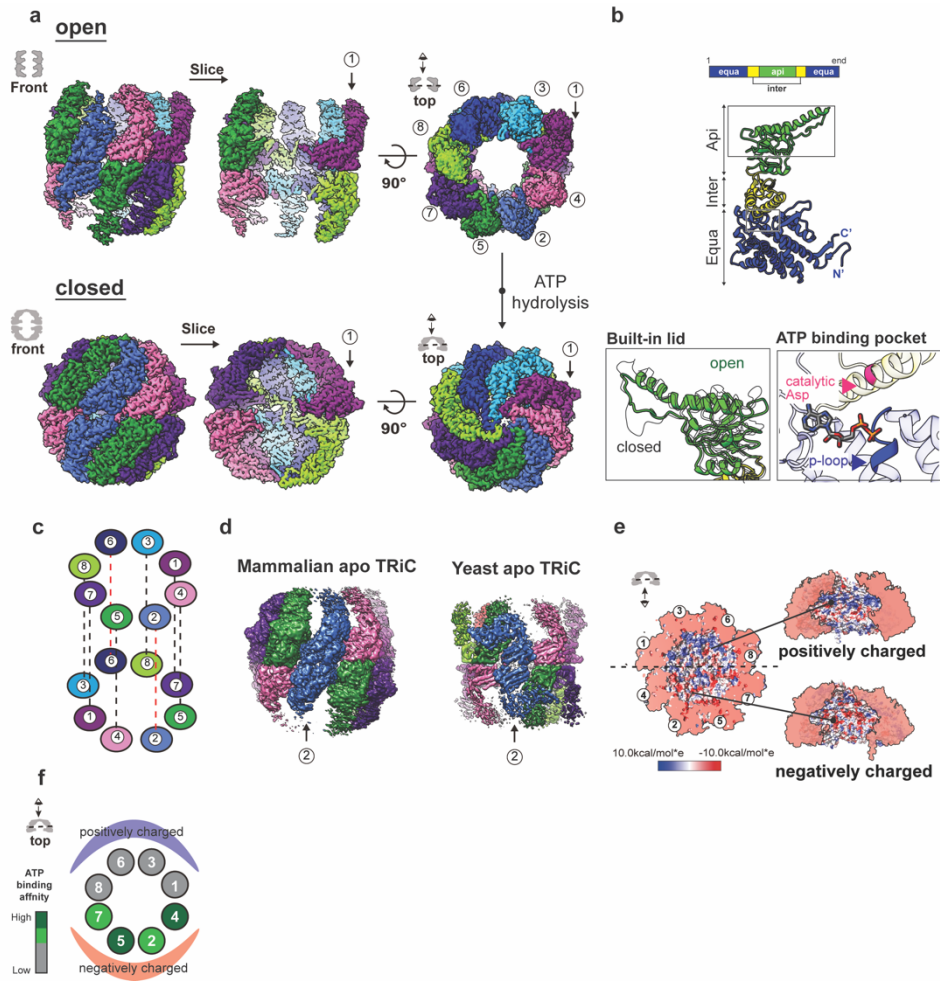


Figure 1.4. Structure of TRiC and ATP-driven structural change. **a** The cryo-EM structure of TRiC in either open or closed state, and chamber closing driven by ATP hydrolysis. Structure of open TRiC (EMD-33053), structure of closed TRiC (EMD-32926)¹⁰⁵. **b** CCT subunit with three domains with a zoom-in view of the built-in lid in the apical domain and ATP binding pocket in the equatorial domain. **c** A schematic of subunit arrangements of TRiC. The red dotted line indicates the subunit nests on each other. **d** Mammalian apo TRiC structure (EMDB:33053)¹⁰⁵ and yeast apo TRiC structure (EMDB: 9540)⁵⁸ in open conformation. **e** Asymmetric charge distribution on the inner chamber wall of the closed TRiC. Upon chamber closing, half of the hemisphere of CCT1/3/6/8/ is charged positively, while the other half hemisphere is charged negatively. **f** Color-coded diagram of different ATP affinities of individual CCT subunits. Deep

green: high ATP binding affinity, chartreuse: mild ATP binding affinity, gray: low binding affinity. Figures are modified from Gestaut et al. (2019a)³¹.

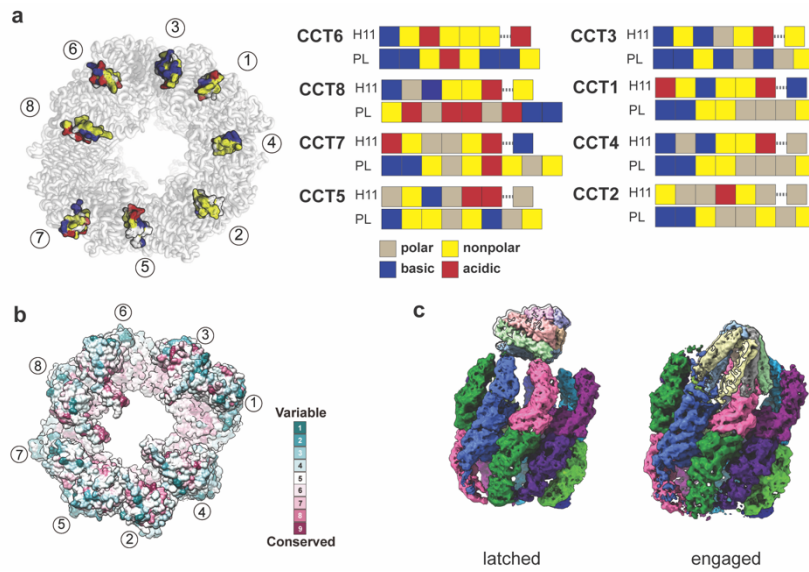


Figure 1.5. Substrate recognition and delivery to TRiC. **a** Charge distribution in the apical domain of each CCT subunit, labeled as a color code; gray: polar, yellow: nonpolar, blue: basic, red: acidic. Each box represents one helix. **b** Diagram of residue conservation score of each CCT subunit. The surface is colored from calculated scores using ConSurf¹⁰⁶. **c** Structures of PFD-TRiC complex visualized by cryo-EM. Left: latch-binding mode of PFD on TRiC (EMD-0493), middle: “engaged” binding mode of PFD on TRiC, whose tail is deep inside the open chamber (EMD-0491)⁵⁹. (A) Adopted from Gestaut et al. (2019a)³¹. (B) Adopted from Park et al. (2023)¹⁰⁴.

a

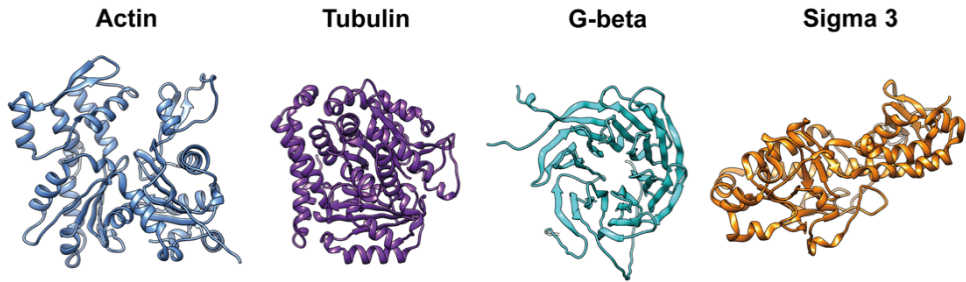


Figure 1.6. Identified obligate substrate of TRiC. a Atomic models of substrate proteins assisted by TRiC. (actin, tubulin, G-beta: from AlphaFold DB. sigma 3: 7lup)⁴²

1.2. Purpose of Research

1. 2. 1. Limitation of previous research and unanswered questions

The substrate folding cycle of TRiC is composed of substrate delivery, co-chaperone cooperation, substrate folding, and substrate release (Figure 1.7). To understand the mechanisms behind each stage, numerous biochemical and biophysical studies have been conducted, with actin being the most common model substrate for TRiC^{49,81,107}.

During the substrate delivery, studies on actin folding mediated by TRiC have shown that when actin is delivered by prefoldin (PFD), the folding rate is significantly accelerated⁵⁹. After delivery, the unfolded substrate binds to the apical domain of TRiC^{49,50}, and substrate expansion occurs¹⁰⁸.

In the substrate folding step, it has been reported that actin folding follows a two-step process⁸¹. Using methods like mutant-based studies and HDX-MS (Hydrogen-Deuterium Exchange Mass Spectrometry), the folding kinetics, as well as the interactions between the substrate and TRiC, have been mapped out^{49,91}.

For substrate release, the C-terminus has been identified as playing a crucial role⁸¹. Additionally, the co-chaperone PhLP family has been shown to directly participate in TRiC's ATPase activity and assist in substrate folding¹⁰¹.

Despite the insights gained from previous studies above, current studies lack detailed residue-level information for each stage of TRiC-mediated folding. This is primarily because substrate folding is highly heterogeneous and involves fast reactions, making it difficult to capture intermediate steps of the folding cycle experimentally. As a result, our understanding of TRiC-mediated folding remains fragmented. In this thesis, I focus on three major questions to address the gaps in understanding:

1. What is the mechanism of substrate delivery to TRiC via PFD?

TRiC receives most of its substrates through prefoldin (PFD). The interaction between PFD and TRiC has been structurally visualized, showing that they can adopt various conformations during this process⁵⁹. However, those structural studies do not answer the mechanism by which PFD transfers substrates to TRiC, how the delivered substrates bind to TRiC and the intermediate states of substrates in TRiC (Figure 1.7i). Further research is needed to clarify these processes.

2. How does co-chaperone cooperation occur during the TRiC ATP cycle?

TRiC collaborates with various co-chaperones, particularly with the Phosducin-like protein (PhLP) family. While it is known that PhLPs influence the folding process by interacting with TRiC, the specific mechanisms of how PhLPs bind to TRiC and contribute to the folding process remain unclear (Figure 1.7ii). Further research is needed to understand PhLP's precise role in TRiC-mediated substrate folding and its coordination during the ATP cycle.

3. What is the mechanism of TRiC-mediated substrate folding?

TRiC folds substrates with diverse topologies. Each substrate may interact with TRiC in unique ways, but the detailed mechanisms of how substrates engage with TRiC within its chamber, and their specific folding pathways they follow, remain largely unknown (Figure 1.7iii). While some insights into substrate-TRiC interactions have been obtained, the structural details of these interactions and the intermediate steps of the folding process within the TRiC chamber are still limited and remain elusive. More research is needed to uncover the intricacies of these processes.

Altogether, this thesis focuses on investigating the folding cycle of TRiC. Specifically, it aims to explore the heterogeneity of TRiC-cochaperone-assisted folding through three-dimensional structural studies at each stage of the cycle. By examining the folding pathways, this research seeks to fill the gaps in understanding the mechanisms by which TRiC facilitates the folding process.

This study aims to enhance our understanding of the substrate folding process mediated by eukaryotic chaperonins. Particularly, this research addresses long-standing questions in the field regarding the function of chaperonins: how substrates are delivered to chaperonins, coordinated with co-chaperones and assisted during folding. Structural investigation of these processes will define the roles of chaperonins and co-chaperones, filling in gaps in chaperone-mediated folding pathway.

By structurally visualizing protein folding, this study lays the groundwork for a deeper understanding of protein folding mechanisms. In addition, this research will provide insight into the mechanisms of protein misfolding, which is linked to various diseases. Ultimately, this research will help establish a foundation for understanding folding-related diseases and may contribute to the development of therapeutic strategies aimed at treating conditions arising from protein misfolding.

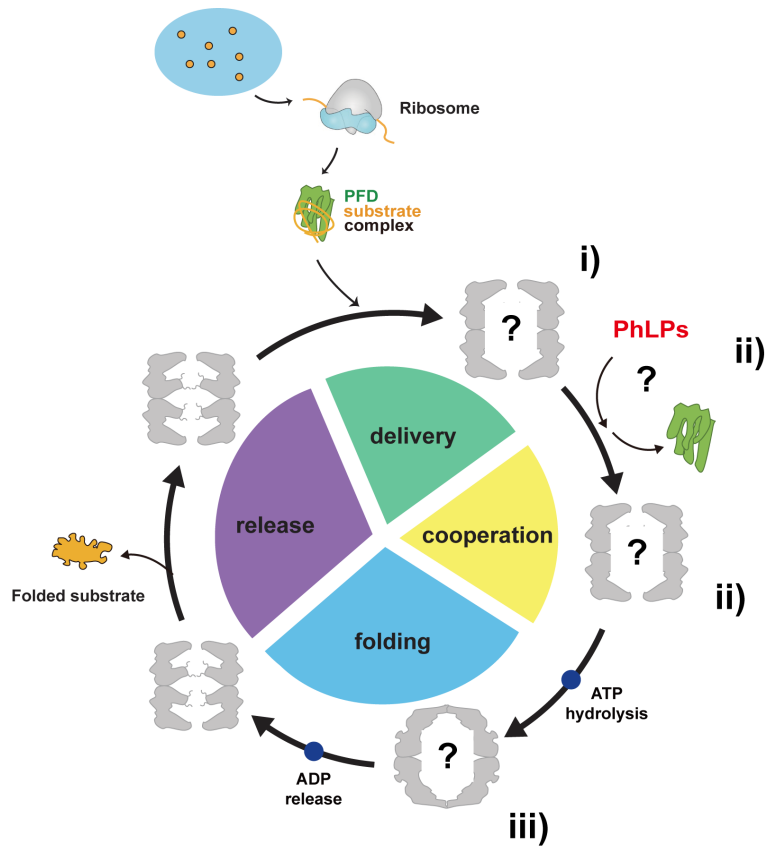


Figure 1.7 TRiC mediated substrate folding cycle remains elusive.

After translation of nascent polypeptides from ribosome, PFD captures the substrate preventing aggregation of the substrate. i) Delivery: PFD delivers substrate to TRiC. ii) Cooperation: PFD, PhLP families, and TRiC cooperates for substrate folding. iii) Folding: After ATP hydrolysis, substrate folding occurs in the closed TRiC chamber. Release: After ADP release, TRiC re-opens and substrate is released from TRiC. However, the mechanisms of i), ii), and iii) remain unknown.

Chapter 2. Methods

2.1. Cryo-EM of TRiC, co-chaperone, substrate complex

2. 1. 1. Cryo-EM of grid preparation and data collection

Purification of protein samples

All protein samples (TRiC, Prefoldin:substrate, PhLP1, PhLP2A, PhLP2B) were shipped from Frydman Lab at Stanford University.

TRiC

Briefly, TRiC with CCT1 tagged with GFP were overexpressed using High Five insect cells. Cells were harvested and resuspended in TRiC lysis buffer (100 mM HEPES pH 7.4, 50 mM NaCl, 20 mM imidazole, 10% glycerol, 5 mM PMSF) supplemented with benzonase (Sigma-Aldrich-Aldrich, E1014) (1,000 units) and a protease inhibitor cocktail [Roche]. Cells were lysed using Dounce homogenization and cleared supernatant was passed over nickel resin and washed with column wash buffer (50 mM HEPES pH 7.4, 50 mM NaCl, 5 mM MgCl₂ 20 mM imidazole, 10% glycerol) with an additional 250 mM NaCl, column wash buffer + 1 mM ATP, column wash buffer + an additional 500 mM NaCl, and finally column wash buffer alone. Nickel-bound protein was eluted with an elution buffer (50 mM HEPES pH 7.4, 50 mM NaCl, 5 mM MgCl₂ 400 mM imidazole, 10% glycerol). Protein-containing fractions were pooled and passed over a heparin column equilibrated with MQA buffer (50 mM HEPES pH 7.4, 50 mM NaCl, 5 mM MgCl₂, 0.5 mM EDTA, 1 mM DTT, 10% glycerol). Protein was eluted with a linear gradient of 20% to 100% MQB buffer (50 mM HEPES pH 7.4, 1 M NaCl, 5 mM MgCl₂, 0.5 mM EDTA, 1 mM DTT, 10% glycerol). TRiC-containing fractions were pooled and diluted with MQ buffer (50 mM HEPES pH 7.4, 5 mM MgCl₂, 1 mM DTT, 10% glycerol) to remove excess NaCl. Pooled

TRiC was loaded onto a MonoQ ion exchange column and eluted with a 200 ml linear gradient of 0% to 100% MQB. TRiC-containing fractions were pooled, concentrated with a 100 kDa MWCO Centricon device, and passed over a Superose-6 size exclusion column equilibrated with MQA. TRiC-containing fractions were pooled, concentrated, and snap-frozen in liquid nitrogen for long-term storage.

Human Prefoldin:substrate

All subunits of *HsPFD* and substrates (β -tubulin, β -actin) were co-expressed using baculovirus in High Five insect cells (twice as much virus was used for β -actin compared to *HsPFD* subunits). Cells were resuspended in lysis buffer (100 mM HEPES pH 7.4, 100 mM NaCl, 15 mM imidazole, 5 mM PMSF) supplemented with benzonase (Sigma-Aldrich-Aldrich, E1014) (1,000 units) and a protease inhibitor cocktail [Roche]) and lysed using Dounce homogenization. Lysate was cleared by ultracentrifugation at 40,000 * g for 30 min. Cleared lysate was passed over nickel resin, washed with column buffer (100 mM NaCl, 50 mM HEPES pH 7.4) and eluted with column buffer + 400 mM imidazole. Fractions containing protein were passed over a MonoQ 10/100 anion exchange column equilibrated with buffer A (50 mM HEPES pH 7.4, 50 mM NaCl) washed with buffer A until UV baselined, and then eluted with a 160 ml gradient to 60% buffer B (50 mM HEPES pH 7.4, 1 M NaCl). Fractions containing PFD: β -substrate were identified by SDS-PAGE, concentrated to ~1 ml, and ran over an SDX200 column. Fractions containing PFD:substrate were again identified by SDS-PAGE, concentrated, 50% glycerol added to 10%, aliquoted, snap-frozen and stored at -80 °C

Human PhLP2A

Plasmids were transformed into BL21 Rosetta2 pLysS and induced to express O/N at 17 °C. Cells were resuspended in lysis buffer 50 mM HEPES pH 7.4, 600 mM NaCl, 20 mM imidazole, 5 mM PMSF) supplemented with benzonase (Sigma-Aldrich-Aldrich, E1014) (1000 units) and a protease inhibitor cocktail [Roche]) and lysed using an emulsiflex. The lysate was cleared by centrifugation at 20,000*g for

30 min. Cleared lysate was purified by passing over nickel resin and washing with lysis buffer followed by column buffer (lysis buffer lacking protease inhibitors). Protein was eluted using column buffer + 400 mM imidazole. Fractions containing protein were concentrated using Amicon ultra 3 kD MWCO concentrators and ran over an SDX200 equilibrated with 50 mM HEPES pH 7.4, 100 mM NaCl, 1 mM DTT. Fractions containing PhLP2a protein were identified by SDS-PAGE and protein was concentrated using an Amicon Ultra 3 kD MWCO. 50% glycerol was added to a final concentration of 5% to protein, and the protein was aliquoted, snap frozen, and stored at -80°C .

Cryo-EM grid preparation

Apo-TRiC

3 μL of apo-TRiC sample was vitrified at 2 mg/mL and applied to 200-mesh R1.2/1.3 holey-carbon grids (Quantifoil) coated with Poly-L-lysine and vitrified using Vitrobot Mark IV (Thermo Fisher Scientific, CMCI in Seoul). 6,084 Movies were collected on a Titan Krios (Thermo Fisher Scientific) equipped with a Falcon 4 (Thermo Fisher Scientific) detector.

Prefoldin: β -tubulin:TRiC

0.5 μM TRiC sample was mixed with 2 μM Prefoldin: β -tubulin complex at RT. CryoEM grids (Quantifoil R1.2/1.3 200 Cu) were glow discharged (PELCO easiGlow) for 45 s 0.07% Octyl-beta-glucoside was mixed with the sample prior to vitrification. Sample was vitrified using Vitrobot Mark IV, where 2.7 μL sample was applied on the cryoEM grids and blotted for 3 s 11,796 movies were collected on a Titan Krios (Thermo Fisher Scientific) equipped with the K2 Summit (Gatan) detector.

TRiC: β -tubulin with ATP- AlF_x

1 μM copurified TRiC: β -tubulin sample was incubated with ATP- AlF_x for 1 h at 37°C . CryoEM grids (Quantifoil R1.2/1.3 200 Cu) were glow discharged (PELCO easiGlow) for 45 s. Sample was vitrified using a Gatan Leica GP plunger, where 2.7 μL sample was applied on the

cryoEM grids and blotted from the back for 3–5 s 31,204 movies were collected on Titan Krios (Thermo Fisher Scientific) equipped with the K2 Summit (Gatan) detector.

PhLP2A–TRiC

2 mg/ml of purified TRiC was incubated at RT with purified PhLP2A in 1:4 molar ratio for 2 h. Then, 3 μ L of PhLP2A–TRiC sample was applied to 200-mesh R1.2/1.3 holey-carbon grids (Quantifoil) coated with Poly-L-lysine and blotted for 3.5 s and vitrified using Vitrobot Mark IV (Thermo Fisher Scientific, CMCi in Seoul). 15,075 movies were collected on a Titan Krios (Thermo Fisher Scientific) equipped with a K3 BioQuantum detector with 20 eV energy filter slit (Gatan) in CDS mode.

PhLP2A–TRiC with ATP/AlFx

0.8 mg/ml of purified TRiC was mixed with PhLP2A in 1:4 molar ratio for 30 min. Then, 1 mM ATP, 1 mM $\text{Al}_3(\text{NO}_3)_3$, 6 mM NaF, 10 mM MgCl_2 50 mM KCl were added and incubated for 1 h at RT. 3 μ L of PhLP2A–TRiC ATP/AlFx sample was applied to glow discharged cryoEM grids (Quantifoil R1.2/1.3 200 Cu). Samples were vitrified using Vitrobot Mark IV. 1,368 movies were collected on a Glacios (Thermo Fisher Scientific) equipped with the Falcon 4 (Thermo Fisher Scientific) detector.

PFD–PhLP2A–TRiC

2 mg/ml of purified TRiC was sequentially incubated with purified PFD and PhLP2A in 1:2: ~ 1 for each 20 min at RT with 1 mM AMP–PNP. Then, an aliquot of 3 μ L of this sample was applied to 200-mesh R1.2/1.3 holey-carbon grids (Quantifoil) blotted for 3.5 s and vitrified using Vitrobot Mark IV (Thermo Fisher Scientific, CMCi in Seoul). 1,270 movies were collected on a Glacios (Thermo Fisher Scientific) equipped with the Falcon 4 (Thermo Fisher Scientific) detector.

Truncated PhLP2A–TRiC

2 mg/ml of purified TRiC was incubated with each purified truncated PhLP2A mutant (TXD, NTD–TXD, TXD–CTD) in 1:2 molar ratio for 20 min at RT. Then, an aliquot of 3 μ L of this sample was applied to 200-mesh R1.2/1.3 holey-carbon grids (Quantifoil) blotted for 3.5 s

and vitrified using Vitrobot Mark IV (Thermo Fisher Scientific, CMCI in Seoul). 2,199 movies for NTD-TXD, 352 movies for TXD and 339 movies for TXD-CTD were collected on a Glacios (Thermo Fisher Scientific) equipped with the Falcon 4 (Thermo Fisher Scientific) detector.

Truncated PhLP2A-TRiC with ATP/AlF_x

To prepare the sample of TRiC in the presence of 1 mM ATP/AlF_x, 0.8 mg/ml of purified TRiC was incubated with each purified truncated PhLP2A mutant (TXD, NTD-TXD, TXD-CTD) in 1:2 molar ratio for 20 min, then 1 mM ATP, 1 mM Al₃(NO₃)₃, 6 mM NaF, 10 mM MgCl₂ and 50 mM KCl were added and incubated for 1 h at RT. Then, 3 μL of truncated PhLP2A-TRiC sample was applied to 200-mesh R1.2/1.3 holey-carbon grids (Quantifoil) blotted for 3.5 sec and vitrified using Vitrobot Mark IV (Thermo Fisher Scientific, CMCI in Seoul). 2,014 movies for NTD-TXD, 516 movies for TXD, and 644 movies for TXD-CTD were collected on a Glacios (Thermo Fisher Scientific) equipped with the Falcon 4 (Thermo Fisher Scientific) detector.

PhLP2A-β-actin-TRiC with ATP/AlF_x

0.8 mg/ml of purified TRiC was mixed with co-purified PFD- β-actin and PhLP2A in a 1:2:2 molar ratio. They were incubated for 20 min and 1 mM ATP, 1 mM Al₃(NO₃)₃, 6 mM NaF, 10 mM MgCl₂ and 50 mM KCl were added followed by incubation for 30 min at 37 °C. 3 μL droplets of samples were then applied to Vitrobot Mark IV (Thermo Fisher Scientific, CMCI in Seoul) and blotted for 3.5 s. After plunge freezing, 3635 micrographs were collected on Glacios (Thermo Fisher Scientific) equipped with the Falcon 4 (Thermo Fisher Scientific) detector.

2. 1. 2. Cryo-EM data processing

All image processing was done in RELION 3.1¹⁰⁹ and cryoSPARC v3.2.¹¹⁰ Computing resources were utilized in the S²C² SLAC national facility and at CMCI at Seoul National University.

Apo-TRiC

Movies were aligned in 5 x 5 patches in MotionCor2¹¹¹ and CTF parameters were estimated with GCTF¹¹². Utilizing template-based autopicking in cryoSPARC v3.2, 2,100,259 particles were initially picked. After 2D classification and removing bad particles, 945,248 particles were subjected to 3D heterogeneous refinement using Ab initio model in cryoSPARC. After further 3D classification and CTF refinements, non-uniform refinement was performed using 662,744 particles yielding a 3.11 Å map of apo-TRiC based on the gold-standard Fourier shell correlation (FSC) at 0.143.

Prefoldin:β-tubulin:TRiC

Movies were aligned in 5 x 5 patches in MotionCor2,¹¹¹ and CTF parameters were estimated with GCTF¹¹². After initial template-based picking of 1,621,636 particles, 2D classification was performed. After selection, 443,858 particles were used for 3D classification yielding 2 major classes, Prefoldin bound TRiC with 194,013 particles and non-bound TRiC with 249,845 particles. Using non-uniform refinement, prefoldin bound and non-bound TRiC was reconstructed at a resolution of 3.9 Å and 4.2 Å, respectively.

TRiC:β-tubulin with ATP-AIFx

21,486 movies were aligned in 5 x 5 patches by MotionCor2¹¹¹, and CTF parameters were estimated with CTFFIND (v 4.1)¹¹³. Particles picked with a template matching method were subject to multiple rounds of 2D classification followed by 3D classification. 819,553 particles in open state were used to reconstruct an open state TRiC:β-tubulin map to 3.8 Å, and 529,181 particles were used to obtain a 2.7 Å C1 symmetry map.

All following image processing was done in RELION 4.0¹⁰⁹ and cryoSPARC v3.3¹¹⁰. Computing resources were utilized at CMCI at Seoul National University.

PhLP2A-TRiC

Movies were aligned in patches and CTF parameters were estimated in patches using cryoSPARC. Utilizing template-based autopicking in cryoSPARC v3.3, particles were initially picked and after 2D classification, they were used to train Topaz¹¹⁴ and successfully picked 2,691,733 good particles. Among them, 2,285,466 particles

were subjected to 3D heterogeneous refinement after ab initio model in cryoSPARC. Further 3D classification and CTF refinements were performed and non-uniform refinement was performed at last using 1,796,900 particles yielding a 3.05 Å consensus map of PhLP2A-TRiC based on the gold-standard Fourier shell correlation (FSC) at 0.143. For compositional analysis, heterogeneous refinement yielded one PhLP2A bound TRiC (486,149) and two PhLP2A bound TRiC (1,311,220). To further refine PhLP2A density, the consensus map was splitted into two half rings and merged to double the particle population. Then, the apical domain of TRiC and PhLP2A was masked and 3D classification was performed without alignment in RELION 4.0. CCT3 bound and CCT4 bound PhLP2A fraction were independently selected and locally refined in cryoSPARC again. As a result, CCT3 bound PhLP2A map and CCT4 bound PhLP2A map were obtained with 3.82 and 4.22 Å resolution, respectively.

Closed PhLP2A-TRiC with ATP/AlFx

Movies were aligned in patches and CTF parameters were estimated with patch CTF correction in cryoSPARC. After the initial template-based picking of 833,250 particles, 282,298 particles were selected by 2D classification. After selection, ab initio and a few rounds of heterogeneous refinement resulted in 220,847 particles of closed TRiC (83.8%) and 42,742 particles of open TRiC (16.2%). Then, the inner chamber of closed TRiC density was masked followed by 3D classification without alignment in RELION. 30,911 particles (14.0%) contained one PhLP2A density and 21,028 particles (9.5%) showed two PhLP2A densities in the chamber. Since two PhLP2A densities exhibited the best density feature of PhLP2A, only TRiC containing two PhLP2A particles was pooled and imported to cryoSPARC. At last, after local motion correction and non-uniform refinement, 3.24 Å of closed PhLP2A-TRiC complex map was obtained. For the illustration purpose, we sharpened PhLP2A density independently from TRiC subunit densities as they showed varying resolution. PhLP2A maps were then segmented and shown in different thresholds for illustration.

PFD-PhLP2A-TRiC

Movies were aligned and CTF parameters were estimated in patches using cryoSPARC. 402,311 particles were picked using template matching and 2D classification was performed. Then, 232,059 particles were picked and ab initio reconstruction and multiple heterogeneous refinement was performed. 109,228 particles were used to reconstruct the consensus map of 3.84 Å. Since the noisy density around the PFD binding site and PhLP2A binding site was observed, further classification was performed. First, heterogeneous refinement giving PFD-TRiC maps in cryoSPARC as references successfully pooled 50,832 particles of TRiC with PFD density. The resolution was further pushed by discarding bad PFD-containing particles yielding 4.19 Å resolution of the PFD-TRiC map. Further masked 3D classification was performed but no PhLP2A density was detected. Meanwhile, a 3D reconstructed map without PFD was exported to RELION and 3D classification without alignment was performed near the PhLP2A binding site. 25,226 particles showed PhLP2A density while 25,129 particles were reconstructed as an apo-like structure.

Truncated PhLP2A-TRiC

(i) NTD-TXD of PhLP2A: Movies were aligned and CTF parameters were estimated in patches using cryoSPARC. 700,078 particles were picked using template matching and 2D classification was performed. Then, 588,578 particles were picked and ab initio reconstruction and multiple heterogeneous refinement was performed. 120,405 particles were used to reconstruct the consensus map of 4.11 Å. Since the noisy density around the NTD-TXD of the PhLP2A binding site was observed, further classification was performed. The apical domain of TRiC and PhLP2A was masked and 3D variability was performed in cryoSPARC. 23,847 particles (19.8%) contained NTD-TXD of PhLP2A density in the chamber. (ii) TXD of PhLP2A: Movies were aligned and CTF parameters were estimated in patches using cryoSPARC. 128,028 particles were picked using template matching and 2D classification was performed. Then, 33,767 particles were picked and ab initio reconstruction and multiple heterogeneous refinement was performed. 15,519 particles were used to reconstruct

the consensus map of 7.24 Å. (iii) TXD-CTD of PhLP2A: Movies were aligned and CTF parameters were estimated in patches using cryoSPARC. 125,947 particles were picked using template matching and 2D classification was performed. Then, 27,116 particles were picked and ab initio reconstruction and multiple heterogeneous refinement was performed. 20,959 particles were used to reconstruct the consensus map of 3.78 Å.

Truncated PhLP2A-TRiC with ATP/AlFx

(i) NTD-TXD of PhLP2A: Movies were aligned and CTF parameters were estimated in patches using cryoSPARC. 899,293 particles were picked using template matching and 2D classification was performed. Then, 216,756 particles were picked and ab initio reconstruction and multiple heterogeneous refinement was performed. 157,313 particles were used to reconstruct the consensus map of 4.38 Å. Since the noisy density inside the TRiC chamber was observed, further classification was performed. The inner chamber of closed TRiC density was masked and 3D variability was performed in cryoSPARC. 12,976 particles (8.25%) contained NTD-TXD of PhLP2A density in the chamber. (ii) TXD of PhLP2A: Movies were aligned and CTF parameters were estimated in patches using cryoSPARC. 232,578 particles were picked using template matching and 2D classification was performed. Then, 57,473 particles were picked and ab initio reconstruction and multiple heterogeneous refinement was performed. 24,924 particles were used to reconstruct the consensus map of 6.61 Å. (iii) TXD-CTD of PhLP2A: Movies were aligned and CTF parameters were estimated in patches using cryoSPARC. 291,069 particles were picked using template matching and 2D classification was performed. Then, 106,204 particles were picked and ab initio reconstruction and multiple heterogeneous refinement was performed. 39,112 particles were used to reconstruct the consensus map of 4.60 Å.

PhLP2A- β -actin-TRiC with ATP/AlFx

Movies were aligned and CTF parameters were estimated in patches using cryoSPARC. 2,197,105 particles were picked using template-based picking followed by few rounds of 2D classification. 162,754

particles were subjected to 3D classification and open TRiC (14,924 particles) and closed TRiC 3D density maps (109,373 particles) were reconstructed. Closed TRiC was then further refined using CTF refinement and non-uniform refinement yielding consensus map of 3.38 Å resolution. Particles were targeted to 3D variability analysis using the inner chamber mask and classified 57.5% empty TRiC (62,899 particles) and 42.5% occupied TRiC (46,474 particles). Particles showing empty chambers were discarded and the rest of the particles were classified using 3D variability again to improve resolution followed by non-uniform refinement yielding 4.42 Å resolution of the structure (8,378 particles).

2. 1. 3. Atomic model building and Refinement

Prefoldin: β -tubulin:TRiC

Model building started from previous Prefoldin:TRiC model (PDB: 6NR8).⁵⁹ The initial model was fitted into the density map and manually refined in COOT.⁵ Then, the model was refined on the Namdinator server using MDFF¹¹⁵ and Phenix real space refinement default options¹¹⁶. After few rounds, the model was further corrected using Phenix and COOT.

Copurified TRiC: β -tubulin under ATP-AlFx condition

The model of TRiC in the closed form (PDB: 7LUM)⁴² reference was rigidly fit into the closed state TRiC density by rigid body fitting with Fit in Map tool from Chimera v1.14. This fitted model was further refined with phenix.real_space_refine in Phenix v1.18.1, ISOLDE v1.1.0. And refined models were inspected and adjusted in COOT. The model of tubulin (PDB: 6I2I)¹¹⁷ was rigidly fitted to each tubulin intermediate density, and manually adjusted by COOT and ISOLDE v1.1.0¹¹⁸. All adjusted models were then refined using phenix.real_space_refine in Phenix.

All models were validated by Q-score¹¹⁹ and phenix.validation_cryoem.¹¹⁶ Difference maps showing the nucleotide density in TRiC-tubulin closed state were calculated between the complex density map and the map calculated from the model of

protein only, generated by phenix.real_diff_map. The figures of the difference map were generated by Chimera with the same contour level 3 sigma. All other figures were generated by Chimera and ChimeraX^{120,121}.

PhLP2A-TRiC

The previous model of TRiC (PDB ID: 6NRA) was used as a reference to rigid-body fitting in the map. The structure of a thioredoxin-fold domain of human phosducin-like 2 (PDB code: 3EVI) and TXD-CTD of the AlphaFold-predicted model were used for the initial reference for the rigid-body fitting. After being fitted onto the density map, the initial model was manually refined in COOT and further refined in Phenix real space refinement with default parameters.

PFD-PhLP2A-TRiC

The previously reported PFD-TRiC model (PDB:7W7U)⁶⁷ was used for the map model fitting and the illustration.

PhLP2A-CCT3

H3 of PhLP2A (residues 63-89) and CCT3 predicted using AlphaFold was used as an initial model and fitted onto the map. TXD of PhLP2A and CCT3 from PhLP2A:TRiC consensus model in the open state was used for fitting TXD of PhLP2A. After manual refinement of TXD of PhLP2A and CCT3 in COOT, the model was refined using MDFF and Phenix real space refinement with default options for few rounds.

PhLP2A-CCT4

AlphaFold-predicted model of H3 of PhLP2A and CCT4 was used as an initial model and rigidly fitted onto the density map. TXD of PhLP2A and CCT4 from the consensus model was used to fit the TXD of PhLP2A. The model was refined in COOT manually, and further adjusted using MDFF and Phenix real space refinement with default options.

PhLP2A-TRiC with ATP/AlFx

The model of TRiC in the closed form (PDB ID: 7LUM) and TXD of PhLP2A from AlphaFold prediction was rigidly fitted into the density map. H2 and H3 of AlphaFold-predicted PhLP2A were used to fit the additional density extending from TXD of PhLP2A. The model was

then manually adjusted in COOT and further refined using MDFF and Phenix real space refinement with default parameters.

PhLP2A- β -actin-TRiC with ATP/AlFx

Previous model of the complex of PhLP2A- β -actin-TRiC in the closed form (PDB ID: 7NVM) and built model of PhLP2A-TRiC in the closed form from this study were fitted onto the map and used as initial models. The model of γ -actin in the initial model was exchanged with the model of β -actin from AlphaFold prediction. After rigid-body fitting, the models were manually adjusted in COOT. Further refinement was performed using MDFF and Phenix real space refinement with default parameters.

All models are validated by Phenix Comprehensive Validation (cryoEM) and Q-score.

2.2. Interaction mapping and AlphaFold prediction

PISA analysis

The interactions between TRiC and β -tubulin model in each state were calculated using the PISA server (<https://www.ebi.ac.uk/pdbe/pisa/>).

AlphaFold prediction

ColabFold¹²² prediction of version released on 2022/7/13 is used to predict the full-length model of PhLP2A. Default multisequence alignment pipeline and parameters are used without alteration. A predicted model deposited in AlphaFold DB (<https://Alphafold.ebi.ac.uk/entry/Q9H2J4>) was additionally presented. Complexes of CCT3-PhLP2A and CCT4-PhLP2A are predicted using the same version of ColabFold with default parameters and MSA pipeline without any relaxation nor templates. Chain break between each component is specified with a colon to predict the heterodimeric complex.

2.3. Sequence alignment and evolutionary analysis

Logo plot generation

For TRiC and β -tubulin, residue conservation was compared across 393 mainly eukaryotic with some archaeal species (group II chaperonins) for residues predicted to make interactions by PISA. Plots were generated using *EDlogo* plot¹²³. For PhLP2A and TRiC, residue conservation was compared across 150 mainly eukaryotic with some archeal species for residues participating in the interaction with PhLP2A or PFD. Logo plots were generated using WebLogo 3¹²⁴.

Sequence alignment and phylogenetic tree building

Multiple sequence alignments for tubulin and tubulin homologues were generated using the multiple sequence alignment tool T-coffee Espresso and visualized¹²⁵. A phylogenetic tree of tubulin and tubulin homologs was made in MEGA X software¹²⁶.

Sequence alignment and phylogenetic tree building

HHMER¹²⁷ was used to find hits of phosducin and phosducin-like protein variants from the eukaryotic system. Human phosducin and phosducin-like protein variants were used as a template for search and hits with low e-values were manually pooled. Also, sequences of cd02957 from NCBI which corresponds to the phosducin-like family were manually pooled. Total 71 sequences were used to generate multiple sequence alignments using t-coffee¹²⁵. The phylogenetic tree was generated by FastTree¹²⁸ and visualized by Dendroscope¹²⁹. The protein residue conservation score was calculated based on Shannon entropy scores with default parameters¹³⁰. Then, based on the PhLP2A structure, aligned sequences were divided into 1-64 (H1-H2), 65-88 (H3), 89-199 (TXD), 200-239 (CTD) and the calculated scores of residues were averaged within each subgroup.

Generation of residue conservation colored surface model

For analyzing residue conservation of CCT, PhLP2A, PFD, Consurf¹⁰⁶ was used with default parameters. Briefly, sequences of CCT1-8, PhLP2A, PFD subunits were used as input independently in Consurf to find hits and multiple sequence alignment (MSA) for each subunit was made with default settings in Consurf. Then, each residue conservation score was calculated based on MSA in Consurf.

The surface models were colored and visualized in Chimera¹²⁰. For PhLP1, PhLP3, the model was generated using homology modeling¹³¹ and MSA for the conservation score calculation was generated using the grouped PhLP1 or PhLP3 sequences from the phylogenetic tree.

Chapter 3. Results

3.1. Structural study of substrate delivery to TRiC

3.1.1. Structural analysis of substrate-free apo open TRiC

Several studies have successfully resolved crystal and cryo-EM structures of open TRiC across species from yeast to mammals^{27,51,55,61,69,132,133}. Most apo TRiC structures have been determined at resolutions below 4 Å due to structural heterogeneity, limiting detailed residue-level analysis. Additionally, these structures often contain bound endogenous substrates, leaving the structure of substrate-free apo open TRiC unresolved^{55,133}.

To overcome this, I sought to resolve a high-resolution apo open TRiC structure using GFP-tagged purified TRiC. Cryo-EM grids were prepared with substrate-free apo TRiC at concentrations ranging from 0.25 mg/ml to 2 mg/ml, with 1 mg/ml proving to be the optimal condition. Data collection on a Falcon 4-equipped Titan Krios yielded around 6,000 movies, and after 2D and 3D classification using CryoSPARC, a 3.1 Å resolution structure of apo TRiC was obtained (Figure 3.1). The equatorial domain achieved approximately 3 Å resolution, while the more flexible apical domain was resolved to about 7 Å, consistent with the flexible nature of TRiC's apical domain (Figure 3.1d). Additionally, the GFP tag attached to CCT1 was observed at low threshold as designed.

The apo TRiC structure revealed the known asymmetric arrangement of 1-3-6-8-7-5-2-4, with the two rings stacked back-to-back²⁷. The cryo-EM map also displayed distinct asymmetric structural characteristics of CCT subunits in terms of the arrangement (Figure 3.2a). There are two large cavities at the interface between the equatorial domains: CCT1, CCT3 and CCT1, CCT4. CCT1 displayed distinct outward-facing features and closely

attached to CCT3. CCT7, CCT5, CCT2, and CCT4 are also tightly associated with each other, including their apical domains (Figure 3.2b). To further explore subunit dynamics, 3D variability analysis was performed. 3D variability analysis is a method that allows the visualization of continuous motions in proteins¹³⁴. This technique computes significant eigenvectors of the covariance of particle images, which linearize the multi-dimensional data and calculates trajectories of 3D structures (principal components analysis, PCA). The analysis revealed overall breathing motion of subunits forming compact or expanded conformation of TRiC (Figure 3.2c). In addition, significant motion of CCT1, which oscillated between inward and outward positions (Figure 3.2d). CCT7, CCT5, and CCT2 displayed coordinated motion especially in apical domains. When subunits were in compact conformation, the helical lids in the apical domain were resolved (Figure 3.2e) while in extended conformation, the density of the lids were not observed. This suggests a linked movement of apical domains of three subunits and that apical domains get stabilized or flexible according to the conformations of the subunits. Further studies will be required to reveal the detailed cooperativity among CCT subunits.

Next, I analyzed the occupancy of the ATP pockets of subunits in the equatorial domain. The new high-resolution map showed the clear nucleotide density in the low-affinity hemisphere (CCT3, CCT6, CCT8), whereas partial nucleotide occupancy was observed in the high-affinity hemisphere (CCT2, CCT5, CCT7) (Figure 3.2f). Since no nucleotides were added during grid preparation, the ADP in CCT3, CCT6 and CCT8 likely reflects endogenous nucleotides retained even during the ATP cycling while purification. ADP preference of these subunits corresponds with previous findings that CCT8 maintains ADP even in the closed state⁶¹.

3. 1. 2. Structural analysis of PFD-b actin-TRiC complex

Next, to visualize the handoff of the substrate from prefoldin (PFD) to TRiC, we incubated substrate-free apo TRiC with β -tubulin

copurified with PFD. After incubation, we collected cryo-EM data using the Titan Krios microscope. This yielded a 3.9 Å resolution cryo-EM map of PFD-bound TRiC from approximately 194K particles and a 4.2 Å map from 75K particles without PFD (Figure 3.3). The prefoldin:β-tubulin complex revealed that prefoldin is fully aligned with TRiC, and coiled coil helices of PFD extend into the inner chamber of TRiC (Figure 3.4b). PFD assumes a fully engaged conformation, one of six conformations when binding to TRiC⁵⁹. This allows PFD contacts to the apical domains of CCT3 and CCT4, consistent with previous studies (Figure 3.4b). Of note, in the TRiC density map without PFD, the apical domains of CCT3 and CCT4 show poorly resolved density, while in the PFD-bound map, these domains are well resolved (Figure 3.2a). This suggests that contact with PFD binding reduces the dynamic flexibility of the TRiC apical domains, stabilizing the overall binding mode.

Cryo-EM map of prefoldin:β-tubulin:TRiC complex and β-tubulin:TRiC complex without PFD both showed a significant extra density in the middle of the septum between equatorial regions of two rings while the density was not observed in the apo substrate free TRiC (Figure 3.3d, Figure 3.4b). Strikingly, the extended PFD6 coiled coil reached the extra density in the inter-ring space making a clear connection (Figure 3.4c). However, no significant extra density was observed inside PFD. The conformation of PFD is in the open extended form, which may reduce the binding affinity to facilitate the handoff of the substrate from PFD. Taken together, the cryo-EM map suggests the handoff of substrate from PFD to the inter-ring space of two rings.

The substrate-dependent extra density is oval-shaped and asymmetrically located in the septum between two rings, close to subunits CCT8, 6, and 3. The density made a clear connection to the N-terminal tails of CCT5 and 7, which are not observed in apo substrate-free open TRiC structure (Figure 3.4d). TRiC has a large central cavity (~6nm open cap, ~9 x 5nm inner space) in the inter-ring space. While the substrate-dependent extra density is observed in this space as a compact state, further focused 3D classification did

not capture any folded domain or secondary domain. This suggests the structural heterogeneity of β -tubulin delivered by PFD either arising from the unstable folding state or the positioning of the substrate.

Unlike previously reported findings⁴⁹, the density map did not reveal any notable extra density in the apical domain of TRiC. This could indicate that the interaction between the substrate and the apical domain is highly dynamic, making it difficult to capture. Alternatively, it is possible that the substrate, after interacting with the apical domain, has already been transferred into the inter-ring space due to interactions with PFD and the CCT tails. Thus, the prefoldin: β -tubulin map may represent the post-delivery substrate state.

Previously, TRiC was considered a chaperonin with two chambers. However, the prefoldin: β -tubulin map provides evidence for an additional chamber in the inter-ring space of open TRiC. Theoretically, this third chamber offers enough space for proteins up to ~50 kDa, but the observed substrate-dependent density likely consists of a mixture of the substrate, CCT tails, and PFD tails. Notably, both TRiC and PFD possess long, disordered N- and C-terminal tails that are not visualized in the map. The TRiC tails, with a combined protein mass of around 35.5 kDa (schematized in Figure 3.5a), are expected to move dynamically within this chamber (illustrated in Figure 3.5b). These tails both polar and hydrophobic characteristics (Figure 3.5a), suggesting they interact with the substrate and maintain β -tubulin in a conformationally dynamic coacervate state. This may help prevent the substrate from becoming trapped in an intermediate state, ensuring it remains primed for folding (Figure 3.5c).

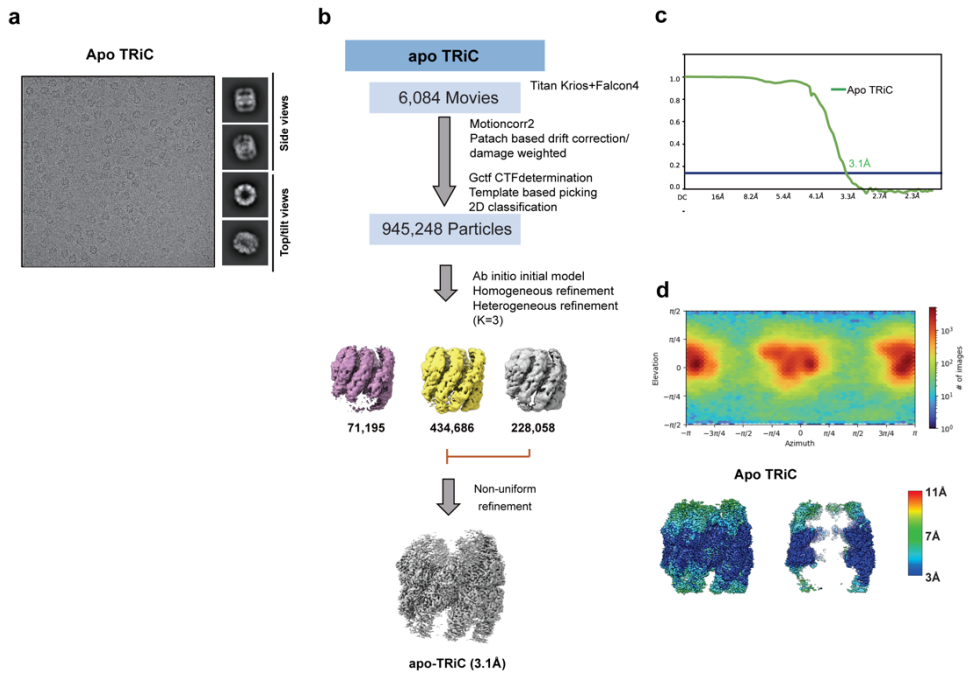


Figure 3.1 Cryo-EM workflow for apo-TRiC **a** Representative cryo-EM micrograph and 2D averages of apo-TRiC in the open conformation. **b** Image processing workflow of apo-TRiC and Gold standard FSC curve **c**, **d** Local resolution estimation of three reconstructed maps: apo-TRiC.

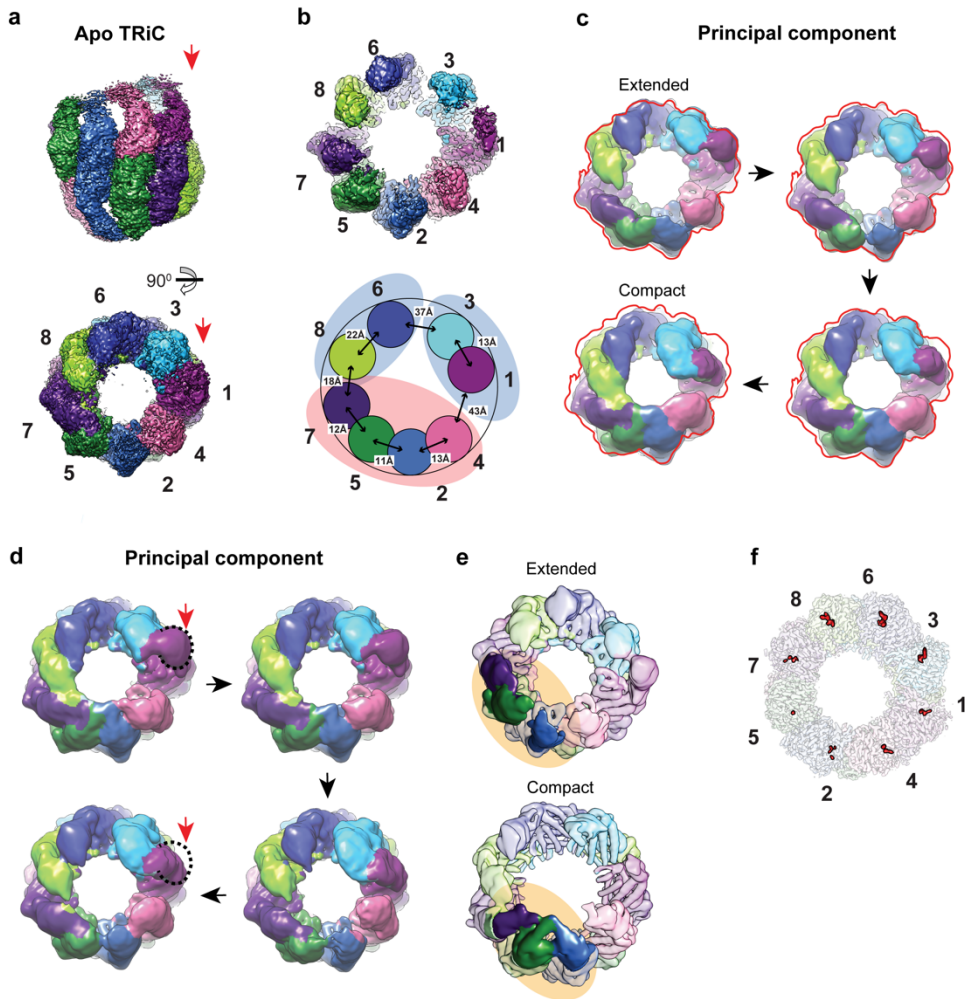


Figure 3.2 Cryo-EM structure of apo TRiC in open conformation **a** Side and top view of cryo-EM structure of apo TRiC in open conformation. The red arrow indicates CCT1 subunit. **b** Distance measurement between neighboring apical domains of CCT subunits. The blue colored circle indicates the positively charged hemisphere while red circle indicates the negatively charged hemisphere. **c** 3D variability analysis of apo TRiC. One of the principal components is visualized as density maps ranging from extended conformation to compact conformation of TRiC. **d** 3D variability analysis of apo TRiC. One of the principal components which represents the motion of CCT1 subunit is visualized as density maps **e** The comparison between extended conformation and compact conformation of apo TRiC. The orange color highlights the movement and conformational

changes of apical domains and helical lid. **f** Density of ATP binding pocket occupied with nucleotide of TRiC complex. Density corresponds to the nucleotide on each ATP binding pocket is segmented and colored red.

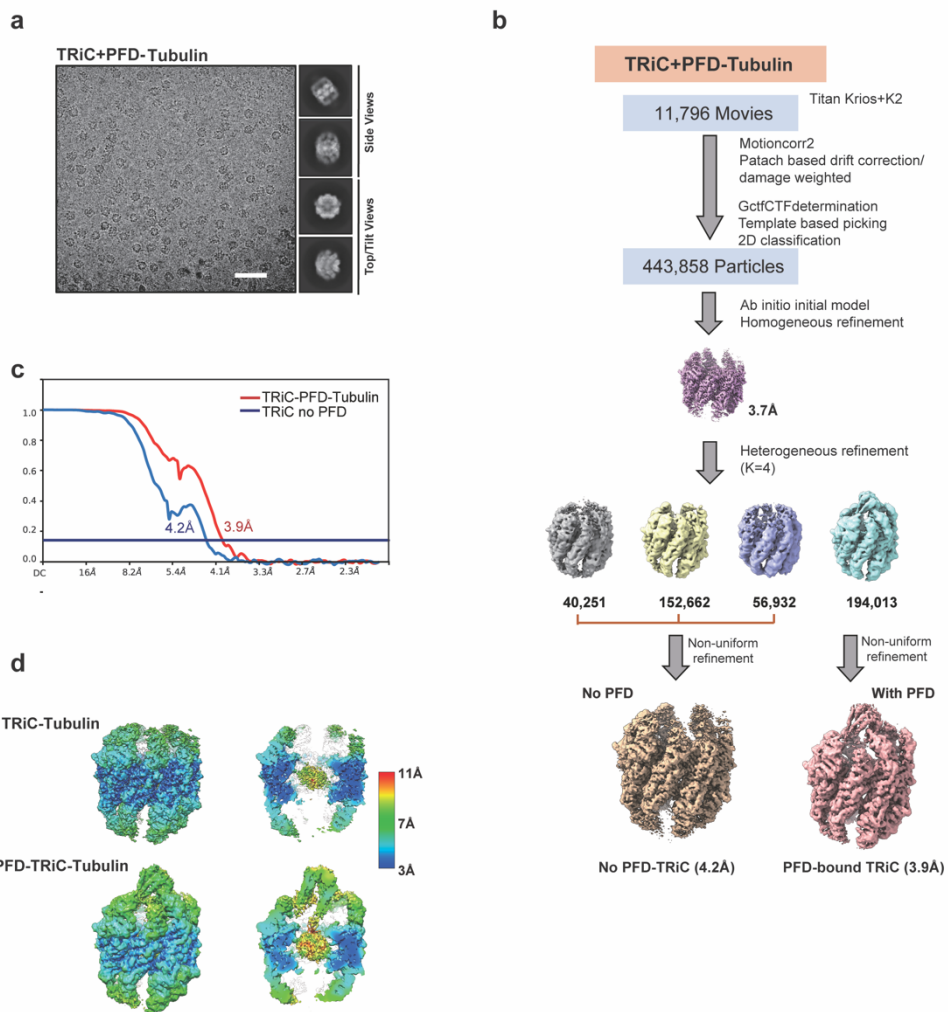


Figure 3.3. Cryo-EM workflow for prefoldin: β -tubulin-TRiC a Representative cryo-EM micrograph and 2D averages of the complex of Prefoldin: β -tubulin-TRiC in the open conformation. **b** Image processing workflow of Prefoldin: β -tubulin-TRiC and Gold standard FSC curve **c**, **d** Local resolution estimation of three reconstructed maps: TRiC: β -tubulin (Prefoldin unbound), Prefoldin:TRiC: β -tubulin.

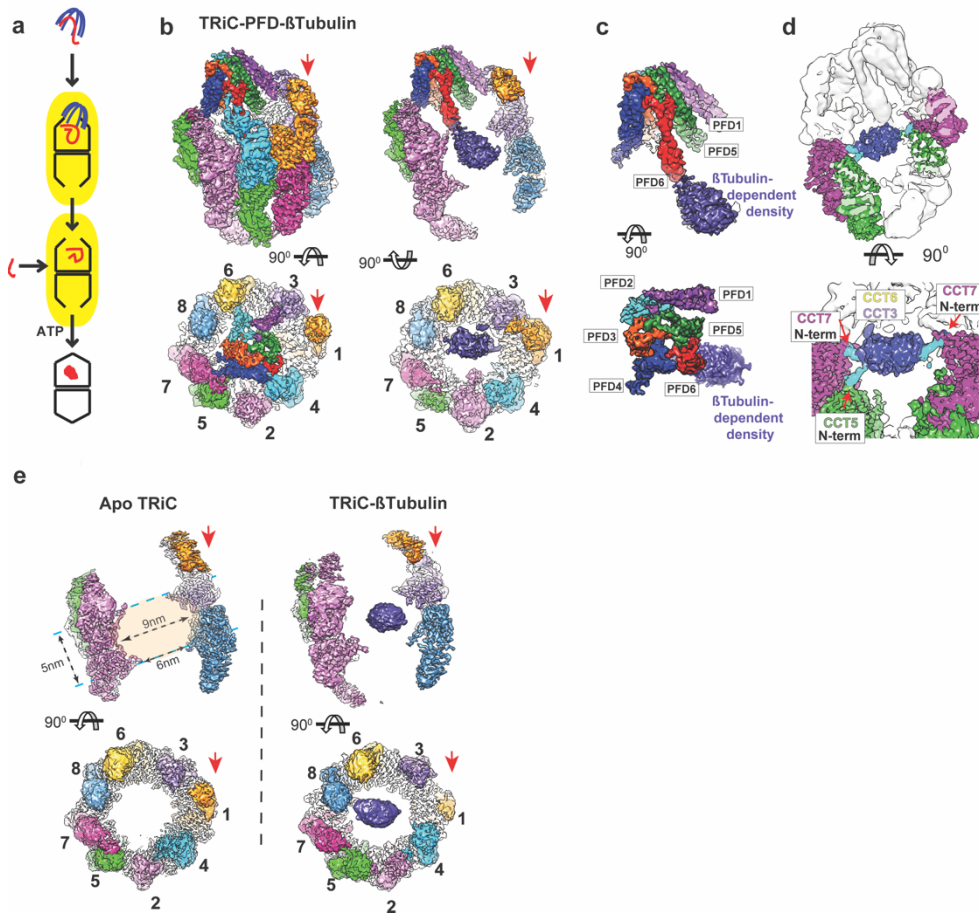


Figure 3.4. Ternary prefoldin: β -tubulin:TRiC complex in the open conformation **a** Model of substrate loading to TRiC. **b** Side and end-on view of the 3D reconstructed ternary complex and slice views showing β -tubulin density bound to TRiC. Red arrows indicate CCT1. **c** Side and end-on views segmented prefoldin: β -tubulin density. **d** Side and top view at lower threshold to illustrate N-terminal tail contacts from CCT5 and CCT7. **e** Side and top views from 3D reconstruction of apo-TRiC and TRiC: β -tubulin highlighting the β -tubulin density is absent from apo-TRiC. Red arrows indicate CCT1.

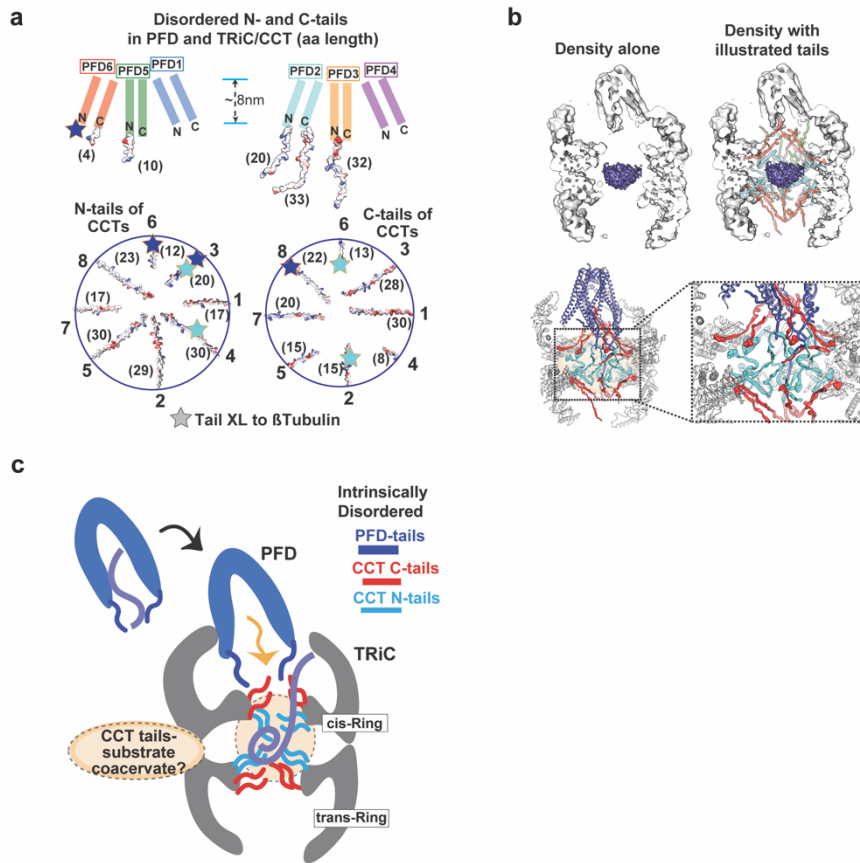


Figure 3.5. Tails and the central cavity of prefoldin: β -tubulin:TRiC complex in the open conformation **a** Schematic of disordered tail residues from the N and C termini of prefoldin (top) and TRiC (bottom) highlighting their electrostatic surface. Brackets denote the length (as number of residues) of each subunit's disordered tail. Star indicates residues within the disordered tails that XL to β -tubulin domains. **b** Schematic of disordered tails in the TRiC inter-chamber space with map (top) and model (bottom). Spheres in the model indicates the location of the first-resolved N-terminal (cyan) and the last-resolved C-terminal residues (red). **c** Cartoon of substrate delivery by the interplay of TRiC and prefoldin's disordered tails. The dotted circle in the TRiC chamber represents a hypothetical coacervate formed by substrate polypeptide and disordered CCT tails.

3.2. Structural study of cochaperone PhLP family and TRiC

3. 2. 1. Structural analysis of PhLP2A and open TRiC

I aimed to generate a complex between purified open human TRiC and PhLP2A by mixing and incubating *in vitro*, followed by cryo-EM to obtain structural information. I processed approximately 15,000 micrographs using cryoSPARC and obtained a consensus map with a 3.08 Å resolution, revealing PhLP2A-dependent density within the TRiC chamber (Figure 3.6). This density was located near the equatorial region of TRiC. The overall structure of TRiC resembled the previously observed open TRiC conformation, showing robust equatorial and dynamic apical regions (Figure 3.7a). Additionally, I observed partial nucleotide occupancy across TRiC subunits. More prominent nucleotide density was noted in the low-affinity hemisphere (CCT6, CCT8, CCT3), whereas partial nucleotide occupancy was observed in the high-affinity hemisphere (CCT2, CCT5, CCT7) (Figure 3.8). This is consistent with substrate-free apo open TRiC structure.

Further 3D classification and refinement revealed high-resolution features of the PhLP2A-dependent density (Figure 3.7b). We fitted the crystal structure of the thioredoxin-fold domain from human PhLP2B (PDB code: 3EVI)¹³⁵ to the electron density, and most secondary structures and bulky side chains matched well with the cryo-EM density map. This provided strong evidence that the extra density represents PhLP2A.

PhLP2A consists of an N-terminal domain (amino acids 1–90, NTD), a thioredoxin domain (amino acids 91–210, TXD), and a short C-terminal domain (amino acids 211–239, CTD) (Figure 3.7e). Based on the TXD and CTD densities, I was able to trace the backbone and model side chains, but no density corresponding to the NTD was observed. Therefore, I conducted focused 3D classification for each CCT subunit (Figure 3.6b). This analysis revealed the mid-resolution density of helix 3 (H3) of the NTD which adopted two different

orientations near the apical domains of CCT3 or CCT4 (Figure 3.7c, Figure 3.7d).

Next, I performed AlphaFold predictions for each PhLP2A-CCT subunit pair to predict the residues involved in the interaction. Notably, only the apical domains of CCT3 and CCT4 were predicted to interact with PhLP2A's H3, with good prediction scores (Figure 3.10), which was consistent with the cryo-EM density maps. Therefore, I built an atomic model of the complex between open TRiC and residues 63-232 of PhLP2A based on the cryo-EM density and predicted CCT3/4 and PhLP2A contacts (Figure 3.7c, Figure 3.7d).

The TRiC-PhLP2A atomic model showed domain-specific residue interactions between PhLP2A and open TRiC (Figure 3.9a Figure 3.9b, Figure 3.9c). PhLP2A binds in an extended conformation within the open TRiC chamber, with each domain interacting with specific TRiC subunits. The TXD domain of PhLP2A is encapsulated within the open TRiC chamber, constrained by hydrophilic and hydrophobic interactions from the equatorial domains of CCT3 and CCT1 (Figure 3.9a, Figure 3.9b). The CTD interacts primarily via hydrophobic interactions at the interface formed by the equatorial domains of CCT3 and CCT6, with the hydrophobic side of the CTD helix forming a hydrophobic zipper motif with an equatorial helix of CCT6 (Figure 3.9a, Figure 3.9c). PhLP2A's NTD can adopt two different orientations, with H3 contacting the apical domains of CCT3 or CCT4 (Figure 3.9a). Although the NTD is primarily negatively charged, H3 has a distinct positively charged patch that shows a high degree of complementarity with the negatively charged apical domains of CCT3 and CCT4 (Figure 3.9b).

3. 2. 2. Structural analysis of PhLP1 and open TRiC

PhLP1 is involved in the folding of G β protein⁹³ and is known to bind to the apical domain of TRiC^{136,137}, suggesting a distinct underlying mechanism compared to PhLP2A. To investigate PhLP1's unique mechanism, I conducted cryo-EM experiments to obtain structural

information on the PhLP1–open TRiC complex. PhLP1 and open TRiC were purified and mixed in a 1:2 ratio, followed by incubation at room temperature for grid preparation. Subsequent cryo-EM data collection yielded around 900 micrographs. After 2D and 3D classification, approximately 50K particles were used to obtain a mid-resolution structure of 4.84 Å (Figure 3.11a, Figure 3.11b). The TRiC structure displayed structural features of the apo open TRiC, with each subunit showing dynamic apical domain features. Notably, extra density was resolved in the apical domains of the CCT3 and CCT6 subunits (Figure 3.11c).

Then, I performed 3D variability analysis on the extra density region using a focused mask to resolve more high-resolution features. Although further 3D refinement did not resolve any noticeable secondary structures, the electron density mass was observed and fitting the thioredoxin-fold model of PhLP1 matched the overall size (Figure 3.11d). This finding is consistent with the previous findings that PhLP1 binds to the apical domains of TRiC subunits. Meanwhile, the helical lids of the CCT3 and CCT6 apical domains were resolved, which was absent in apo open TRiC (Figure 3.2a). This suggests that PhLP1 binding reduces the dynamics of these domains by forming contacts with them. Larger dataset of cryo-EM would be required more precise PhLP1's interaction with open TRiC in the future.

3. 2. 3. Structural analysis of PhLP2B and open TRiC

In mammals, PhLP2B shares approximately 57% sequence similarity with PhLP2A but is expressed specifically in germ cells^{98,99}. PhLP2B is expected to have a similar function to PhLP2A, involving in actin folding mechanism. To gain insight on the modulation by PhLP2B, I used AlphaFold to predict PhLP2B structure. The result exhibited a similar structural topology to PhLP2A (Figure 3.32c) composed of NTD, TXD, and CTD. Sequence alignment of PhLP2A and PhLP2B indicated that the residues involved in interaction with TRiC are highly conserved between the two (Figure 3.32b). These imply

conserved binding mechanism to open TRiC.

To get structural information of the PhLP2B-TRiC complex, purified PhLP2B and substrate-free apo TRiC were mixed, incubated, and plunge-frozen. Around 700 micrographs were collected, and after several rounds of 2D and 3D classification, a PhLP2B-TRiC complex structure was obtained at 4.46 Å resolution (Figure 3.12a). The open TRiC showed similar features to previous open TRiC structures, with extra density observed in the equatorial domains of CCT1, CCT3, and CCT6. The thioredoxin-fold was resolved at the equatorial domains of CCT1 and CCT3, and the C-terminal helix was docked at the interface between the equatorial domains of CCT3 and CCT6 (Figure 3.12b Figure 3.12c). Overall, PhLP2B resembled the binding conformation of PhLP2A. Like the PhLP2A consensus map, the NTD of PhLP2B was not visible, likely due to the dynamic nature of the NTD and the apical domains of CCT3 and CCT6.

Taken together, PhLP2B shares a similar cooperation mechanism to TRiC with PhLP2A, while its function may be regulated based on its tissue-specific expression in germ cells.

3. 2. 4. Structural analysis of PhLP2A and closed TRiC

TRiC undergoes lid closure upon ATP hydrolysis, forming an isolated central chamber. To investigate whether PhLP2A forms a complex with closed TRiC, we conducted another cryo-EM experiments. In a previous study, Jin et al. demonstrated that TRiC exhibits the same closed structure under both ATP and ATP/AlFx conditions, showing full nucleotide occupancy in the ATP binding pocket⁶¹. Since AlFx mimics a stable post-hydrolysis state during TRiC's ATP hydrolysis cycle⁶⁰, it shifts and locks the population of closed TRiC states, allowing us to obtain more particles for high-resolution structures. We incubated TRiC and PhLP2A in a 1:4 molar ratio with ATP/AlFx and performed cryo-EM analysis (Figure 3.13). The consensus map of the closed TRiC reached a 2.95 Å resolution, and significant extra density was observed inside the chamber. This closed TRiC structure resembled the native ATP-induced structure, with full nucleotide

occupancy in the CCT subunits (Figure 3.14).

Subsequent focused 3D classification of the inner TRiC chamber revealed states with PhLP2A in one chamber (14.0%) and in both chambers (9.5%) (Figure 3.13b). The map of the state with PhLP2A in both chambers exhibited higher-resolution features, so I selected these particles to obtain the final electron density map of closed TRiC with encapsulated PhLP2A within the chamber at a 3.24 Å resolution (Figure 3.15a). The cryo-EM map clearly showed details of the backbone and side chains of TRiC and PhLP2A and an atomic model was refined based on the map. For PhLP2A, I was able to build a model spanning residues 27–214 (Figure 3.15b). The density of NTD H1–2 (aa1–26) and CTD (aa 215–239) were not clearly observed but showed low-resolution density of the NTD near CCT1 and CCT3, and the CTD near the intermediate domains between CCT1 and CCT4 (Figure 3.15b).

Interestingly, PhLP2A forms domain-specific contacts with certain CCT subunits in the closed TRiC chamber, which differ from those observed in the open state. NTD was anchored to the chamber wall of closed CCT3 and CCT6 making multiple salt bridges between negatively charged residues of the NTD and positively charged residues in CCT3 and CCT6 (Figure 3.15c). The TXD is positioned near the lid regions of CCT5, CCT2, and CCT4 through polar and hydrophobic interactions (Figure 3.15c). Previous analyses confirmed that the TRiC inner chamber has an asymmetric charge distribution, with a positively charged surface contributed by CCT1/3/6/8 and a negatively charged surface by CCT7/5/2/4 (Figure 3.15d). PhLP2A establishes a diagonal binding topology within the asymmetric TRiC chamber, driven by the electrostatic interaction between its negatively charged NTD and the positively charged hemisphere of TRiC, along with the interaction between its TXD and the TRiC lid segments on the opposite hemisphere (Figure 3.15d, Figure 3.15e). Unlike PFD, PhLP2A binds to both the open and closed states of TRiC. During ATP hydrolysis and subsequent ring closure, TRiC forms a sealed chamber wall and lid, prompting the relocation of PhLP2A domains within the chamber. As TRiC transitions from the

open to the closed state, PhLP2A's NTD H3 disengages from the apical domains of CCT3 and CCT4, moving approximately 50Å to bind to the charged wall of CCT3 and CCT6 (Figure 3.16a, Figure 3.16b). Additionally, the TXD rotates by about 180 degrees and shifts 30Å, moving from interactions with CCT3 and CCT1 in the open state to new contacts with the CCT5/2/4 lid segments (Figure 3.16a, Figure 3.16b). Finally, the hydrophobic interaction between PhLP2A's CTD and the CCT3/6 interface dissipates, bringing the CTD in proximity to the inner wall of CCT1/4. In conclusion, the interaction between PhLP2A and the newly formed chamber wall and lid in closed TRiC leads to a reorientation of PhLP2A's domain interactions, inducing a dramatic structural rearrangement.

3. 2. 5. Structural analysis of PhLP2A, PFD and TRiC complex

PhLP2A and the co-chaperone PFD both associate with TRiC as a platform to carry out their functions. To investigate the relationship between PhLP2A and PFD upon TRiC binding, I first analyzed their interaction patterns with TRiC. Previous reports have shown that PFD binds to the charged apical domains of CCT3 and CCT4 in the open state of TRiC but dissociates in the closed state⁵⁹. When comparing the interaction surfaces of CCT3/4 in the atomic models of PhLP2A and PFD (PDB:7WU7)⁵⁹, I found that both interactors exhibit similar interaction networks with the CCT subunits, particularly forming specific salt bridges (Figure 3.17a). When the two models were superimposed, the contact sites of PFD and PhLP2A with TRiC subunits significantly overlapped (Figure 3.17a). Based on this structural analysis, I hypothesized that steric hindrance between PFD and PhLP2A could lead to mutually exclusive binding, establishing a competitive relationship between them for TRiC interaction.

PFD primarily binds through electrostatic interactions centered around the apical domains of CCT3/4, while PhLP2A has multiple binding sites on both the apical domains of CCT3/4 and the equatorial domains of CCT3/6. This difference in binding modes likely

contributes to PhLP2A's preferential and more stable association with TRiC, even when PFD is present. Thus, I performed cryo-EM experiments with both PFD and PhLP2A incubated with TRiC.

The cryo-EM analysis revealed that the particles displayed high heterogeneity in the co-chaperones' binding states (Figure 3.18). Further 3D classification showed that TRiC particles either contained only PFD, only PhLP2A, or had no binding at all, with no population observed where both PFD and PhLP2A were simultaneously bound (Figure 3.17b). This observation supports the idea that PFD and PhLP2A bind to TRiC in a mutually exclusive manner.

Next, I analyzed whether the interaction regions of PFD and PhLP2A with TRiC were evolutionarily conserved. The results showed that the electrostatic patch on CCT4 is highly conserved, and earlier studies showed that mutations in this region impair cellular proteostasis⁵⁹. Residue conservation analysis further revealed that the residues forming the contact surfaces among TRiC, PFD, and PhLP2A are evolutionarily conserved. Specifically, PFD6 has a highly conserved positive charge that contacts CCT4 (Figure 3.18f), and the charged patch on PhLP2A's H3, which interacts with CCT4, is also evolutionarily conserved (Figure 3.18f, Figure 3.18g). This evolutionary conservation suggests that these three chaperones have coevolved to coordinate substrate delivery and TRiC-mediated folding.

3. 2. 6. Structural analysis of truncated PhLP2A upon ATP cycle of TRiC

To further dissect the interactions between PhLP2A domains and specific TRiC subunits, we generated four truncated domain mutants: NTD (amino acids 1–84), TXD (amino acids 85–211), NTD-TXD (amino acids 1–211), and TXD-CTD (amino acids 85–239) (Figure 3.19a). To analyze the binding modes of each truncated mutant, I mixed these mutants with both open and closed TRiC and observed them using cryo-EM (Figure 3.20). In the cryo-EM maps of open TRiC, attributable densities for each PhLP2A mutant were observed

in positions similar to full-length PhLP2A. The NTD-TXD fragment showed clear NTD density near the apical domains of CCT3/CCT4 in the open TRiC chamber, but the TXD density appeared more heterogeneous (Figure 3.19a). The TXD fragment alone was only visible at a low contour level near the equatorial domain of TRiC. This suggests that PhLP2A's intrinsic affinity for the TRiC chamber depends more on other PhLP2A domains than TXD. In agreement, the TXD-CTD mutant showed high-resolution features resembling full-length PhLP2A, with the CTD anchored between CCT3 and CCT6, and the TXD located near CCT3 (Figure 3.19a). The structural features of the TXD-CTD complex were sharper, suggesting that CTD plays an important role in PhLP2A binding to open TRiC (Figure 3.19a).

I then added ATP/AlFx to induce rearrangement of all PhLP2A mutants within the closed TRiC chamber (Fig). In the closed TRiC chamber, NTD-TXD reoriented similarly to full-length PhLP2A, but no density was observed for TXD or TXD-CTD (Figure 3.19a). This suggests that although TXD and TXD-CTD are encapsulated in the closed chamber, they interact weakly and dynamically, with NTD providing the major anchoring interface (Figure 3.19a).

PhLP2A domains have distinct roles in interacting with TRiC. In the open state, TXD and CTD are essential for stable binding to TRiC, while NTD is crucial for proper orientation of PhLP2A within the closed chamber. The truncation experiments provide insight into the binding and release events during PhLP2A rearrangement as the chamber closes. Each TRiC ring is composed of eight subunits with distinct ATP binding affinities¹³⁸, leading to an asymmetric wave of chamber closure. Each CCT subunit undergoes structural changes during ATP hydrolysis, which are transmitted through an allosteric network connecting the equatorial and apical domains (Figure 3.19b). We hypothesize that this conformational change releases NTD from the apical domains of CCT3/CCT4 and anchors it to the closed, charged chamber wall at CCT3/6 (Figure 3.19b). This process reorients and relocates PhLP2A within the closed chamber. Ring closure also weakens the strong interactions between CTD and TXD

with their CCT subunits in the open state, allowing them to undergo relocation within the chamber. The anchoring effect of NTD in the closed state may enhance the interactions of TXD and CTD with the chamber interior.

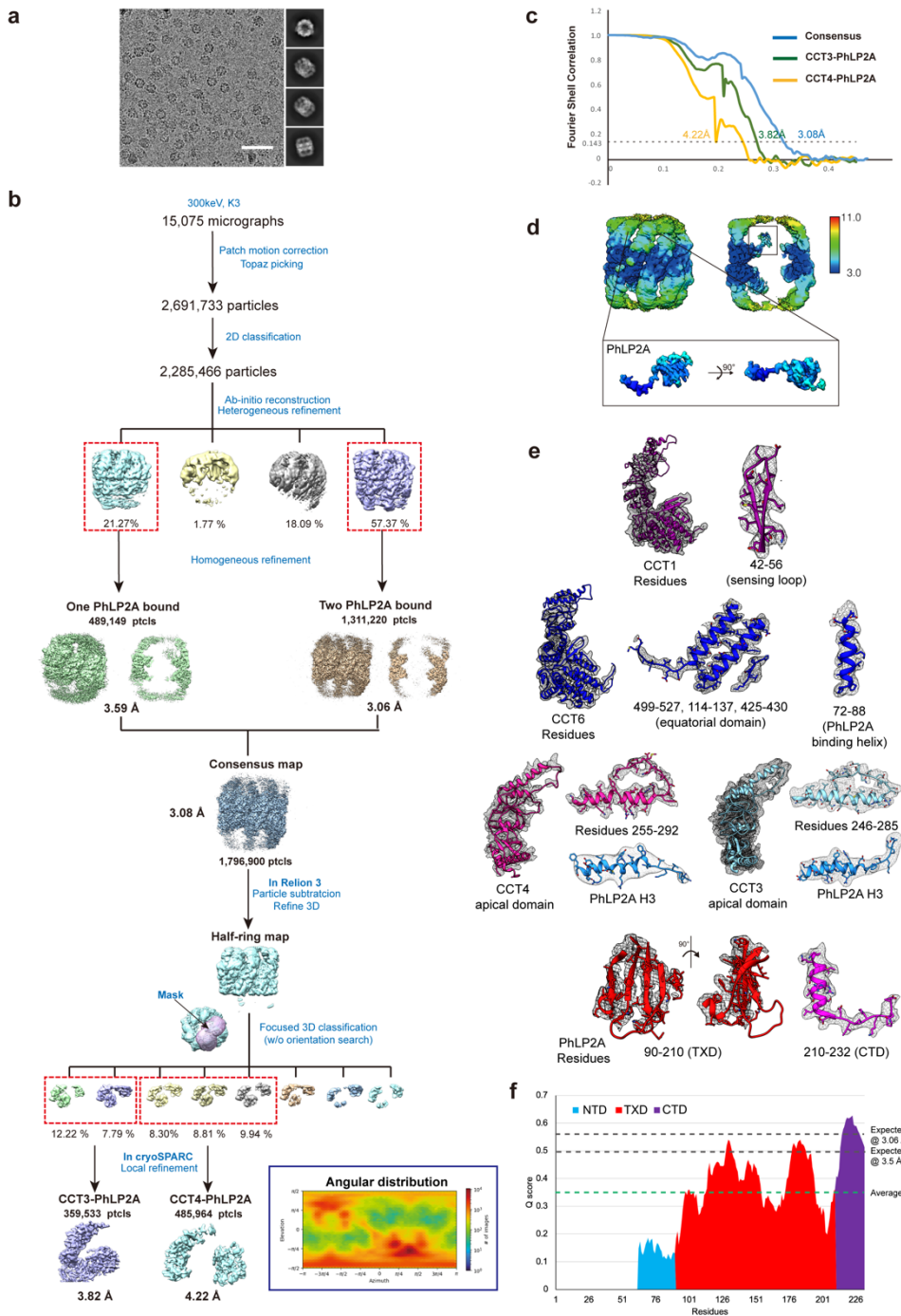


Figure 3.6 Structural analyses on PhLP2A in an open TRiC complex. **a** Representative electron micrograph of open TRiC-PhLP2A. scale bar, 50 nm. Averaged 2D classes showing top, tilted, and side views are displayed at the right side. **b** Workflow of cryo-EM data processing. A diagram for angular distribution of particles

for consensus map is displayed. **c** Fourier Shell correlation (FSC) curve of consensus map (blue), local map of CCT3-PhLP2A (green), and local map of CCT4-PhLP2A (yellow) from focused classification. **d** Local resolution map of consensus map and zoom-in view on PhLP2A encapsulated. **e** Map-model fitting of CCT subunits and PhLP2A. CCT1 and its TXD-interacting nucleotide-sensing loop, CCT6 and its equatorial domain and CTD-interacting helix, and apical domain of CCT3, CCT4 are presented with NTD H3, TXD, and CTD of PhLP2A. **f** Q-score graph of PhLP2A in open TRiC. Each domain is color coded.

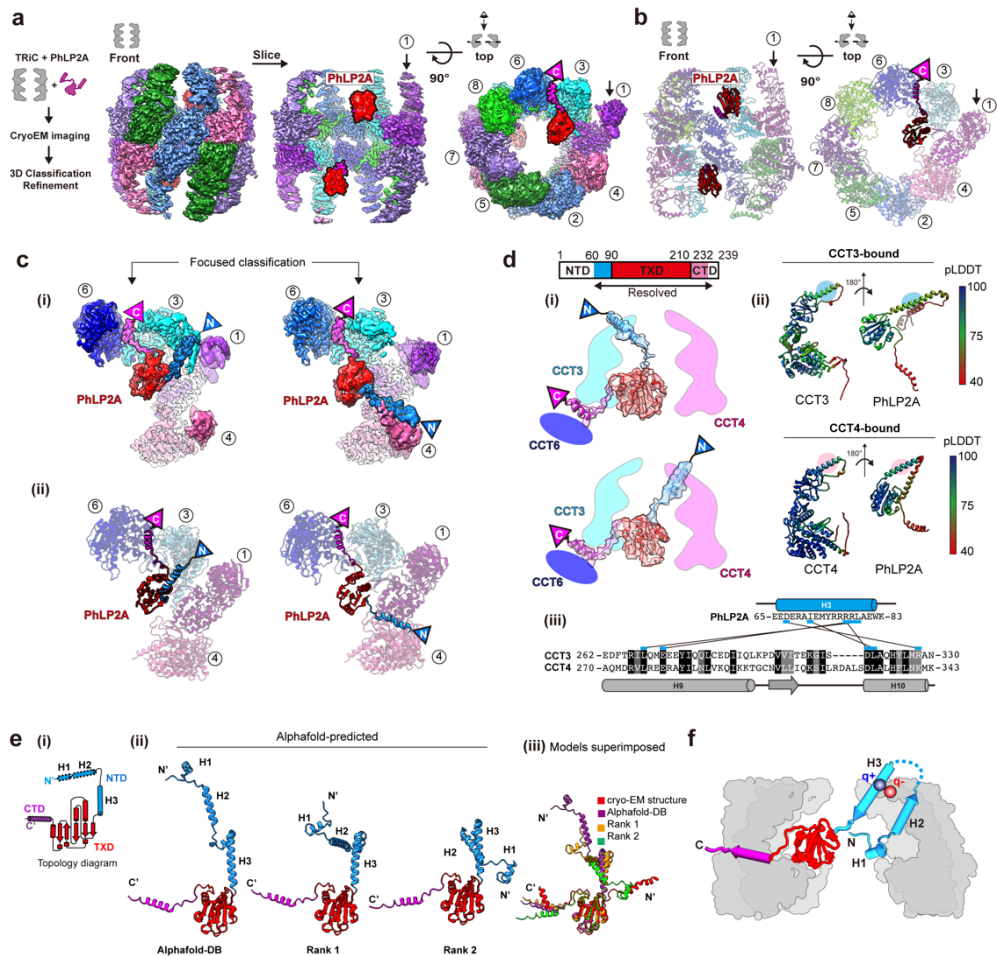


Figure 3.7 Cryo-EM structure of the PhLP2A-open TRiC complex.
a (Left) Schematic of the designed experiment. (Right) Front, slice, and top view of consensus map of PhLP2A encapsulated in the TRiC folding chamber. Each CCT subunit and PhLP2A are color-coded as defined in the top view. **b** The atomic model of the PhLP2A-TRiC complex from the front and top view. CCT subunits and PhLP2A are color-coded as in a. **c** Two binding modes of the PhLP2A NTD are revealed by 3D-focused classification. (i) Densities of CCT3 or CCT4 bound to PhLP2A. (ii) Atomic models of the complexes of the PhLP2A NTD and CCT3 or CCT4 using AlphaFold prediction. Each domain of PhLP2A is color-coded: NTD: dodger blue, TXD: red, CTD: dark magenta. **d** (i) Schematic diagram of PhLP2A and the CCT3/4 complex. The colored box indicates the modeled residues of

PhLP2A with each domain color-coded. (ii) AlphaFold prediction of each complex with a per-residue confidence score (pLDDT) diagram. (iii) Sequence alignment of H9 and H10 of CCT3 and CCT4 at the major interaction site of PhLP2A. Predicted interactions between CCTs and PhLP2A are labeled with black lines. **e** (i) 2D topology diagram of PhLP2A. Each domain is color-coded as indicated in c. (ii) Three representative structures of AlphaFold-predicted full-length models of PhLP2A, color-coded in a domain-wise manner and (iii) superposition of the three models with the experimental model. **f** Schematic representation of PhLP2A topology in an open TRiC chamber. While CTD and TXD are anchored near the equatorial domain of CCT3/6, N-terminal helices can adopt various topologies and reside inside the folding chamber.

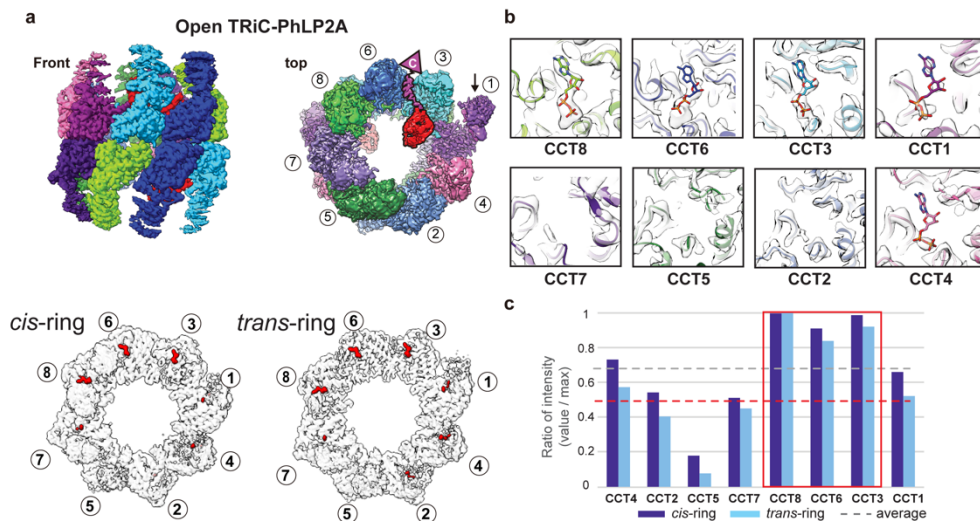


Figure 3.8 Analyses on ATP binding pocket in an open TRiC-PhLP2A complex **a** (Top) cryo-EM structure of open TRiC-PhLP2A complex without nucleotide supplemented from this study, (bottom) Density of ATP binding pocket occupied with nucleotide on *cis*- and *trans*-ring of TRiC complex. Density corresponds to the nucleotide on each ATP binding pocket is segmented and colored red. **b** Zoom-in view on ATP binding pocket on each CCT subunit, showing different masses depending on different subunits. While CCT8/6/3 show density where nucleotide can fit, other CCT subunits, especially CCT5, show relatively weak densities on the pocket. **c** A graph of the relative intensity of ATP binding pocket on each CCT subunit. The mass of each segmented volume was calculated using ChimeraX Measure volume tool, and the ratio to the maximum volume of the ATP binding pocket was presented. CCT3/6/8 shows significantly higher intensity in comparison with others. Deep blue and sky blue: mass of each CCT subunit in *cis*-ring and *trans*-ring, respectively. Light gray dashed line: average of the ratio values, red dashed line: ratio value of 0.5.

domain where H3 of PhLP2A binds via electrostatic charge interaction. **c** Surface hydrophobicity of PhLP2A and the open TRiC chamber. Interactions between PhLP2A and TRiC are as indicated in **b**. While other binding sites are mainly hydrophilic, the TXD binding interface between CCT1/3 and the CTD binding crevasse between CTD3/6 are hydrophobic.

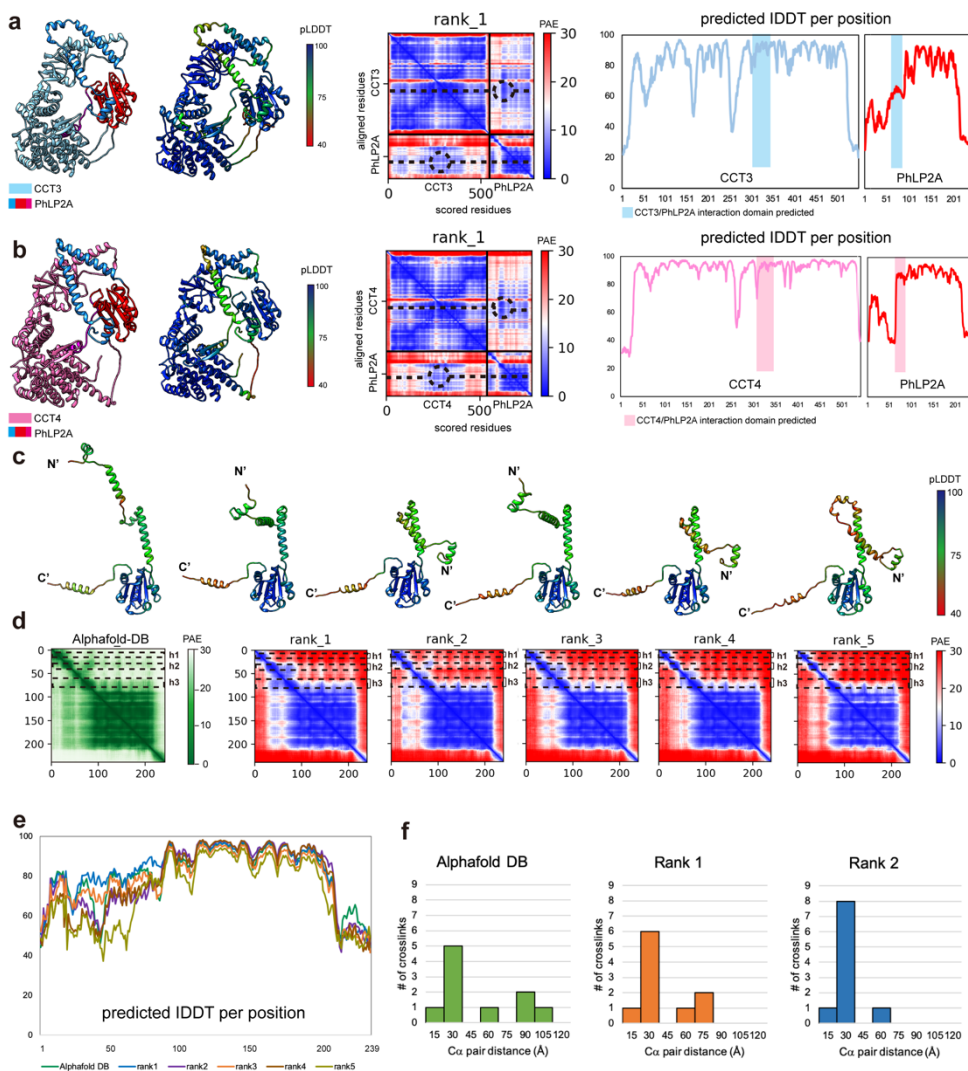


Figure 3.10 Alphafold-adopted model building and crosslinking assay of PhLP2A. **a** Alphafold prediction of a dimeric complex of PhLP2A-CCT3. Models of per-residue confidence score (pLDDT) colored surface, PAE graph with binding surface labeled with a dashed circle, and pLDDT graph are presented. **b** Alphafold-predicted model of PhLP2A-CCT4 and validation graphs. The binding surface between H3 of PhLP2A and H9 on the apical domain of CCT is conserved as observed. **c** Six Alphafold-predicted models of PhLP2A, either AlphaFold-DB deposited or predicted models using Colabfold from rank1 to rank 5. Each model is colored with a pLDDT score representing the surface. **d, e** PAE and pLDDT graph of six Alphafold-predicted models. **f** $C\alpha$ distance graph of intramolecular

crosslinks measured on three different Alphafold-predicted models.

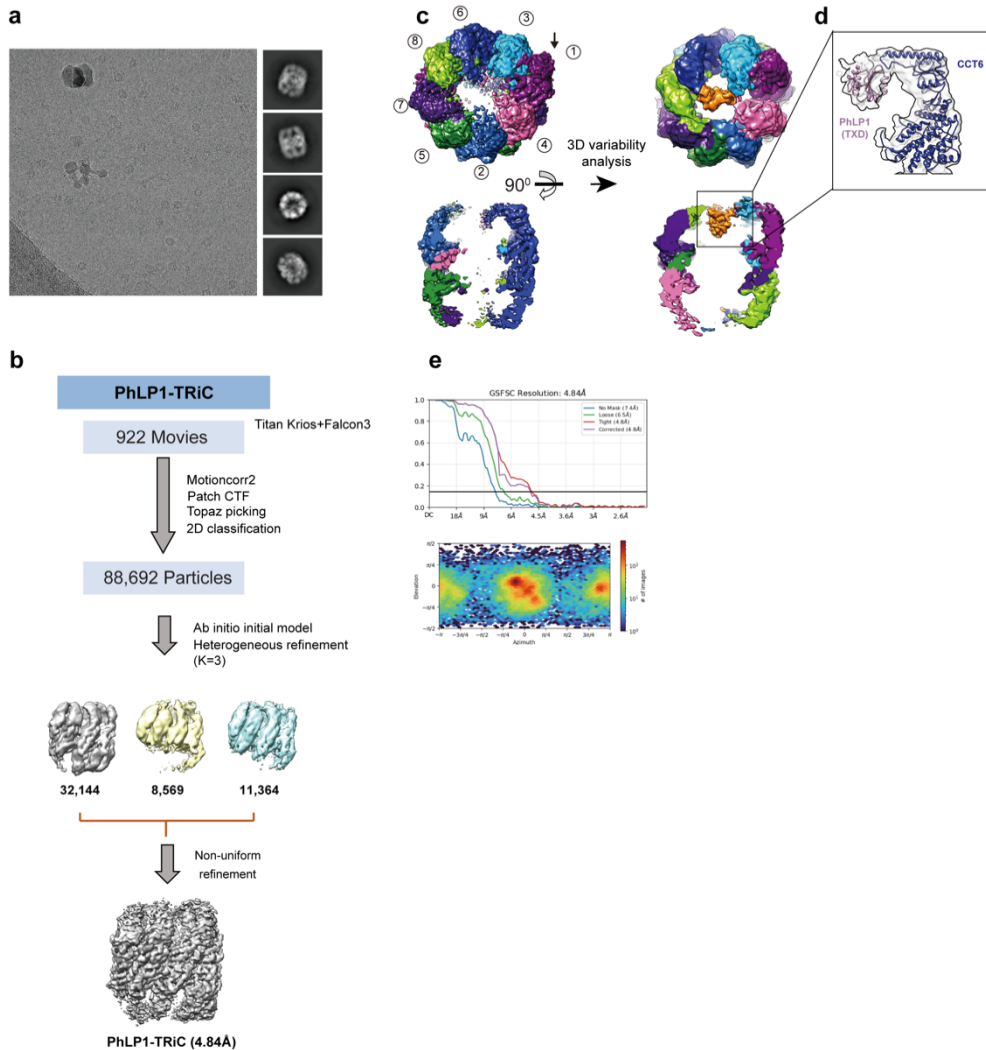


Figure 3.11 Cryo-EM structure of open PhLP1-TRiC **a** Representative electron micrograph of open TRiC-PhLP1. Averaged 2D classes showing tilted, side and top views are displayed at the right side. **b** Workflow of cryo-EM data processing. **c** Top and side slice view of cryo-EM map of open consensus TRiC-PhLP1 (left). An open TRiC-PhLP1 map after 3D variability analysis (right). The extra density is indicated by orange color. **d** PhLP1 and CCT6 subunit model fitted to cryo-EM density map. **e** A Fourier Shell correlation (FSC) curve of consensus map and a diagram for angular distribution of particles for consensus map is displayed.

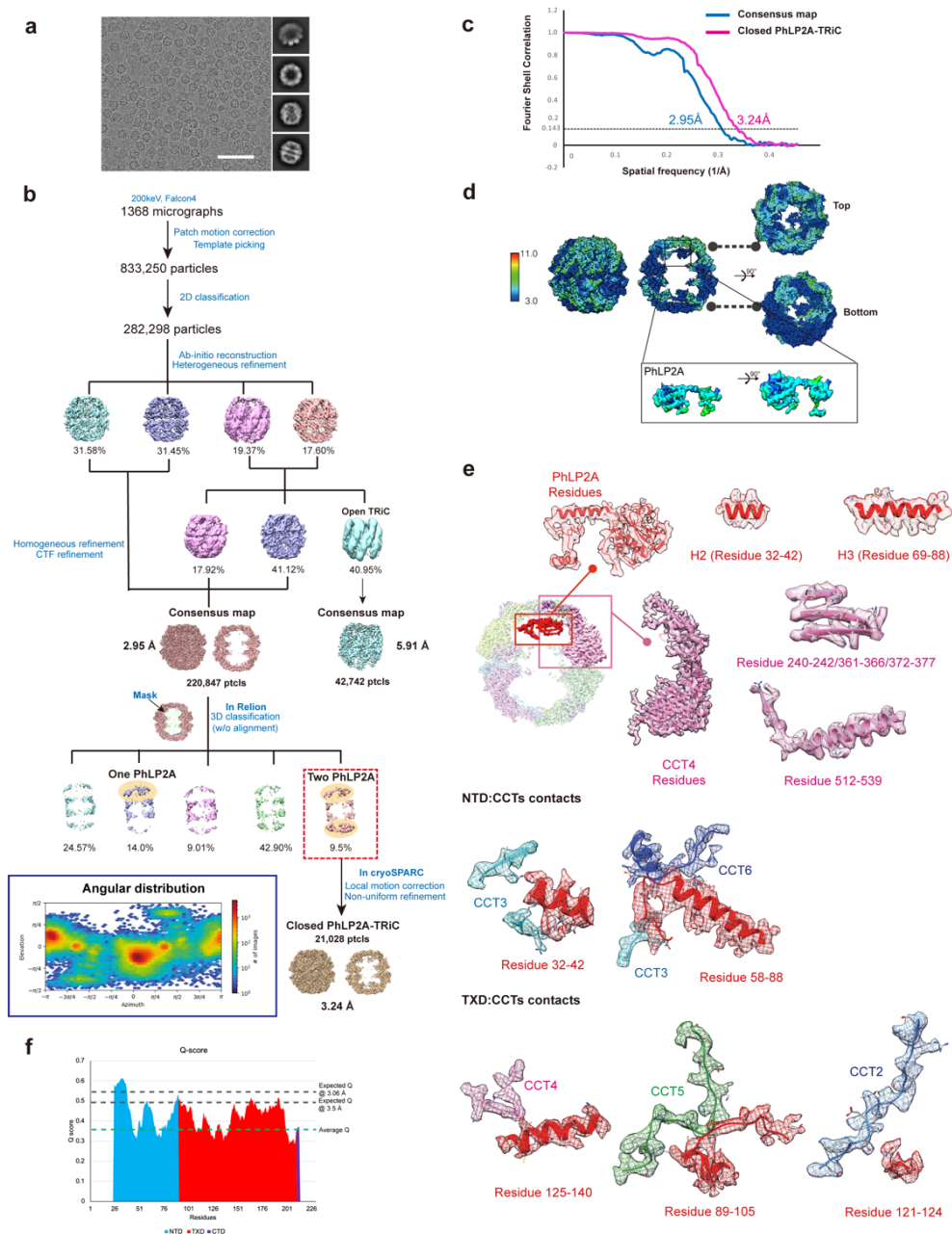


Figure 3.13 Cryo-EM structure of PhLP2A in closed TRiC. **a** Electron micrograph of closed TRiC-PhLP2A. Representative 2D classes of tilted, top, and side view are shown at right. scale bar, 50 nm. **b** Data processing workflow of PhLP2A-closed TRiC and a diagram for particle angular distribution. **c** Fourier Shell Correlation (FSC) curve of structures of PhLP2A-closed TRiC. Consensus map and the map from focused classification are color coded in dodger blue and deep pink, respectively. **d** Local resolution map of PhLP2A-

closed TRiC and zoom-in view on PhLP2A encapsulated inside a folding chamber. **e** Map-model fitting. CCT4 and newly resolved H2 and H3 of PhLP2A are shown individually. Map-model fitting on contacts between NTD:CCT and TXD:CCT are presented together. **f** Q-score graph of PhLP2A to corresponding electron density.

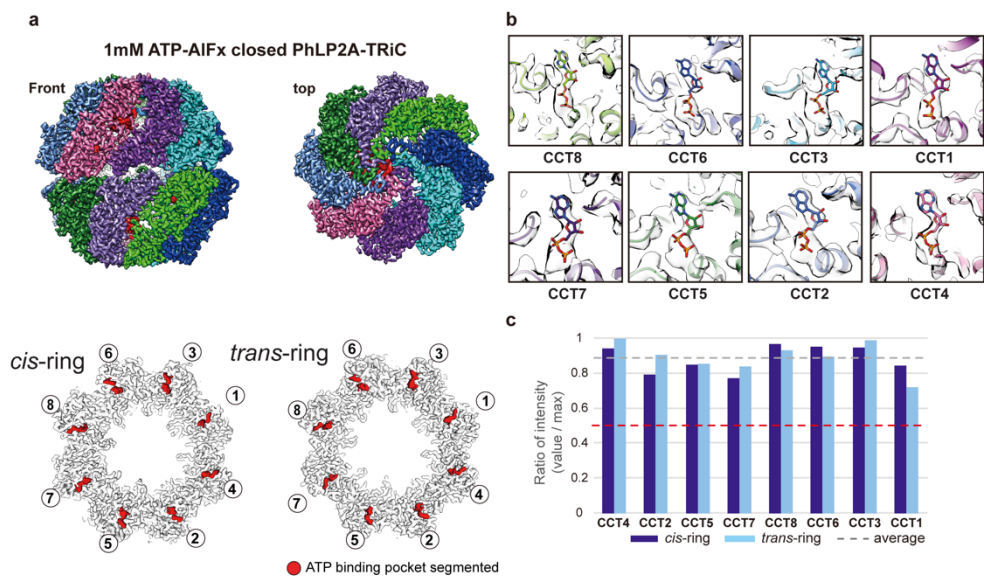


Figure 3.14 Analyses on ATP binding pocket in a closed TRiC-PhLP2A complex **a** (Top) cryo-EM structure of closed TRiC-PhLP2A induced by 1mM ATP/AIFx. (bottom) Density of ATP binding pocket occupied with nucleotide on cis- and trans-ring of TRiC complex. **b** Zoom-in view on ATP binding pocket on each CCT subunit. **c** A graph of the relative intensity of ATP binding pocket on each CCT subunit. The mass of each segmented volume and the ratio to the maximum value from the molecule are calculated.

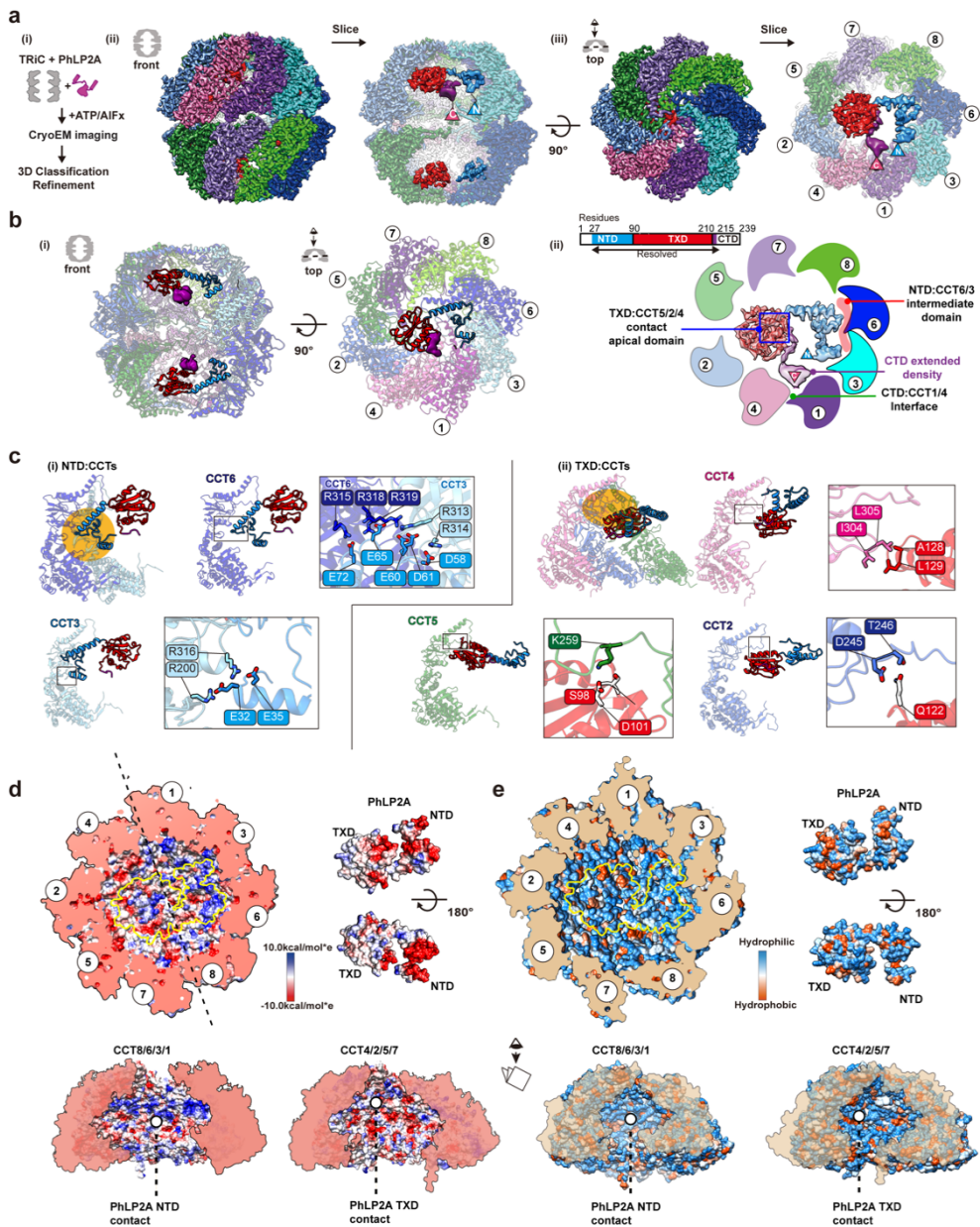


Figure 3.15 Structure of PhLP2A inside TRiC chamber after chamber closing. **a** Cryo-EM structure of PhLP2A inside the closed TRiC chamber after ATP hydrolysis. (i) Cryo-EM imaging preparation scheme. (ii) Front and slice view of the closed PhLP2A-TRiC complex. N- and C-terminus of PhLP2A are labeled in the map. (iii) Top and slice view of the closed PhLP2A-TRiC complex. Due to the varying resolution, the PhLP2A density is shown at different thresholds according to the protein domains. Note that both folding chambers can be occupied by PhLP2A, as in open-state TRiC. **b** (i)

Model of PhLP2A inside the closed TRiC chamber. The CTD is not modeled and the lowpass filtered electron density is shown instead. (ii) Summary of binding sites between PhLP2A and the closed TRiC chamber. Compacted NTD helices interact with the intermediate domain of CCT3/6 (colored in red) and the following TXD interacts with the apical domain of CCT5/2/4 (marked by a blue box). Note that although these domains are not resolved to the atomic level, the density map at the lower contour level shows the NTD close to CCT1/3 and the CTD close to the equatorial domains between CCT4/1. **c** Zoom-in view of the domain-wise interaction between PhLP2A and CCT subunits. (i) Molecular contacts between CCT 3/6 and the NTD of PhLP2A and (ii) between CCT5/2/4 and the TXD of PhLP2A. Contact areas are indicated by a yellow circle. Residues making contacts are displayed and labeled. **d** Electrostatic surface charge showing charge complementarity between PhLP2A and the closed folding chamber. The positively charged half hemisphere of CCT1/3/6/8 provides a binding surface for the negatively charged PhLP2A NTD. **e** Hydrophobic surface charge of closed folding chamber and PhLP2A. While the inner wall of the chamber is mostly hydrophilic and charged, part of the surface composed of CCT5/2/4 provides hydrophobic patches for PhLP2A TXD to bind on.

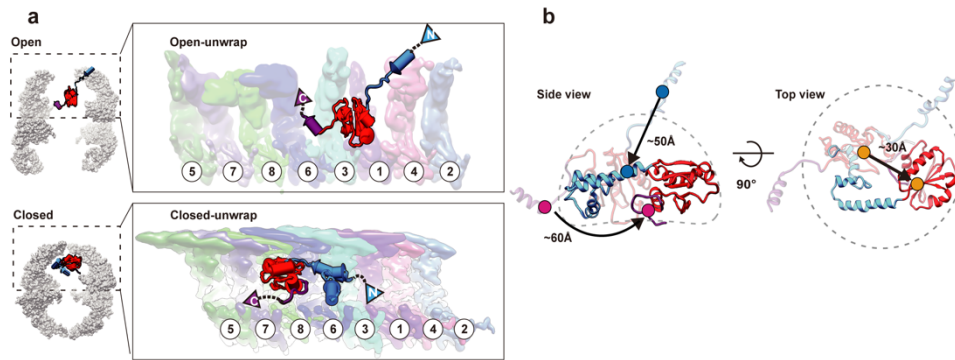


Figure 3.16 Relocation of PhLP2A upon ATP dependent TRiC cycle.
a Global rearrangement of PhLP2A in the TRiC folding chamber in the unwrapped view. (Top) Unwrapped view of PhLP2A in which NTD is in the expanded form in TRiC in the open conformation. (Bottom) Unwrapped view of PhLP2A in the closed conformation of TRiC. Note that PhLP2A NTD is compacted and constrained. **b** Conformational and orientation changes of PhLP2A in the open or closed TRiC folding chamber. PhLP2A NTD undergoes an orientation change of about ~ 50 Å from extended outward to bent inward, closer to the TXD. The TXD is lifted about ~ 30 Å from the equator to the apical contact through flipping but retains its conformation. The CTD moves ~ 60 Å following the movement of TXD.

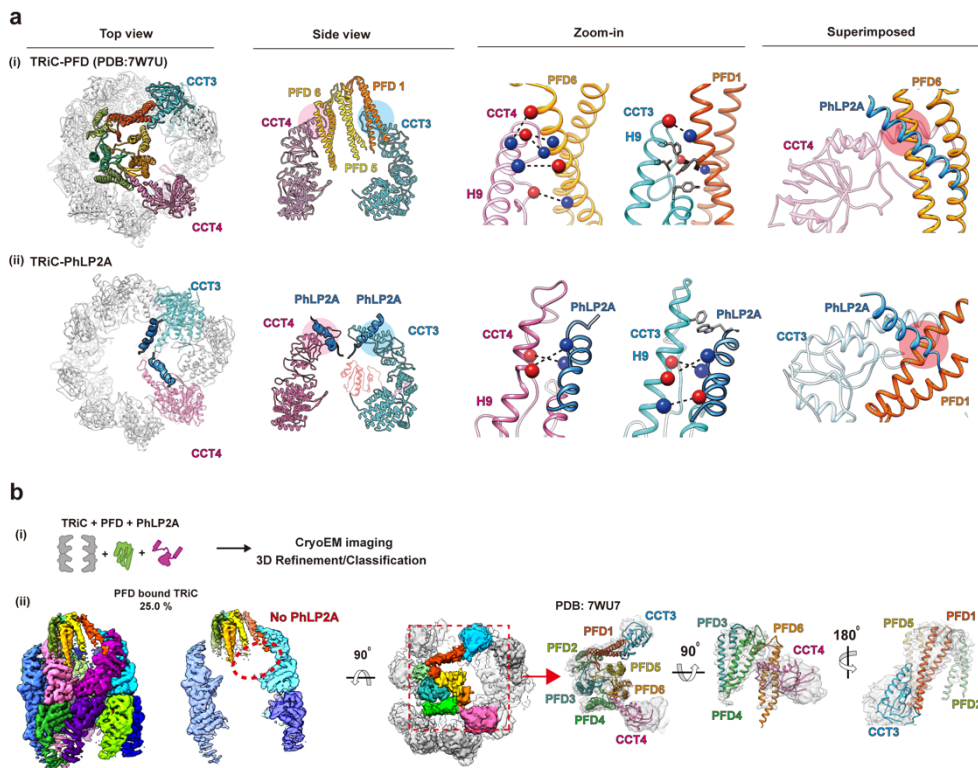


Figure 3.17 PhLP2A modulation on the PFD-TRiC network. **a** Atomic models of (i) PFD-bound TRiC (PDB:7WU7) and (ii) PhLP2A-bound TRiC. CCT3, CCT4, PFD and the PhLP2A NTD are highlighted. Contacts between TRiC and PFD or PhLP2A are indicated as colored-circles in the side view. Zoomed-in view of each contact between TRiC (CCT3, CCT4) and the cochaperones (PFD, PhLP2A). Negatively charged residues are indicated by red balls while positively charged residues are indicated by blue balls. Other residues are shown as stick cartoons. PFD and PhLP2A models are superimposed on their binding sites of CCT3 or CCT4. Red circles indicate the clash between the molecules. **b** (i) Schematic of the designed experiment. (ii, iii) 3D classification reveals PFD-bound TRiC (25.0%) and PhLP2A-bound TRiC (22.9%), respectively. The PFD-TRiC atomic model (PDB: 7WU7) fitted to the PFD-bound TRiC density. The red circle indicates no detectable PhLP2A density while the yellow circle indicates no detectable PFD density.

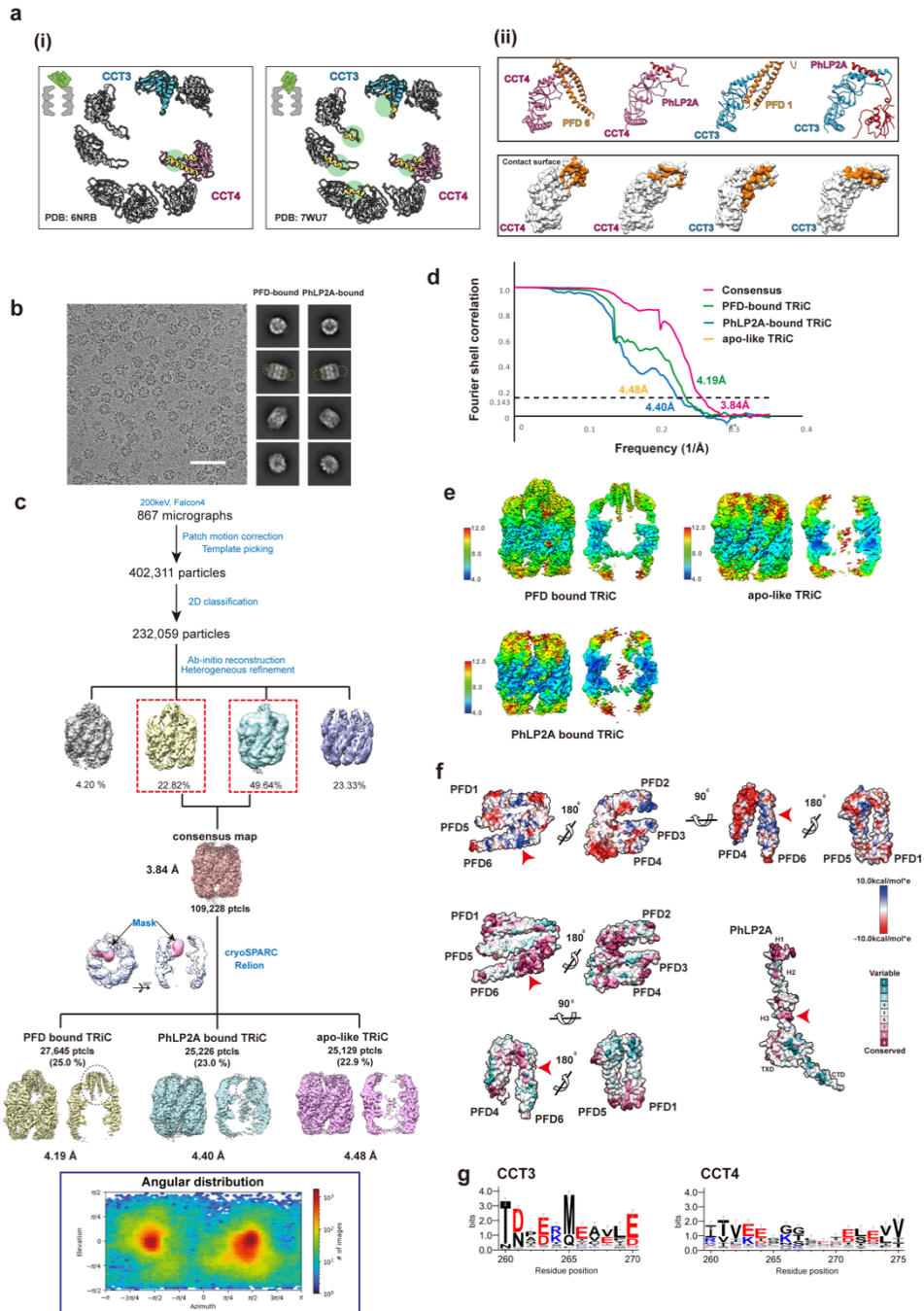


Figure 3.18 The direct competition between PFD and PhLP2A. **a** (i) TRiC contact points for PFD from two distinct conformations (latched, engaged) highlighted with green circles. (ii) The ribbon diagrams of TRiC contact points for PFD subunits (PFD1, 6) and PhLP2A (PhLP2A NTD). The surfaces of CCT3 and CCT4 are shown and the

contact area from PFD and PhLP2A is colored in orange. **b** Representative cryo-EM micrograph and 2D averages of PFD-bound TRiC and PhLP2A-bound TRiC. scale bar, 50 nm. **c** The workflow of cryo-EM data processing (top) and a diagram for particle angular distribution (bottom). **d** The Fourier shell correlation (FSC) curve. **e** Local resolution map shown in color coded. **f** (Top) The surface charge distribution of PFD subunits and (bottom) the surface of PFD and PhLP2A colored by residue conservation score. The red arrow indicates PFD and PhLP2A binding site. Each conservation score of PFD subunits and CCT subunits is independently calculated and normalized using Consurf. **g** Logo plot of the conservation of CCT3 and CCT4 making contacts with PhLP2A or PFD.

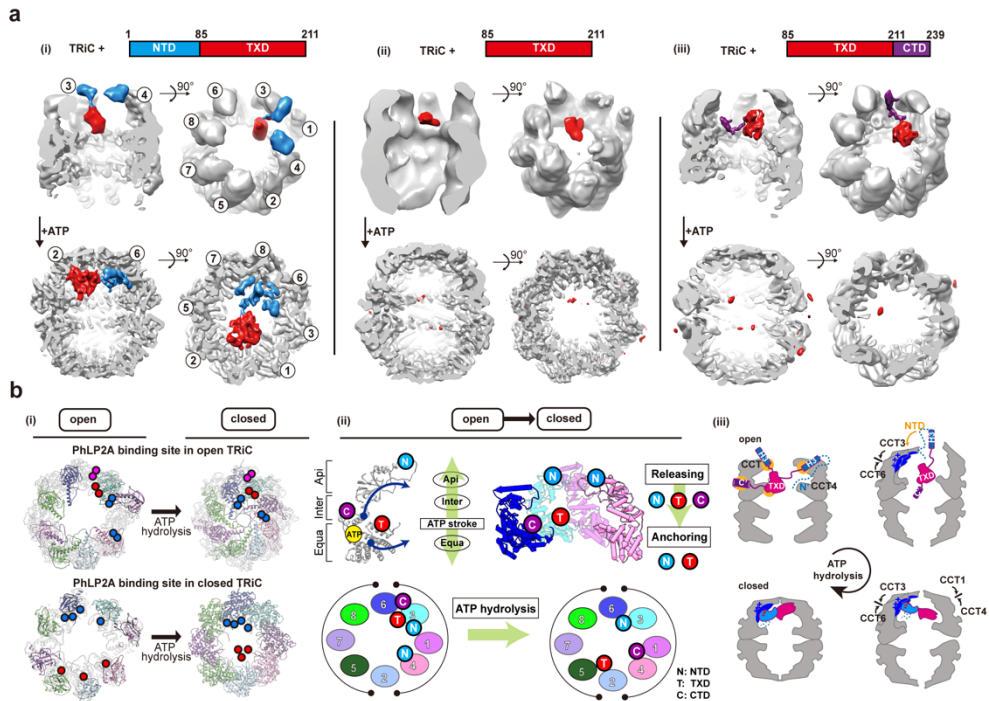


Figure 3.19 Domain-wise characteristics of PhLP2A in relationship with TRiC. **a** Cryo-EM structures of three truncated mutants inside the TRiC in the open state and after ATP hydrolysis. (i) TRiC with NTD + TXD: attributable NTD density at the apical domain with TXD and NTD + TXD orients like WT PhLP2A in closed TRiC. (ii) TRiC with TXD: attributable density of TXD at low resolution at the equator, but no attributable density in closed TRiC. (iii) TRiC with TXD + CTD: CTD anchor shows high-resolution features like WT PhLP2A between CCT3/6 and TXD close to CCT3, but no attributable density in closed TRiC. **b** (i) Schematic diagram of PhLP2A domain-wise interaction with the TRiC chamber in open (left) and closed conformation (right). Colored circles indicate interacting residues in open TRiC and closed TRiC and their movements during the ATP cycle. Each PhLP2A domain is color-coded. (ii) ATP hydrolysis event in CCT subunits cascades the releasing and re-anchoring process of PhLP2A. N: NTD, T: TXD, C: CTD. (iii) Diagram of releasing of PhLP2A upon ATP-dependent cycle of TRiC. Source data are provided as a Source Data file.

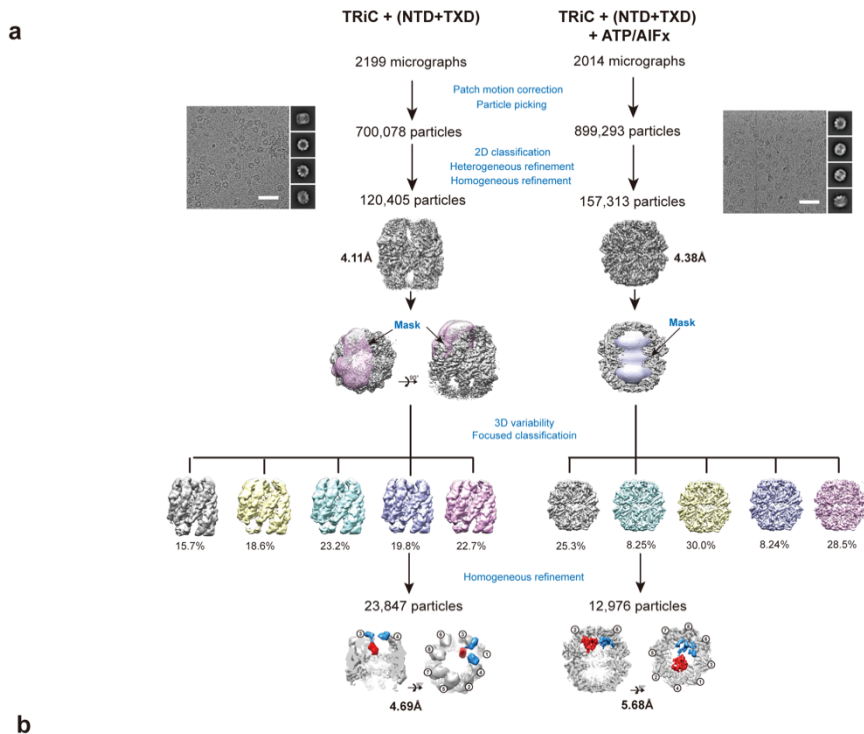


Figure 3.20 Cryo-EM processing workflow of truncated PhLP2A:TRiC complex. **a** Cryo-EM data processing workflow of TRiC incubated with NTD-TXD protein in open (left) and closed (right) states with representative micrograph and 2D class averages. scale bar, 50 nm. **b** Table showing population and percentages of encapsulated PhLP2A WT or different constructs of PhLP2A in TRiC at open and closed states.

3.3. Structural study of TRiC for substrate folding

3.3.1. Structural analysis of substrate-free apo closed TRiC

After substrate delivery to TRiC, substrates are released into the inner chamber upon ATP hydrolysis-induced chamber closure. To understand and visualize the folding process inside the chamber, we aimed to first resolve the structure of substrate-free apo closed TRiC as a control. The substrate-free apo closed TRiC was incubated with ATP-AlFx and subjected to cryo-EM analysis. I obtained a cryo-EM map with a resolution of approximately 3.21 Å based on ~13k particles (Figure 3.21a, Figure 3.21b). Then, previously reported closed TRiC atomic model⁴² was fitted to the electron density map and showed well-resolved secondary structures and residue sidechain.

The apo closed TRiC structure displayed the known subunit arrangement, featuring an asymmetric split between a positively charged hemisphere and a negatively charged hemisphere. Notably, the inner chamber of the apo closed TRiC was clean and empty, with no detectable densities resembling substrates even at low contour levels (Figure 3.21c).

3.3.2. Structural analysis of closed β -tubulin TRiC complex

Next, to understand the fate of the substrate released into the inner chamber after substrate delivery, I aimed to determine the structure of the substrate-bound closed TRiC complex. For this, purified TRiC: β -tubulin complex was used as a model system, and conducted cryo-EM analysis after incubation with ATP-AlFx. Consequently, both open and closed TRiC states were obtained containing β -tubulin-dependent density (Figure 3.22). Similar to previous data, the 3.8 Å resolution open TRiC state exhibited a compact, heterogeneous β -tubulin-dependent density in the inter-ring space. In contrast, the structure of closed TRiC revealed β -tubulin repositioned into one chamber, with well-defined secondary structural elements (Figure

3.23a). However, the local resolution of β -tubulin varied across different regions, and further heterogeneity analysis uncovered partially folded β -tubulin densities (Figure 3.23b). Each of these β -tubulin densities was reconstructed into cryo-EM maps with resolutions ranging from 2.9 Å to 3.6 Å, all showing well-defined secondary structures (Figure 3.23b). The four β -tubulin structures were aligned in an axis of tubulin domains gradually accumulating suggesting a progressive folding process. Additionally, the C-terminus structure of β -tubulin was observed near the TRiC chamber wall. Atomic models were built based on the four tubulin maps and validated them using Q-scores (Figure 3.23c, Figure 3.23e). High Q-scores were consistently observed in regions where the tubulin density was well resolved, while lower scores were seen in unresolved areas. The Q-scores of four tubulin map and atomic model show distinct patterns, suggesting that the four β -tubulin states represent different folded states. Based on these observations, the conformations were labeled as states I-IV, with state IV corresponding to fully folded tubulin.

The atomic models of states I-IV suggest that β -tubulin undergoes discontinuous domain-wise folding as it progresses through folding intermediates (Figure 3.23c). State I is the least resolved of the four states, containing only the N-terminal β -tubulin domain (residues 1-170), which interacts with the inner chamber wall of CCT6-CCT8 (Figure 3.23d). Additionally, the C-terminal β -tubulin E-hook (residues 438-444) is bound to a pocket between CCT1 and CCT4. State II contains the domains from state I, along with discontinuous elements of the C-terminal domain of β -tubulin, spanning residues 171-203 and 263-267, as well as C-terminal helices 372-426 (Figure 3.23d). This C-terminal domain is anchored to CCT1 and CCT3. State III builds upon state II with the resolution of the folded helical core domain, spanning residues 204-262, 268-272, and 366-371 (Figure 3.23d). Finally, state IV is composed of residues 273-365, forming the mid-domain and completing the structure of the fully folded monomeric tubulin (Figure 3.23d). Although there are minor differences in the C- α backbone RMSD,

most of the folded secondary elements closely resemble the native tubulin structure. These four structural states of β -tubulin suggest a sequential folding pathway in which discontinuous sequence elements fold into specific native-like domains through interactions with the TRiC chamber, ultimately forming the native state (Figure 3.23c, Figure 3.23d).

3. 3. 3. Folding intermediates guided by TRiC subunits

In a previous report, it was shown that the TRiC inner chamber wall exhibits an asymmetric electrostatic charge distribution, after ATP hydrolysis and ring closure³⁰ (Figure 3.24c). To explore the role of charged chamber for β -tubulin folding, we analyzed the interactions between the TRiC chamber and each β -tubulin folding intermediate state. In all β -tubulin folding intermediates, the N-terminal domain is highly negatively charged and forms complementary interactions with the positively charged walls of CCT6 and CCT8. Additionally, the flexible, negatively charged C-terminal E-hook tail of β -tubulin anchors itself into a positively charged pocket between CCT1 and CCT4 (Figure 3.24a, Figure 3.24b). In states II-IV, the folded C-terminal β -tubulin domain also forms electrostatic interactions with the positively charged patches on CCT1 and CCT3. These electrostatic interactions remain even after β -tubulin reaches its native folded state (Figure 3.24a). The charged walls of TRiC and the charged domains of β -tubulin segregate the charged region to one side of the TRiC chamber, while the rest topology extend into the central cavity of the chamber.

Next, I examined the specific interactions between β -tubulin folding intermediates and each CCT subunit. In state I, the folded N-terminal domain of β -tubulin forms salt bridges and hydrogen bonds between residues in H2, H3, H4, and the loops H1-S2, H3-S4, and H4-S5 with CCT6 and CCT8 (Figure 3.24d, Figure 3.24e). The β -tubulin E-hook also interacts with the positively charged residues in CCT1 and CCT4, and this interaction is observed across all folding intermediates. In state II, the folded C-domain is anchored through

interactions between H11 and H12 with CCT1 and CCT3 (Figure 3.24f, Figure 3.24g). The C-terminal tail of CCT6 is positioned near the T5 loop of β -tubulin in the C domain, which forms part of the GTP-binding pocket, suggesting that the CCT6 tail may facilitate the formation of the GTP-binding pocket in β -tubulin (Figure 3.24h). In states III and IV, additional interactions with the chamber wall do not accumulate. Instead, the C-terminal tail of CCT2 interacts with the core and M domains of β -tubulin, possibly providing stabilization effect (Figure 3.24h).

Taken together, all β -tubulin folding intermediates exhibit tight interactions with TRiC through a combination of rigid electrostatic interactions with the chamber wall and flexible interactions with the CCT tails (Figure 3.24i). Notably, the negatively charged patches on the N- and C-terminal domains are conserved across α -, β -, and γ -tubulins, suggesting that these tubulins undergo a similar mode of TRiC-facilitated folding (Figure 3.25a). The residues within the TRiC chamber that interact with the tubulin intermediates are also highly conserved (Figure 3.25b). This shows TRiC and tubulin may be co-evolved for folding assistance. Thus, the process of TRiC-mediated folding does not release substrate to freely rotate within the closed chamber; rather, TRiC assists folding by actively orienting and restraining the N-terminal domain and C-terminal tail of β -tubulin (Figure 3.24a).

The four cryo-EM structures demonstrate that during the progressive folding process, different folding intermediates of β -tubulin are involved in interactions with distinct CCT subunits and the intrinsically disordered CCT tails. These interactions accumulate throughout the progressive folding process, guiding the folding of β -tubulin until it reaches the fully folded state (Figure 3.26a). The folding intermediate structures also demonstrate how TRiC helps circumvent the challenges posed by the folding of aggregation-prone β -sheets. The β -tubulin folding intermediates show that anchoring of the N-terminal domain towards the TRiC chamber provides directional guidance for the formation of a hydrophobic β -sheet, allowing the sheet to grow towards the interior of the chamber

(Figure 3.26b). Comparing state I through IV, each intermediate structure adds another β -strand layer to the exposed hydrophobic core, priming it for the next folding step. Importantly, helices and loops are added to the β -sheet, protecting its exposed edges and reducing the potential for off-pathway folding events. This interaction with TRiC helps shape the tubulin folding landscape by preventing trapped folding intermediates and reducing frustration in the folding process (Figure 3.26b).

3. 3. 4. Evolutionary analysis of TRiC required substrate folding

Eukaryotic tubulin is an obligate substrate for TRiC, requiring the TRiC for proper folding. In contrast, its prokaryotic homolog, FtsZ, can undergo spontaneous folding without the need for a chaperone^{139,140}. Both proteins share structural similarities with other superfamily members from prokaryotes and archaea, particularly in their domain organization and the extended core β -sheet (Figure 3.27a, Figure 3.28a, Figure 3.28b)^{139,141-143}. However, eukaryotic tubulins possess unique features that allow for specialized functions, such as remodeling of GTP affinity, changes in hydrolysis kinetics, the ability to form lateral microtubule contacts, and binding with microtubule-associated proteins (MAPs)^{139,142,144,145}. These specific tubulin functions are likely to be supported by structural insertions, such as in the H1-S2 loop, two negatively charged helices H11 and H12, the E-hook tail, and the remodeling of residues that contact GTP. These structural changes lead to an increase in hydrophobic interdomain interfaces (Figure 3.27a, Figure 3.28c). This addition of domains of eukaryotic tubulins likely prevents them from folding spontaneously or using simpler chaperone systems. Remarkably, the sites of TRiC binding during folding are concentrated on these additional structural features, suggesting that tubulin's specialized functions are closely linked to the need for TRiC assistance during folding (Figure 3.27b).

This hypothesis is more supported by folding observed in the formation of the N-C domain interface in β -tubulin. The T3 loop,

which is crucial for the folded β -tubulin N-C interdomain interface, undergoes a 13 Å C- α variation between state I and state II, indicating significant conformational changes (Figure 3.27c). Closer examination and Q score validation allowed the fitting of bulky side chains like H105 and Y106 and to trace the T3 loop's density (Figure 3.28d). In state I, residues 100-109 of the T3 loop adopt an extended conformation, forming contacts with E202 of CCT3 and D86 of CCT6 (Figure 3.27c). As β -tubulin transitions to state II, a decrease in the resolvability of residues 96-106 suggests a conformational shift as the C domain folds (Figure 3.27c). In states III and IV, the T3 loop stabilizes through interactions with the folded C domain, eventually adopting its native conformation (Figure 3.27c).

In this stabilized conformation, the residue interactions transition from interactions with TRiC to intra-domain contacts within the β -tubulin structure. N99 of the T3 loop is involved in GTP γ -phosphate sensing, and hydrophobic residues like W101 are embedded within the hydrophobic interface between the N and C domains (Figure 3.27c). The folding of the core helix domain completes the GTP binding pocket, consistent with the nucleotide density observed in state III and state IV of β -tubulin (Figure 3.27c). Thus, TRiC holds the T3 loop in an extended state while the C domain is still forming and releases it to allow the loop to adopt its native conformation once the C domain is fully folded.

Additionally, the H1-S2 loop forms polar interactions with the TRiC chamber, indicating that TRiC helps stabilize the inserted β -tubulin loops during folding (Figure 3.27b). Altogether, TRiC helps the stabilization of tubulin's complex topology, which has evolved to perform specialized functions, ensuring its proper folding and functionality.

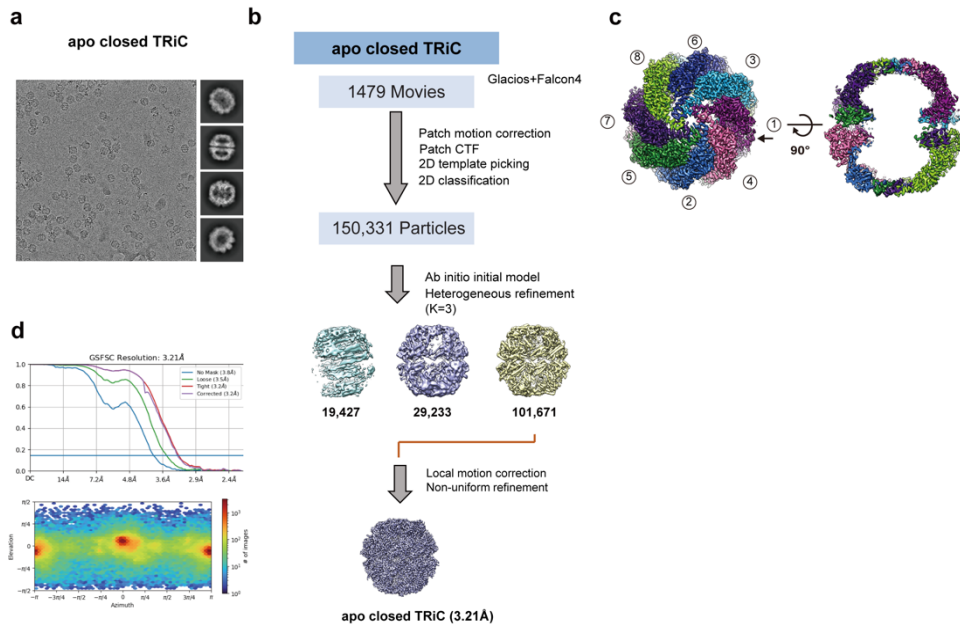


Figure 3.21 Cryo-EM structure of apo closed TRiC. **a** Representative micrograph and 2D class averages of apo closed TRiC with ATP-AIFx. **b** Processing workflow of apo closed TRiC with ATP-AIFx **c** Cryo-EM structure of apo closed TRiC. The black arrow indicates CCT1 subunit. **d** FSC curve of reconstructed maps showing resolution according to the gold standard FSC (0.143 criterion). Euler angle distribution for apo closed TRiC

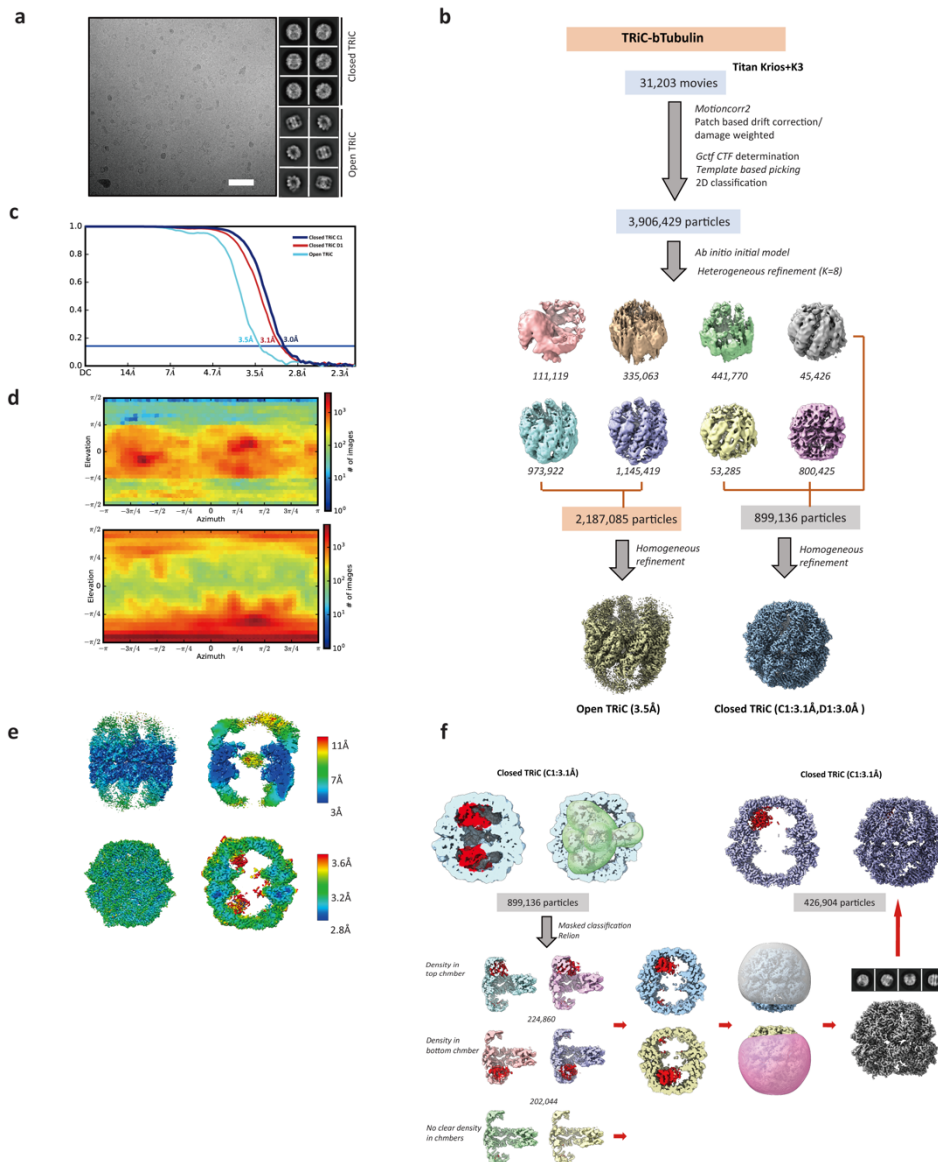


Figure 3.22 Cryo-EM workflow and analysis for TRiC:β-tubulin
a Representative micrograph and 2D class averages of TRiC:β-tubulin with ATP-AIFx. **b** Processing workflow of TRiC:β-tubulin with ATP-AIFx **c** FSC curve of reconstructed maps showing resolution according to the gold standard FSC (0.143 criterion). **d** Euler angle distribution for open TRiC:β-tubulin and closed TRiC:β-tubulin **e** Local resolution map estimation of β-tubulin intermediate states. **f** Focused 3D classification strategy for inner chamber of TRiC. Further analysis identified four progressively folded tubulin conformations inside the chamber: State I (41% of the rings); State II (16% of the

rings); State III (34% of the rings) and State IV (9% of the rings) corresponding to folded tubulin.

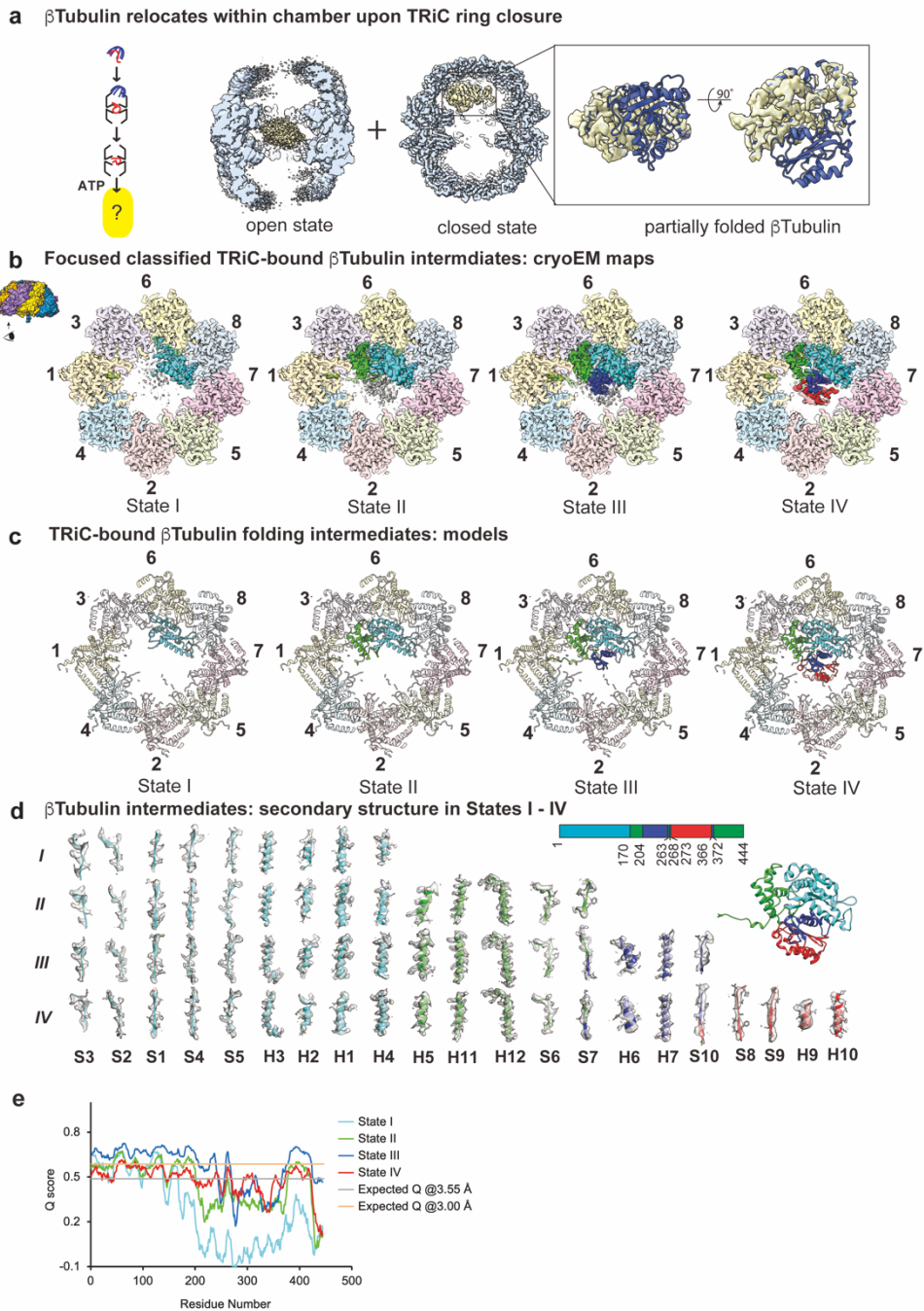


Figure 3.23 Cryo-EM identifies β -tubulin folding intermediates in ATP-driven closed TRiC chamber **a** Cryo-EM consensus maps of open and closed TRiC: β -tubulin indicates dramatic repositioning of β -tubulin density. **b** Focused classification on β -tubulin in the closed state identified four distinct states I-IV that could be separated by the amount of progressively folded β -tubulin relative to the final

state of β -tubulin. **c** Atomic models of TRiC-bound β -tubulin folding intermediates. **d** Local resolvability of secondary structure elements in β -tubulin folding intermediates reveals progressive formation of folded domains. **e** Q-score plots of the β -tubulin intermediate states shown with the expected Q-score according to 3.55 and 3.00 Å.

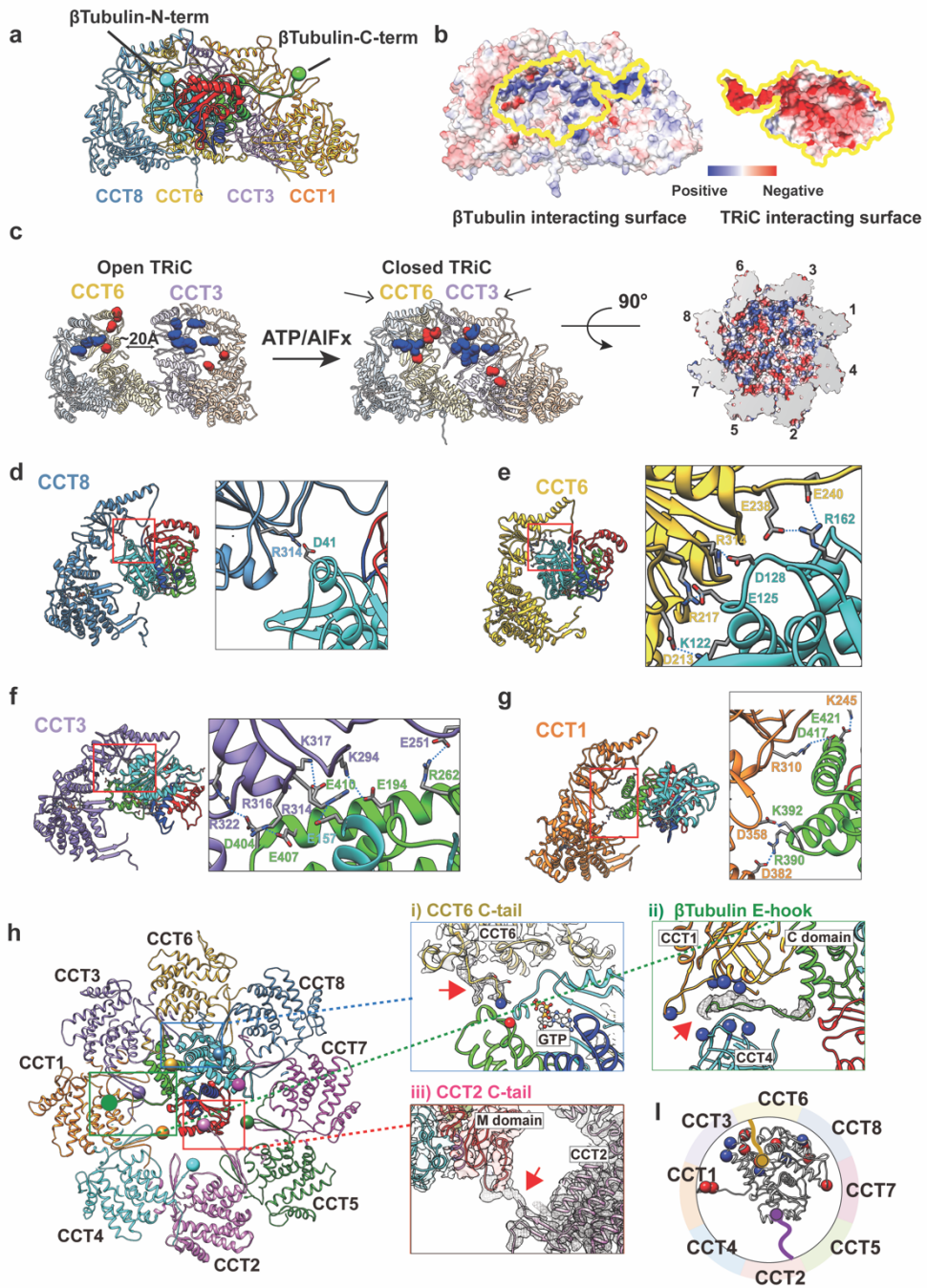


Figure 3.24 TRiC and β -tubulin interaction in a domain-specific manner **a** Side view of a ribbon diagram of β -tubulin and the CCT subunits (1,3,6,8) that have a large contact interface. The β -tubulin N and C termini are indicated as a cyan and green ball, respectively. **b** The surface electrostatic distribution of the interacting surfaces of CCT (1,3,6,8) and β -tubulin. **c** The formation of the electrostatic

patch inner chamber of CCT (1,3,6,8) induced by the ring closure and the asymmetric charge distribution. **d, e, f, g** Side view of CCT (1,3,6,8) and β -tubulin. β -tubulin is colored by progressively folded domains. Residues making salt bridges are labeled, and side chains are displayed with contact shown as a dotted line. **h** Specific tail contacts between TRiC and β -tubulin. Magnified views are displayed for (i) the CCT6 C tail and β -tubulin GTP binding pocket, (ii) β -tubulin CCT1/4 binding pocket and β -tubulin C-terminal E-hook tail, and (iii) CCT2 C tail and β -tubulin M domain. **i** Schematic of β -tubulin. Negatively charged residues (red) and positively charged residues (blue) that contact TRiC are indicated by spheres; the CCT2 (purple) and CCT6 (gold) C-terminal tails are also displayed with spheres on the terminal residue.

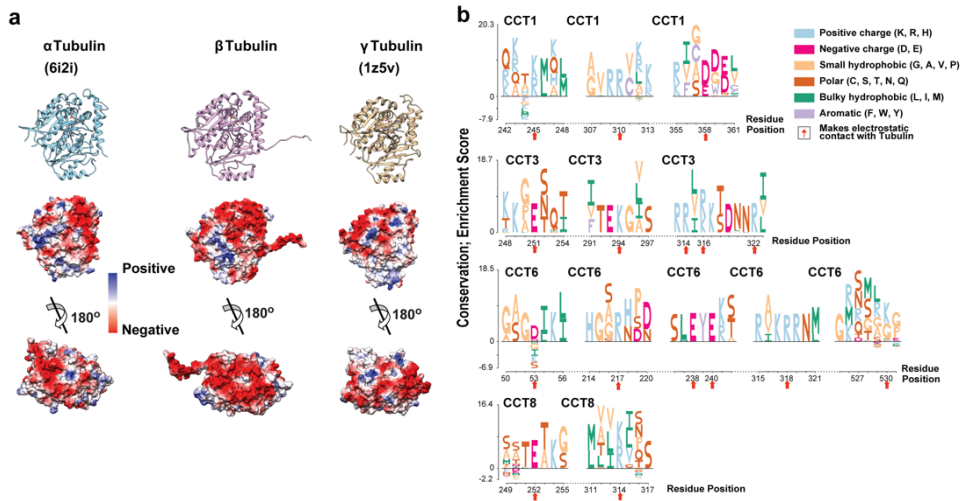


Figure 3.25 TRiC chamber spatially orients and restrains β -tubulin
a Electrostatic surface display of human α -tubulin (PDB:6I2I)¹⁴⁵, β -tubulin (PDB: this study) and γ -tubulin (1Z5V)¹⁴⁶, respectively. **b** Logo plot of the conservation of CCT residues. The residues making direct contact with β -tubulin are indicated by red arrows.

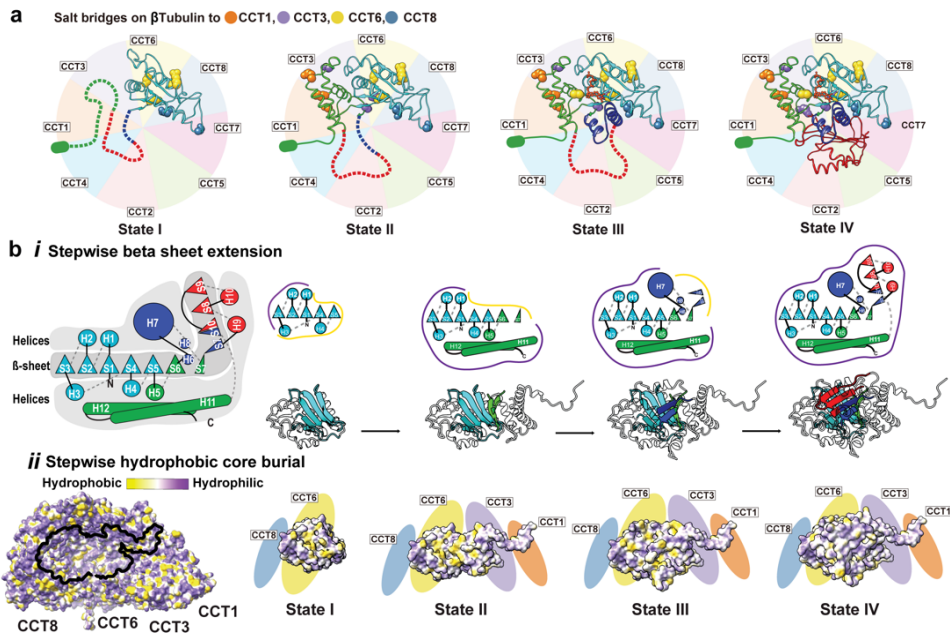


Figure 3.26 The directed folding of β -tubulin intermediates by specific CCT interactions **a** Specific contact between β -tubulin domains and CCT subunits at each intermediate state; salt bridges shown as balls colored according to the interacting CCT subunit. Not-yet-folded domains of each state shown as dotted lines. The negatively charged E-hook annotated as a green ellipse. **b** (i) Cartoon of β -tubulin emphasizes the hydrophobic β -sheet running the length of the β -tubulin structure that is surrounded by α helices, and individual cartoons for the sequential formation of this β -sheet core through each folding state. (ii) Hydrophobicity distribution on TRiC of the β -tubulin interacting surface, and the hydrophobic core burial of β -tubulin as it extends toward the interior of the chamber through the folding states.

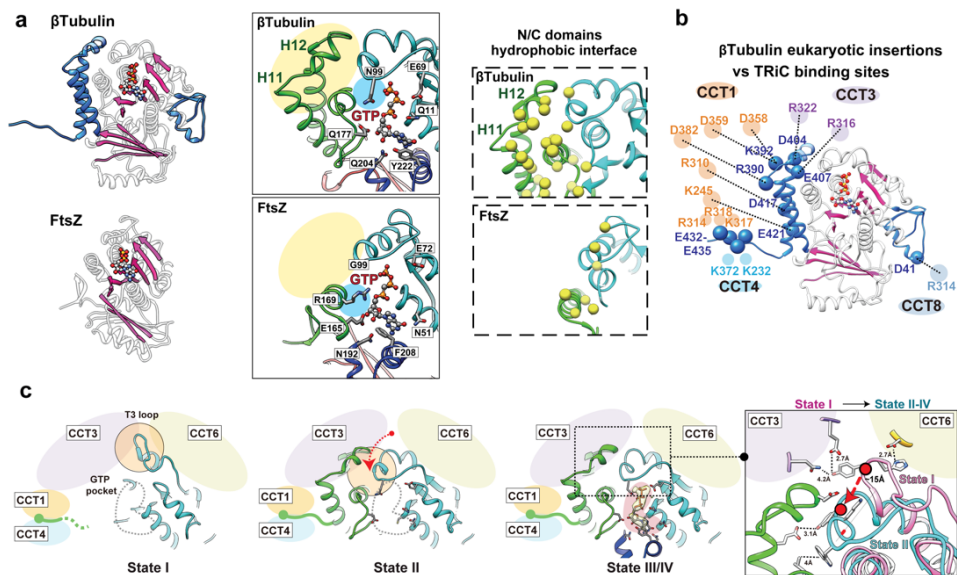


Figure 3.27 Evolutionary analysis and the directed folding of β -tubulin intermediates **a** Ribbon diagram of β -tubulin (PDB: 6I2I, top)¹¹⁷ and FtsZ (PDB: 1FSZ ; bottom)¹⁴⁷; additions unique to β -tubulin structure shown in blue. The overall β -strand folds in β -tubulin and FtsZ are colored in pink. Zoomed-in views of the GTP binding pocket (contacting residues indicated) and N-C domain interface (hydrophobic residues yellow) are shown for comparison. **b** The contacts between β -tubulin specific insertions and CCT subunits are shown with potential salt bridges. **c** Formation of the β -tubulin GTP binding pocket through β -tubulin intermediates. GTP pocket is indicated as a gray dotted line in states I and II; density map corresponding to the nucleotide displayed as a yellow density with pink background in state III/IV. T3 loop makes a large conformational change between state I and the other states indicated by the red arrow and displayed in the focused overlay between states I and II-IV.

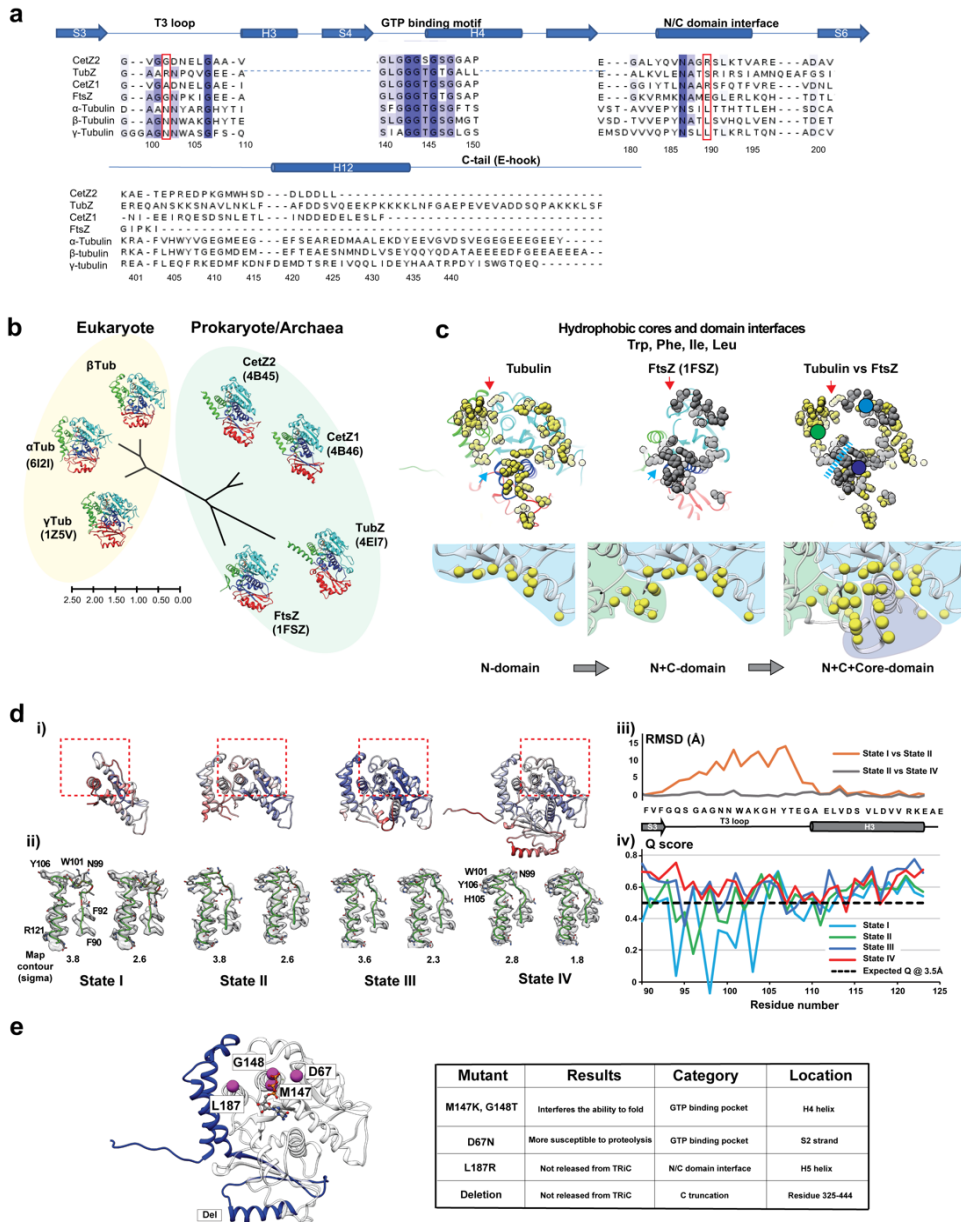


Figure 3.28 Tubulin coevolved with TRiC for directed folding process. **a** Sequence alignment for selected areas of human α -, β -, γ -tubulins and archaeal/prokaryotic homologues (CetZ1: *H. Volcanii*/CetZ2: *H. Volcanii*, FtsZ: *M. jannaschii* and TubZ: *B.cereus*). T3 loop, GTP binding motif, N/C-domain interface and C-domain including H12 and E-hook are represented. Red box indicates conserved N99 and L189 in T3 loop and N/C-domain interface in human tubulins. **b** Phylogenetic tree of tubulins and their

structures^{117,146-149}. Structures are colored in domain (N-domain: cyan, C domain: green, Core domain: blue, M-domain: red). The scale bar represents the number of amino acids substitutions per site. **c** The hydrophobic core and domain interfaces of β -tubulin and FtsZ with hydrophobic residues (Trp, Phe, Ile, Leu) highlighted with yellow (β -tubulin) and gray (FtsZ) balls. Red arrow indicates the N/C-domain interface. Blue arrows and dashed line indicate the C/Core-domain interface. Colored circles represent hydrophobic core of each domain. The progressive assembly of the hydrophobic cores for N-, C- and Core domain of β -tubulin (bottom panels). **d** Model B factor distribution of each state highlights the N-domain with T3 loop in red dashed box (i) and corresponding cryo-EM density maps with fitted model are presented (ii). Per residue RMSD plots of T3 loop among four states (iii) and Q-score plot of T3 loop (iv). Dashed black line indicates average Q score expected at 3.5 Å resolution. **e** β -tubulin model with point mutations at the GTP binding pocket indicated as balls on residues that have folding defects. Their locations and effects are summarized¹⁵⁰.

3.4. Structural study of cochaperone and TRiC cooperation for substrate folding

3. 4. 1. Structural analysis of PhLP2A, substrate and TRiC

PhLP2A is known to cooperate with TRiC to fold specific substrates. Recent research demonstrated that the structure of TRiC, when endogenously purified from cell lysate, forms a ternary complex with actin and PhLP2A¹³³. In this study, we reconstituted the TRiC-actin-PhLP2A complex *in vitro* by incubating purified PhLP2A with TRiC and PFD-actin. After inducing the closed state by incubation with ATP/AIFx, cryo-EM analysis showed that most TRiC particles adopted a closed conformation, and approximately 42% of the particles displayed extra density within the TRiC chambers corresponding to either PhLP2A or actin (Figure 3.29, Figure 3.30a). Further 3D classification revealed that actin and PhLP2A were clearly encapsulated in opposite chambers (Figure 3.30b). Notably, actin inside the closed TRiC chamber appeared in a native-like folded state, indicating that unstructured actin had been transferred from PFD to TRiC and folded inside the chamber. This structure resembled the previously reported TRiC-actin-PhLP2A structure, which was a single snapshot of an undefined folding state captured from a cell lysate¹³³. These findings suggest that our *in vitro* reconstitution strategy using purified components successfully mimics the TRiC-mediated folding observed *in vivo* under physiological conditions. Collectively, these reconstructed structures provide insights into the role of PhLP2A in the TRiC-mediated actin folding cycle, leading to fully folded actin.

Next, we examined the residue interactions between PhLP2A in the cis-chamber and actin in the trans-chamber of the closed TRiC. Remarkably, both PhLP2A and actin interact with a negatively charged patch and engage with the positively charged patch on the CCT 3/6/8 chamber wall (Figure 3.30c, Figure 3.30d). This shared binding interface may provide the chemical logic for separating the

substrate and cochaperone into two distinct chambers. Actin in the TRiC chamber appeared to have reached a fully folded state, with its four subdomains (SD1–4) resolved (Figure 3.30b). SD1 and SD2 are anchored through polar interactions with the charged wall of CCT1/3/6, while SD3 and SD4 extend toward the chamber center without directly interacting with TRiC (Figure 3.30b). This structure aligns with previous hydrogen-deuterium exchange and mass spectrometry (HDX-MS) data, which indicated that SD1 and SD2 were protected by TRiC⁴⁹.

Interestingly, the ATP binding pocket of actin in TRiC is approximately 20 degrees more open than that of globular actin (PDB 4PKH, Figure 3.29e), likely due to domain-specific constraints imposed by TRiC subunits. The overall structure of PhLP2A in this complex is similar to that in the PhLP2A-TRiC closed complex, but the NTD H2 undergoes a dramatic conformational change, stretching across the inter-chamber cavity toward actin (Figure 3.30e). More importantly, the previously unresolved NTD H1 now makes direct contact with folded actin in the trans-chamber (Figure 3.30f, Figure 3.29c), suggesting that the presence of actin in the trans-chamber induces a ~60Å structural change in the PhLP2A NTD (Figure 3.30e). Next, we analyzed the binding mode between actin and PhLP2A. PhLP2A's H1 adopts an amphipathic helix that attaches to the hydrophobic groove between actin SD1 and SD3 (Figure 3.29h). Notably, this hydrophobic groove is a known interaction hotspot for actin polymerization regulators and a mutation hotspot affecting actin folding⁹⁰. These structural features suggest that TRiC and PhLP2A cooperate in orchestrating actin folding. The TRiC chamber wall serves as a rigid template to bring actin subdomains together, while PhLP2A's H1 makes specific contacts with actin, sealing the exposed hydrophobic surface between SD1 and SD3, assisting in the formation of the actin lobe, and facilitating folding.

3. 4. 2. Evolutionary analysis of PhLPs and TRiC for substrate folding

Each domain of PhLP2A plays a distinct yet synergistic role in its cooperation with TRiC upon ATP cycle. As PhLPs are known to evolve to have distinct homologs^{93,94}, I conducted an evolutionary analysis to understand the relationship among structures and activity and functional differences within the PhLP superfamily. I obtained the full sequences of 71 eukaryotic PhLPs and constructed a phylogenetic tree to reveal the evolutionary hierarchy among PhLP family members (Figure 3.31a). The analysis showed that the simple PhLP system in unicellular organisms, like PLP1 and PLP2 in yeast, diverged into various PhLP1-3 subfamilies and the phosducin (PDC) family in multicellular organisms. Notably, human PhLP3 is closest to yeast PLP1, and human PhLP2 is closest to yeast PLP2. PhLP1-3 branches appeared before the emergence of the phosducin family, which was historically the first to be identified. PhLP1, 2A, and 3 are ubiquitously expressed across various tissues^{98,151}, while PDC and PhLP2B are specifically expressed in the retina and reproductive tissues^{93,99,152}, respectively, indicating their later divergence for tissue-specific functions.

PhLPs share a similar domain architecture, but each domain is conserved to varying degrees (Figure 3.31b, Figure 3.32a). Domain elements that interact with both open and closed TRiC, such as H3 in the NTD and TXD, are highly conserved across PhLPs, particularly the positively charged patch on H3 and the hydrophobic surface of TXD, which interact with TRiC (Figure 3.31b). This specific conservation pattern suggests similar domain-wise interactions with TRiC for all PhLP family members as described for PhLP2A. PhLP1-3 all bind to TRiC to modulate substrate folding^{95,99,101}. Of note, PDC does not bind to TRiC despite having ~28% sequence identity with PhLP2A. Indeed, PDC shows significantly lower conservation in the TRiC-interacting residues^{95,136}.

Interestingly, the NTD and CTD regions are highly divergent across the PhLP family (Figure 3.31b, Figure 3.32a, Figure 3.32b, Figure 3.32c). The variable NTD includes the domain of PhLP2A that interacts with actin in the TRiC chamber. Such sequence variation may allow PhLPs to interact with multiple folding substrates within

the TRiC chamber. For instance, PhLP2B's NTD H1 also contains a -WNDIL- actin-binding motif, which is identified in PhLP2A in this study and in previous research¹³³. In contrast, this sequence is weakly conserved in other PhLPs. Instead, the NTD of PDC and PhLP1 contains a -GVI- G β -binding motif, which is absent in PhLP2A and PhLP2B, explaining why PDC and PhLP1 interact with G β ¹⁰². Thus, while PhLP isoforms conserve their TRiC-binding elements, the substrate-binding motifs have diverged, allowing them to facilitate a wider range of substrate folding processes within the TRiC chamber.

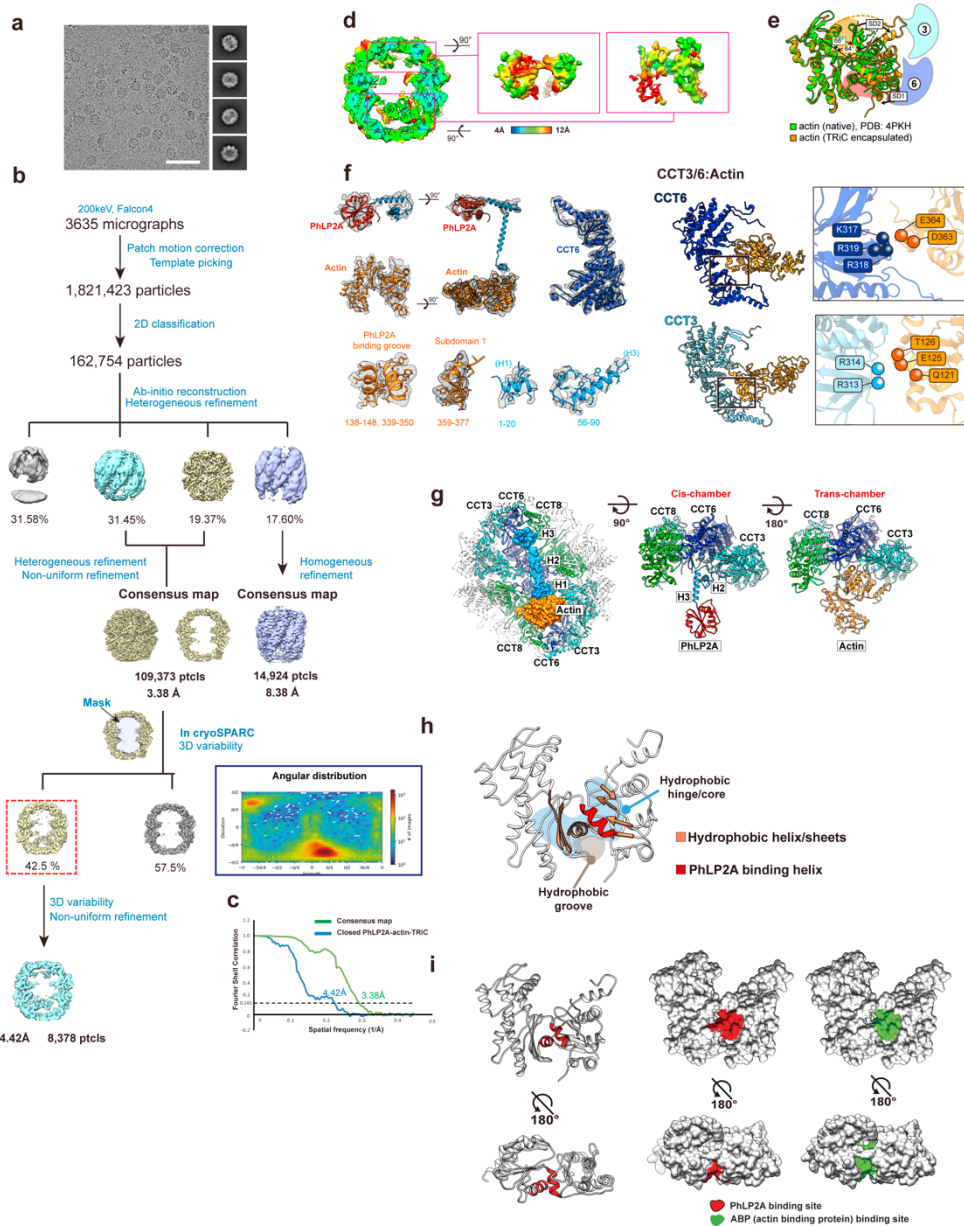


Figure 3.29 Cryo-EM structure of PhLP2A-actin encapsulated closed TRiC. **a** Representative cryo-EM micrograph and 2D class averages of PhLP2A-actin-TRiC in closed conformation. scale bar, 50 nm **b** Data processing workflow of PhLP2A-actin-TRiC in closed conformation. **c** A diagram of angular distribution for the particles is displayed. FSC curves of consensus map and reconstructed map of PhLP2A-actin-TRiC after focused classification. **d** Local resolution estimation of reconstructed map and zoom-in view on encapsulated

PhLP2A (left) or actin (right). **e** Comparison between models of native actin (PDB: 4PKH) and encapsulated actin. **f** Map-model fitting of the reconstructed map. Global fitting of PhLP2A, actin, and CCT6 are presented. Residues of actin interacting with CCT3 or CCT6 are also displayed. **g** The slice view of actin and PhLP2A surface in the TRiC chamber. PhLP2A and actin are shown from the outer chamber view with CCT3/6/8. **h** The interdomain of encapsulated actin. Hydrophobic sheets and helix are colored in orange while the PhLP2A binding helix is colored in red. The hydrophobic hinge/core and hydrophobic groove are represented. **i** The top and side view of PhLP2A binding site and ABP binding site representation on actin surface. Each surface is colored in red and green, respectively

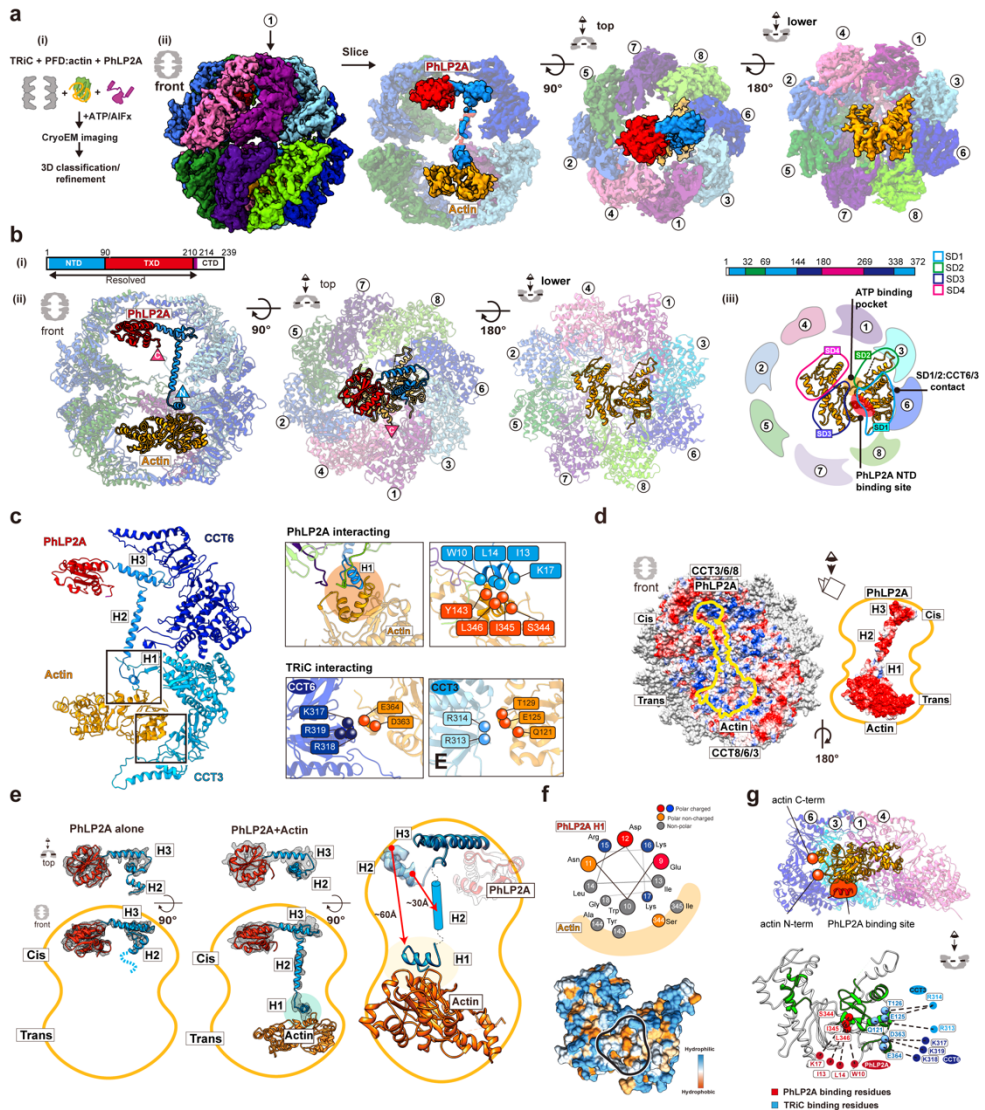


Figure 3.30 Cryo-EM structure of closed TRiC with folded actin and PhLP2A. **a** Cryo-EM structure of closed TRiC with folded actin and PhLP2A in each chamber. (i) Sample preparation scheme for the substrate-cochaperone TRiC. (ii) Cryo-EM map of folded actin and PhLP2A encapsulated in closed TRiC. The density of H2 of PhLP2A is low-pass filtered and depicted at $\sigma = 1.4$ from the density map of the full complex. CCT1 is indicated by an arrow. **b** Atomic model of closed PhLP2A-actin-TRiC (i) Schematic of the model of PhLP2A. (ii) Slice views of PhLP2A and folded actin encapsulated inside the closed TRiC. (iii) Summary of actin features inside the folding chamber. SD1 is the major binding site with the intermediate domain

of CCT3/6. The PhLP2A binding site is between SD1 and SD3 (indicated by a red circle), and the ATP binding pocket is on the opposite side, between SD2 and SD4 (indicated by an orange marker). **c** Detailed interactions between PhLP2A, CCT subunits, and folded actin. (Left) Interactions between the PhLP2A NTD or CCT3 and actin. (Right) (Top) H1 of PhLP2A and CCT3 show direct interaction with actin, forming a local hydrophobic interaction network. Interacting residues are represented as balls. (Bottom) Interacting residues between actin and CCT3/6 are shown as balls. **d** Electrostatic surface of the closed TRiC chambers (left), PhLP2A and actin (right). **e** The comparison between PhLP2A with and without actin in the closed folding chamber. Conformational changes of PhLP2A induced by the encapsulated substrate are represented. **f** The helix wheel plot and hydrophobic surface of encapsulated actin showing the actin-PhLP2A contact sites. **g** (Top) The slice view of the actin-TRiC contact site. CCT4/1/3/6 and actin are shown. N- and C-terminus of actin are represented as balls and PhLP2A binding site is colored in red. (Bottom) The folding defect mutant residues colored in green on the encapsulated actin structure. Red balls indicate the residues interacting with PhLP2A while blue balls represent CCT interacting residues.

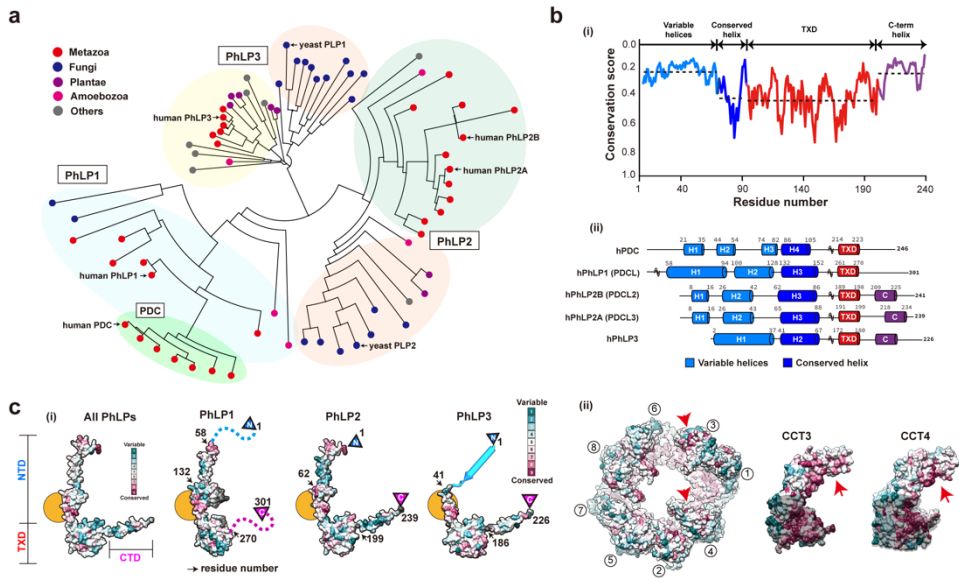


Figure 3.31 Conservation on Phosducin-like protein family and the proposed mechanism of chaperone-in-chaperonin mediated folding cycle. **a** Phylogenetic tree of the PhLP family. The kingdom of each branch and each human subtype (PhLP1, PhLP2A, PhLP2B, PhLP3, PDC) are indicated in the phylogenetic tree. **b** (i) The domain-wise conservation score of PhLPs. Each domain is divided according to human PhLP2A domain features. The dotted line indicates the average value of the conservation score for each domain. (ii) The secondary structures of 5 human PhLPs based on AlphaFold predictions. **c** Conservation scores of human PhLPs and TRiC. (i) Residue conservation of human PhLPs. The yellow circle indicates the conserved surface in H3 helix. (ii) Residue conservation among CCT subunits, and CCT3, CCT4 is shown.

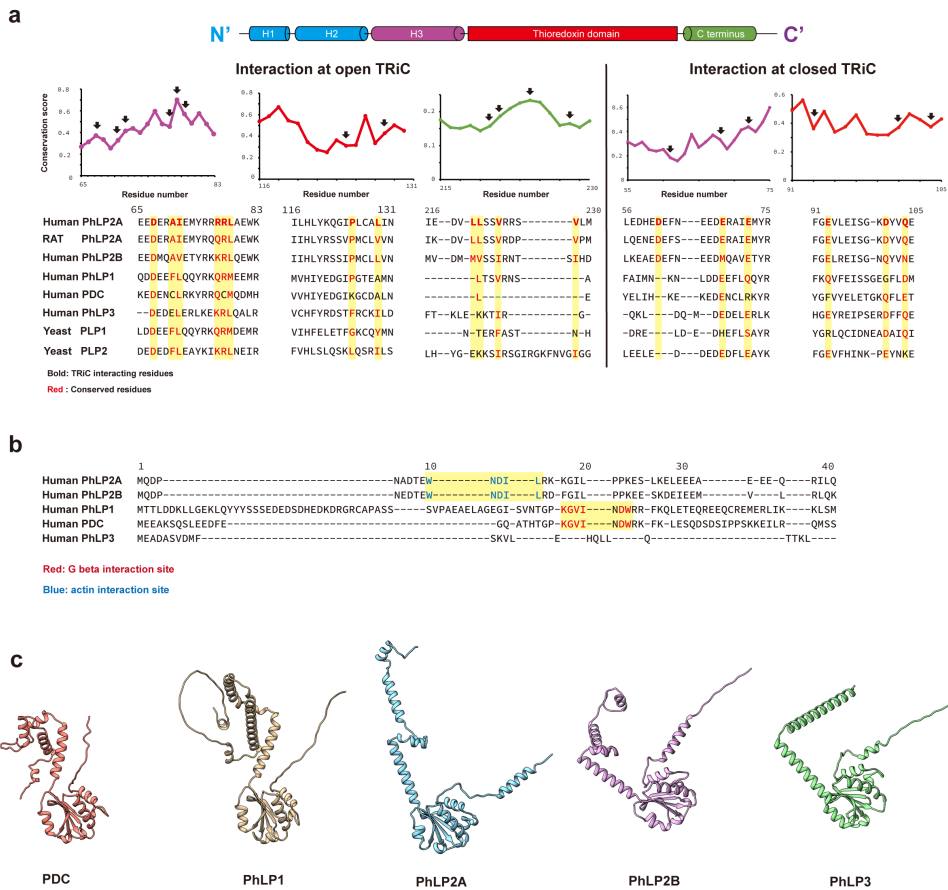


Figure. 3.32 Evolutionary analysis on phosducin-like protein family. **a** Representative sequence alignments for human PhLP families, rat PhLP2A and yeast PLPs. Plots on the left shows interacting residues in open TRiC state while plots on the right shows interacting regions in closed TRiC state. The average conservation scores of 71 phosducin (PDC) and PhLPs are plotted above. The interacting residues are indicated as black arrows in the plot. Human PhLP2A residues interacting with TRiC are colored in bold red and conserved residues in other phosducin and PhLPs are indicated as red. Left panel shows residues interacting within open TRiC while the right panel shows residues interacting within closed TRiC. **b** Sequence alignment among NTDs of 5 human phosducin families. Red indicates G β binding site and blue indicates actin binding site. **c** Model of AlphaFold-predicted 5 human phosducin and PhLPs from AlphaFold DB.

Chapter 4. Conclusion

4.1. Structural study of TRiC for substrate folding

4. 1. 1. The proposed mechanism of substrate delivery to TRiC

Various experiments suggested that substrate delivery to TRiC primarily occurs at the apical domain. However, the mechanism of substrate delivery by the cochaperone PFD has remained unclear. In this thesis, the process of substrate delivery by PFD-bound β -tubulin to apo TRiC was structurally visualized using an *in vitro* reconstitution of the delivery process and cryo-EM analysis.

The noble cryo-EM density maps show that β -tubulin bound PFD binds to open TRiC in a fully engaged conformation through electrostatic interactions. The binding of PFD to TRiC then promotes the substrate delivery. PFD-bound β -tubulin is delivered to the central cavity of open TRiC chamber, where interactions with the disordered CCT tails generates a compact entity without discernible folded elements. This suggests that the central cavity of open TRiC can function as a "third chamber," receiving and harboring the substrate during the folding process.

We speculate the disordered tails confined within the TRiC chamber act as a tethered solvent by nonspecific interactions. Tails may maintain the unstructured substrate as a dynamic yet compacted state such as a coacervate. The liquid-like nature of substrate may prevent the off-pathway reaction or trapped intermediates, priming the substrate for productive folding upon chamber closure (Figure 4.1).

4. 1. 2. The proposed mechanism of substrate folding without co-chaperones

As a chamber closes upon ATP-dependent cycle, the substrate

repositions from the equatorial chamber into one of two ring-enclosed folding chambers (Figure 4.1). The enclosed chamber directs the stepwise formation of β -tubulin folding intermediates that remain bound to specific regions in the chamber through electrostatic and H-bond interactions between β -tubulin and the TRiC chamber. These contacts establish the necessary native topology for β -tubulin and help orchestrate a hydrophobic collapse to then drive sequential folding of the β -tubulin domains. One feature of the discontinuous formation of β -tubulin domains in this folding pathway is the unidirectional assembly of the β -sheet spanning the entire hydrophobic core in folded β -tubulin. These TRiC contacts appear to direct β -tubulin folding through sequential domain formation without releasing the substrate into the chamber. This contrasts to the mechanism of chaperonin GroEL-ES, which releases polypeptides into an inner chamber that provides a unique confined environment for folding^{20,24,153-155}. The fact that contacts with the closed TRiC chamber guide multiple steps in β -tubulin folding raises doubts on the universality of Anfinsen's principle.

The concept of TRiC directing the folding pathway is illustrated by the notable structural change in the T3 loop of β -tubulin between states I and II. TRiC keeps the T3-loop in an extended conformation through contacts with the inner wall until the C-terminal domain folds through association with the TRiC wall, then the T3 loop is released from the chamber wall to become nestled at the N-C domain interface. The T3 loop acts as a folding switch to control sequential folding of the GTP binding pocket after completion of the N-C domain interface (Figure 4.1). Thus, TRiC binding to the T3 loop ensures the proper folding of the C domain, establishing the overall fold topology of β -tubulin and allowing the hydrophobic core of the M and core domains to fold. Perhaps GTP binding to the incipient nucleotide pocket drives these subsequent steps, as observed for bacterial tubulin FtsZ, where GTP binding is a limiting step during spontaneous refolding¹⁵⁶. The TRiC: β -tubulin contacts directly orchestrate the progression of events needed to form the GTP binding pocket by sequential positioning of the nucleotide sensing T3

loop to form the N-C domain interface, which are not conserved in FtsZ (Figure 3.27c). Consistent with this, tubulin mutations in the N-C domain interface affect β -tubulin folding and release from TRiC¹⁵⁰ (Figure 3.28e). While TRiC appears to direct the folding landscape through formation of specific intermediates (Figure 4.1), the tubulin-CCT contacts may also disfavor formation of kinetically trapped states (Figure 4.1).

4. 1. 3. The proposed mechanism of substrate folding with co-chaperones

TRiC functions in a cooperative network with PhLPs. Our analysis shows that PhLP2A can form a dynamic complex to both open and closed TRiC (Figure 4.2). In both conformations, PhLP2A binds inside the chamber but undergoes significant changes upon TRiC closure and in the presence of substrate (Figure 4.2). In the open state, the PhLP2A NTD adopts an H3 extended conformation to apical domains either CCT3 or 4. ATP-dependent TRiC closure encapsulates substrate and induces a large reorientation of PhLP2A domains, with reorienting the NTD H3 and shifting its binding sites inside the closed TRiC chamber. Within the chamber, PhLP2A becomes compacted with the highly negatively charged H2 and part of H3 associating with the positive hemisphere within the TRiC chamber. The presence of substrate in the opposite closed TRiC chamber induces a further conformational change of PhLP2A, specifically in H1 and H2 of the NTD, whereby H2 traverses the chamber positioning H1 to directly bind the substrate actin. H1 of PhLP2A masks a hydrophobic groove around two helices (aa 137–145 and 340–350) of encapsulated actin (Figure 3.30f). Our structure suggest PhLP2A H1 stabilizes an exposed hydrophobic core of actin intermediates that are folding within the TRiC chamber. While future experiments should delve into the mechanism of how PhLP2A assists folding, it is noteworthy that mutation in actin residues 340–344, *i.e.* corresponding to the PhLP2A H1 binding site, significantly affects actin folding^{90,91}. Furthermore, previous studies observed that the

folding of SD1 is rate-limiting for TRiC-mediated actin folding⁴⁹. Taken together, our study provides mechanistic insight into the molecular interplay between TRiC and PhLP2A to orchestrate a hydrophobic collapse that drives the folding of the substrate.

4.2. Cooperation of TRiC and co-chaperones for proteomic complexities

TRiC folds approximately 10% of the cytoplasmic proteome and employs distinct strategies to support the folding of various substrates³⁴. The hetero-oligomeric nature of TRiC is key to recognizing distinct motifs in multiple substrates and promoting their folding in the enclosed chamber^{49,50}. On the other hand, TRiC collaborates with several cochaperones, including PFD and PhLPs^{59,95,133,157}. Notably, the PhLP family consists of approximately 30 kDa cytosolic proteins that also participate in the regulation of TRiC-mediated protein folding^{94,151,158}. These PhLP homologs share a common domain structure featuring a central thioredoxin-like domain (TXD) flanked by variable-length, flexible N-terminal domain and C-terminal domain (NTD and CTD, respectively)¹⁵⁹. Each PhLP isoform exhibits unique activity and specificity toward different TRiC substrates. The isoforms share conserved TRiC binding components while evolving distinct substrate-binding elements that dictate their roles in the TRiC folding environment¹⁵⁹. PhLPs are exclusive to eukaryotes, and their emergence may correlate with the rise in proteomic complexity. The combined use of PhLPs as substrate-specific cochaperones amplifies the capacity of TRiC to fold various substrates. Indeed, recent studies have revealed the domain-specific connections between PhLP2A and TRiC, and various functions of the cochaperone in the TRiC network^{133,157,159}.

4.3. Structural comparison of TRiC mediated folding pathway among different substrates

Many studies have attempted to determine the whereabouts of the

substrate in the subsequent phase of the chamber closure of TRiC, triggered by ATP hydrolysis using biophysics or biochemistry^{49,81,91,160}. However, structural visualization of the substrate in the chamber has remained elusive due to its innate heterogeneity and complexity. In the light of the cryo-EM method and the power of heterogeneity analysis, multiple studies have recently succeeded in capturing snapshots of the folded or partially folded substrate in the TRiC folding chamber in the presence of ATP-Aluminium fluoride (AlFx)^{42,67,133,157,159}.

Among TRiC's substrates, $\sigma 3$, tubulin, and actin in the closed TRiC are visualized by using cryo-EM, either in the yeast system or human system (Figure 4.3). The first resolved structure is one of the reovirus outer capsid proteins, $\sigma 3$ ⁴². The substrate shows a near-native conformation and is oriented inside the chamber, stretching across the asymmetrically charged hemisphere with charge complementarity, whose positively charged surface interacts with a negatively charged inner wall of the TRiC chamber, and vice versa. Similarly, tubulin possesses a native conformation in both yeast and human TRiC and has strong interactions with the positively charged patches of TRiC, while no interaction is observed with the negatively charged half-hemisphere of a folding chamber^{67,105,133,157}. Meanwhile, actin exhibits electrostatic interactions with both hemispheres. Interestingly, actin has a different conformation compared to G-actin, which shows a “much opened” conformation, with a wider angle between the 2 domains of actin¹³³. This suggests that TRiC can alter the structure of the substrate inside its chamber during or after folding, either in direct or indirect ways. Interestingly, $\sigma 3$, tubulin, and actin all have strong surface charges complementary to the inner wall of the closed TRiC hemisphere. This suggests that TRiC strongly holds the substrate through electrostatic interaction and that the charge division acts differently depending on the substrate features. In addition, recent studies also report the interaction between the tails of CCT subunits and substrates, suggesting additional ways of interaction adopted by the TRiC complex^{67,105}.

4.4. Future direction

TRiC exhibits an impressive substrate folding repertoire by interacting with approximately 10% of the entire eukaryotic proteome. This diversity is largely attributed to the divergence of eight distinct subunits and the additional substrate specificity provided by cochaperones. In this thesis, I have elucidated the specific interactions between TRiC and a subset of substrates, particularly focusing on the interaction between TRiC and tubulin, revealing the tubulin-specific folding pathway.

However, the substrate clients of TRiC remain highly diverse, and the structures of these substrates vary widely. Consequently, how TRiC guides the folding of each specific substrate remain elusive. Additionally, some substrates are larger than the chamber size of TRiC, and a mechanism has been proposed where only certain domains of the substrate fold within the chamber. However, the detailed process behind this process remains to be thoroughly explored. Therefore, further research is required to fully understand the individual substrate folding pathways that TRiC facilitates for a wide range of proteins.

This thesis revealed that PhLP2A dynamically interacts with TRiC throughout the ATPase cycle, modulating both the interactions with other cochaperones and guiding the substrate folding pathway. However, for other PhLP family members, such as PhLP1 and PhLP3, the mechanisms upon ATPase cycle remains elusive. Moreover, investigating the interactions between other PhLP family subtypes and TRiC will be crucial for gaining a comprehensive understanding of how these cochaperones participate in protein folding processes across different substrates.

Furthermore, it remains unclear if and how PhLP2A is involved in the folding of other substrates beyond those identified so far. Future research will need to explore these questions through biochemical techniques, mass spectrometry, and additional experimental approaches to identify other substrates of PhLP2A and to clarify the relationships between PhLP2A and different substrates.

Lastly, this folding analysis was conducted using an *in vitro* reconstitution approach. However, within actual cells, various events occur simultaneously and influence one another. Notably, TRiC has been directly associated with several diseases. Therefore, further research is essential to investigate the TRiC-mediated folding pathway occurring in living cells. This includes how function of TRiC varies between cell types and the specific role TRiC plays in disease contexts. Understanding TRiC's behavior in physiological conditions will be key to revealing its broader impact on cellular proteostasis and its contribution to disease mechanisms.

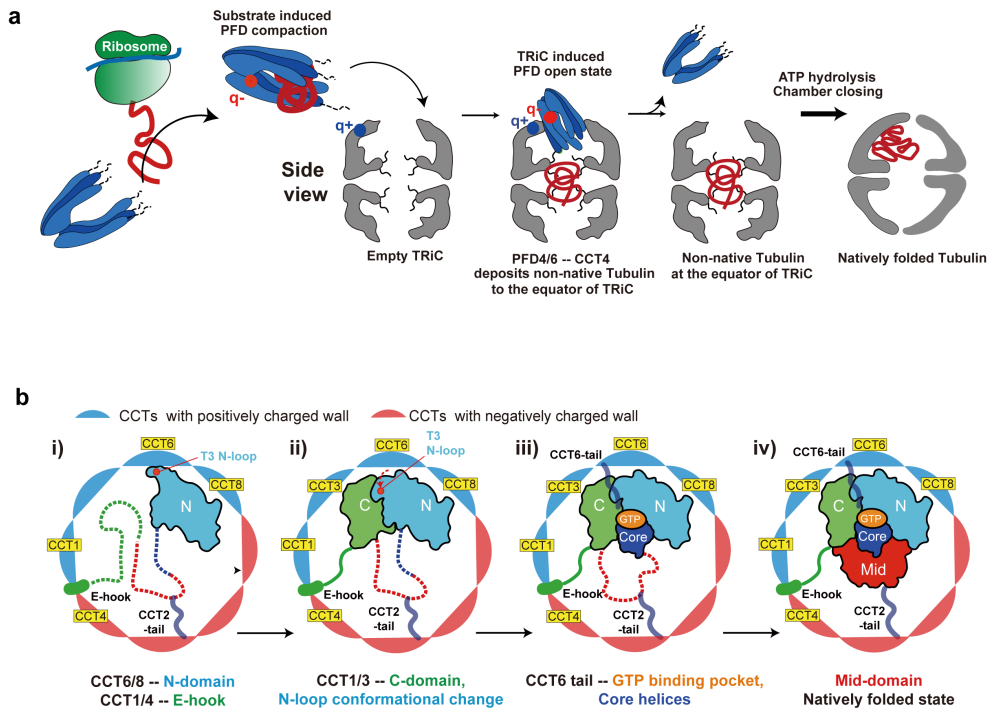


Figure. 4.1 Mechanism of TRiC mediated substrate folding pathway.
 a Substrate delivery mediated by PFD b Substrate folding pathway in the folding chamber without cochaperone

a

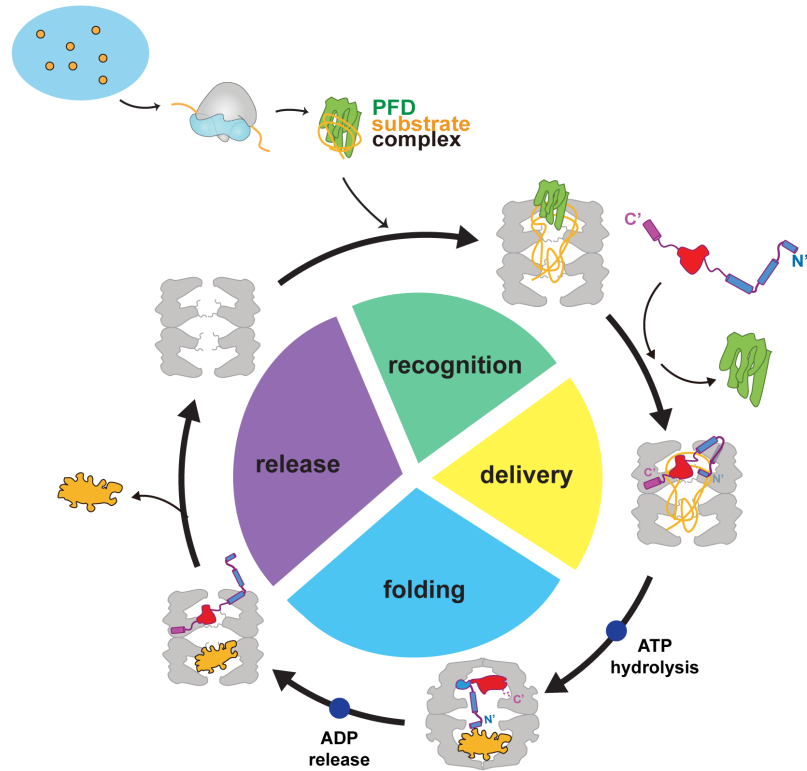


Figure 4.2 Mechanism of TRiC and cochaperone PhLP2A mediated substrate folding pathway. a Substrate folding cycle mediated by TRiC and cochaperone PhLP2A.

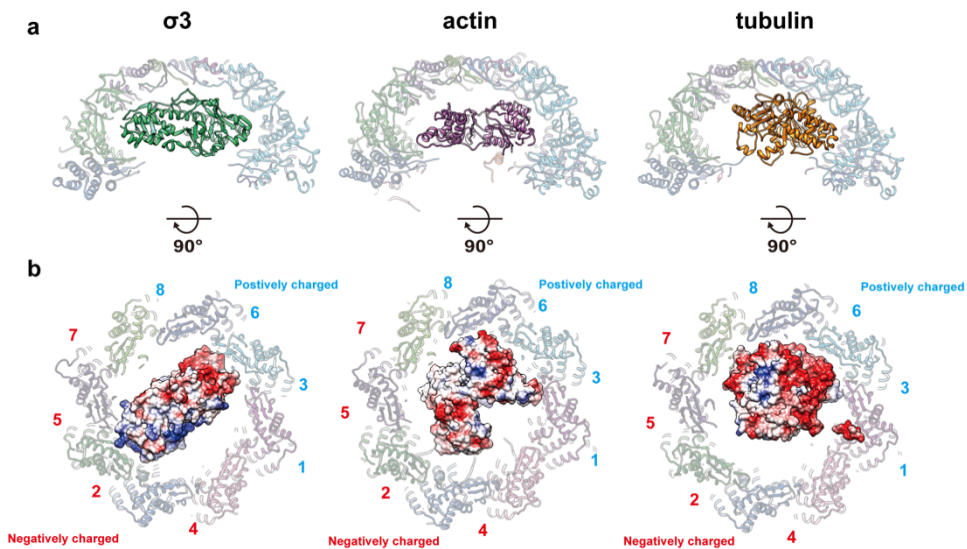


Figure. 4.3 Substrate-specific interaction in the TRiC folding chamber. **a** Three structures of substrates encapsulated in closed TRiC ($\sigma 3$, tubulin, actin, PDB: 7LUP, 7TUB, 7NVM, respectively) shown in cartoon models at side slice view, and **b** electrostatic charge surface of substrates encapsulated at top slice view. Each substrate shows specific interactions with different CCT subunits.

	Apo-TRiC	PFD- β Tub-TRiC	TRiC- β Tub State I	TRiC- β Tub State II	TRiC- β Tub State III	TRiC- β Tub State IV
CryoEM image collection and map processing						
Voltage (kV)	300	300	300	300	300	300
Total electron exposure ($e^-/\text{\AA}^2$)	37	36	37	37	37	37
Defocus range (μm)	-0.5~-2.5	-0.5~-3.5	-0.5~-3.5	-0.5~-3.5	-0.5~-3.5	-0.5~-3.5
Pixel size (\AA)	1.0	1.02	1.1	1.1	1.1	1.1
Symmetry imposed	C1	C1	C1	C1	C1	C1
Particle images (no.)	662,744	194,013	110,984	42,804	94,955	24,233
Map resolution (\AA) FSC threshold (0.143)	3.1	3.9	3.0	3.3	2.9	3.6
EMDB ID	32822	32823	26089	26120	26123	26131
Model refinement						
Initial model used (PDB code)	N/A	6NR8	7LUM, 6I2I	7LUM, 6I2I	7LUM, 6I2I	7LUM, 6I2I
Model composition Non-hydrogen atoms Protein residues Ligands		67039 8727 ADP:4	33714 4377 MG: 8 ADP: 8 AF ₃ : 8 H ₂ O: 8	34563 4481 MG: 8 ADP: 8 AF ₃ : 8 H ₂ O: 8	35180 4561 MG: 8 ADP: 8 AF ₃ : 8 H ₂ O: 8	35877 4650 MG: 8 ADP: 8 AF ₃ : 8 H ₂ O: 8
R.m.s. deviations Bond lengths (\AA) Bond angles ($^\circ$)		0.003 0.790	0.014 1.137	0.012 1.233	0.010 1.049	0.006 0.767
Validation MolProbity score Clashscore Rotamer outliers (%)		2.12 18.09 0.08	1.6 4.7 0.08	1.61 4.54 0.32	1.57 4.52 0.00	1.65 6.22 0.13
Ramachandran plot Favored (%) Allowed (%) Outliers (%)		94.66 5.25 0.09	94.83 5.03 0.14	94.39 5.45 0.16	95.02 4.78 0.20	95.62 4.30 0.09
PDB ID		7WU7	7TRG	7TTN	7TTT	7TUB

Table 1. Cryo-EM image collection, map reconstruction, and model refinement. List of cryo-EM image collection information and map reconstruction, and model refinement statistics.

CryoEM image collection and map processing						
	TRiC-PhLP2A	TRiC-PhLP2A (CCT3 focused)	TRiC-PhLP2A (CCT4 focused)	TRiC-PhLP2A-ATP/AIFx	TRiC-PhLP2A-actin-ATP/AIFx	TRiC-PFD TRiC
Voltage (kV)	300			200	200	200
Total electron exposure (e⁻/Å²)	50			40	40	40
Defocus range (μm)	-1.0~-1.8			-1.2~-1.8	-1.2~-1.8	-1.2~-1.8
Pixel size (Å)	1.13			1.1	1.1	1.1
Symmetry imposed	C1			C1	C1	C1
Particle images (no.)	1,796,900	359,533	485,964	21,028	8,378	50,832
Map resolution (Å) FSC threshold (0.143)	3.1	3.82	4.22	3.24	4.42	4.19
EMDB ID	35284	35199	35280	35122	35335	35284 (An additional map)

Model refinement					
	TRiC-PhLP2A	TRiC-PhLP2A (CCT3 focused)	TRiC-PhLP2A (CCT4 focused)	TRiC-PhLP2A-ATP/AIFx	TRiC-PhLP2A-actin-ATP/AIFx
Initial model used (PDB code)	6NR8	6NR8	6NR8	7NVM, 7TUB	7LUM 7NVM
Model composition Non-hydrogen atoms Protein residues Ligands	65,141 8,483 ADP:10	5,287 670 ADP:1	5,177 675	67,629 8,763 MG: 16 ADP: 16 AF ₃ : 16	68,540 8,948
R.m.s. deviations Bond lengths (Å) Bond angles (°)	0.003 0.872	0.003 0.697	0.005 0.828	0.003 0.627	0.003 0.710
Validation MolProbity score Clashscore Rotamer outliers (%)	2.01 4.20 1.78	1.95 7.55 0.17	2.36 18.09 0.17	1.96 11.10 0.00	2.29 23.74 0.01
Ramachandran plot Favored (%) Allowed (%) Outliers (%)	87.16 12.10 0.75	90.39 9.61 0.00	87.78 12.07 0.17	94.13 5.83 0.03	93.64 6.36 0.00
PDB ID	8I9U	8I6J	8I9Q	8I1U	8IB8

Table 2. Cryo-EM image collection, map reconstruction, and model refinement. List of cryo-EM image collection information and map reconstruction, and model refinement statistics.

Bibliography

1. Kim, M.S., Pinto, S.M., Getnet, D., Nirujogi, R.S., Manda, S.S., Chaerkady, R., Madugundu, A.K., Kelkar, D.S., Isserlin, R., Jain, S., et al. (2014). A draft map of the human proteome. *Nature* *509*, 575–581. 10.1038/nature13302.
2. Wilhelm, M., Schlegl, J., Hahne, H., Gholami, A.M., Lieberenz, M., Savitski, M.M., Ziegler, E., Butzmann, L., Gessulat, S., Marx, H., et al. (2014). Mass-spectrometry-based draft of the human proteome. *Nature* *509*, 582–587. 10.1038/nature13319.
3. Beck, M., Schmidt, A., Malmstroem, J., Claassen, M., Ori, A., Szymborska, A., Herzog, F., Rinner, O., Ellenberg, J., and Aebersold, R. (2011). The quantitative proteome of a human cell line. *Mol Syst Biol* *7*, 549. 10.1038/msb.2011.82.
4. Boudiaf-Benmammar, C., Cresteil, T., and Melki, R. (2013). The cytosolic chaperonin CCT/TRiC and cancer cell proliferation. *PLoS One* *8*, e60895. 10.1371/journal.pone.0060895.
5. Emsley, P., Lohkamp, B., Scott, W.G., and Cowtan, K. (2010). Features and development of Coot. *Acta Crystallogr D Biol Crystallogr* *66*, 486–501. 10.1107/S0907444910007493.
6. Sweeney, P., Park, H., Baumann, M., Dunlop, J., Frydman, J., Kopito, R., McCampbell, A., Leblanc, G., Venkateswaran, A., Nurmi, A., and Hodgson, R. (2017). Protein misfolding in neurodegenerative diseases: implications and strategies. *Transl Neurodegener* *6*, 6. 10.1186/s40035-017-0077-5.
7. Todd, T.W., and Lim, J. (2013). Aggregation formation in the polyglutamine diseases: protection at a cost? *Mol Cells* *36*, 185–194. 10.1007/s10059-013-0167-x.
8. Levinthal, C. (1968). Are there pathways for protein folding? *Journal de chimie physique* *65*, 44–45.
9. Anfinsen, C.B. (1973). Principles that govern the folding of protein chains. *Science* *181*, 223–230. 10.1126/science.181.4096.223.
10. Dill, K.A. (1985). Theory for the folding and stability of globular proteins. *Biochemistry* *24*, 1501–1509. 10.1021/bi00327a032.
11. Bryngelson, J.D., and Wolynes, P.G. (1987). Spin glasses and the statistical mechanics of protein folding. *Proc Natl Acad Sci U S A* *84*, 7524–7528. 10.1073/pnas.84.21.7524.
12. Brockwell, D.J., and Radford, S.E. (2007). Intermediates: ubiquitous species on folding energy landscapes? *Curr Opin Struct Biol* *17*, 30–37. 10.1016/j.sbi.2007.01.003.
13. Hartl, F.U. (1996). Molecular chaperones in cellular protein folding. *Nature* *381*, 571–579. 10.1038/381571a0.
14. Genest, O., Wickner, S., and Doyle, S.M. (2019). Hsp90 and Hsp70 chaperones: Collaborators in protein remodeling. *J Biol Chem* *294*,

- 2109–2120. 10.1074/jbc.REV118.002806.
15. Kim, Y.E., Hipp, M.S., Bracher, A., Hayer-Hartl, M., and Hartl, F.U. (2013). Molecular chaperone functions in protein folding and proteostasis. *Annu Rev Biochem* *82*, 323–355. 10.1146/annurev-biochem-060208-092442.
 16. Mayer, M.P. (2013). Hsp70 chaperone dynamics and molecular mechanism. *Trends Biochem Sci* *38*, 507–514. 10.1016/j.tibs.2013.08.001.
 17. Hayer-Hartl, M., Bracher, A., and Hartl, F.U. (2016). The GroEL–GroES Chaperonin Machine: A Nano-Cage for Protein Folding. *Trends Biochem Sci* *41*, 62–76. 10.1016/j.tibs.2015.07.009.
 18. Lopez, T., Dalton, K., and Frydman, J. (2015). The Mechanism and Function of Group II Chaperonins. *J Mol Biol* *427*, 2919–2930. 10.1016/j.jmb.2015.04.013.
 19. Saibil, H.R., Fenton, W.A., Clare, D.K., and Horwich, A.L. (2013). Structure and allostery of the chaperonin GroEL. *J Mol Biol* *425*, 1476–1487. 10.1016/j.jmb.2012.11.028.
 20. Gupta, A.J., Haldar, S., Milicic, G., Hartl, F.U., and Hayer-Hartl, M. (2014). Active cage mechanism of chaperonin-assisted protein folding demonstrated at single-molecule level. *J Mol Biol* *426*, 2739–2754. 10.1016/j.jmb.2014.04.018.
 21. Clare, D.K., Vasishtan, D., Stagg, S., Quispe, J., Farr, G.W., Topf, M., Horwich, A.L., and Saibil, H.R. (2012). ATP-triggered conformational changes delineate substrate-binding and -folding mechanics of the GroEL chaperonin. *Cell* *149*, 113–123. 10.1016/j.cell.2012.02.047.
 22. Gruber, R., and Horovitz, A. (2016). Allosteric Mechanisms in Chaperonin Machines. *Chem Rev* *116*, 6588–6606. 10.1021/acs.chemrev.5b00556.
 23. Lin, Z., Madan, D., and Rye, H.S. (2008). GroEL stimulates protein folding through forced unfolding. *Nat Struct Mol Biol* *15*, 303–311. 10.1038/nsmb.1394.
 24. Sharma, S., Chakraborty, K., Muller, B.K., Astola, N., Tang, Y.C., Lamb, D.C., Hayer-Hartl, M., and Hartl, F.U. (2008). Monitoring protein conformation along the pathway of chaperonin-assisted folding. *Cell* *133*, 142–153. 10.1016/j.cell.2008.01.048.
 25. Tang, Y.C., Chang, H.C., Roeben, A., Wischnewski, D., Wischnewski, N., Kerner, M.J., Hartl, F.U., and Hayer-Hartl, M. (2006). Structural features of the GroEL–GroES nano-cage required for rapid folding of encapsulated protein. *Cell* *125*, 903–914. 10.1016/j.cell.2006.04.027.
 26. Bai, C., Guo, P., Zhao, Q., Lv, Z., Zhang, S., Gao, F., Gao, L., Wang, Y., Tian, Z., Wang, J., et al. (2015). Protomer Roles in Chloroplast Chaperonin Assembly and Function. *Mol Plant* *8*, 1478–1492. 10.1016/j.molp.2015.06.002.
 27. Cong, Y., Baker, M.L., Jakana, J., Woolford, D., Miller, E.J., Reissmann, S., Kumar, R.N., Redding-Johanson, A.M., Batth, T.S., Mukhopadhyay, A., et al. (2010). 4.0-Å resolution cryo-EM structure of the mammalian chaperonin TRiC/CCT reveals its unique

- subunit arrangement. *Proc Natl Acad Sci U S A* *107*, 4967–4972. 10.1073/pnas.0913774107.
28. Frydman, J., Nimmesgern, E., Erdjument–Bromage, H., Wall, J.S., Tempst, P., and Hartl, F.U. (1992). Function in protein folding of TRiC, a cytosolic ring complex containing TCP–1 and structurally related subunits. *EMBO J* *11*, 4767–4778. 10.1002/j.1460–2075.1992.tb05582.x.
 29. Kim, S.K., Kim, S.R., Kim, Y.H., Kwack, P., Son, D., and Cheong, G.W. (2002). Structural analysis of thermosome from hyperthermophilic archaeon *Thermococcus*. *Mol Cells* *14*, 85–92.
 30. Leitner, A., Joachimiak, L.A., Bracher, A., Monkemeyer, L., Walzthoeni, T., Chen, B., Pechmann, S., Holmes, S., Cong, Y., Ma, B., et al. (2012). The molecular architecture of the eukaryotic chaperonin TRiC/CCT. *Structure* *20*, 814–825. 10.1016/j.str.2012.03.007.
 31. Gestaut, D., Limatola, A., Joachimiak, L., and Frydman, J. (2019). The ATP–powered gymnastics of TRiC/CCT: an asymmetric protein folding machine with a symmetric origin story. *Curr Opin Struct Biol* *55*, 50–58. 10.1016/j.sbi.2019.03.002.
 32. Zhang, J., Baker, M.L., Schroder, G.F., Douglas, N.R., Reissmann, S., Jakana, J., Dougherty, M., Fu, C.J., Levitt, M., Ludtke, S.J., et al. (2010). Mechanism of folding chamber closure in a group II chaperonin. *Nature* *463*, 379–383. 10.1038/nature08701.
 33. Hein, M.Y., Hubner, N.C., Poser, I., Cox, J., Nagaraj, N., Toyoda, Y., Gak, I.A., Weisswange, I., Mansfeld, J., Buchholz, F., et al. (2015). A human interactome in three quantitative dimensions organized by stoichiometries and abundances. *Cell* *163*, 712–723. 10.1016/j.cell.2015.09.053.
 34. Yam, A.Y., Xia, Y., Lin, H.T., Burlingame, A., Gerstein, M., and Frydman, J. (2008). Defining the TRiC/CCT interactome links chaperonin function to stabilization of newly made proteins with complex topologies. *Nat Struct Mol Biol* *15*, 1255–1262. 10.1038/nsmb.1515.
 35. Shen, K., and Frydman, J. (2012). The Interplay Between the Chaperonin TRiC and N–terminal Region of Huntingtin Mediates Huntington's Disease Aggregation and Pathogenesis. In *Protein Quality Control in Neurodegenerative Disease*, R.I. Morimoto, and Y. Christen, eds. (Springer Verlag).
 36. Sontag, E.M., Joachimiak, L.A., Tan, Z., Tomlinson, A., Housman, D.E., Glabe, C.G., Potkin, S.G., Frydman, J., and Thompson, L.M. (2013). Exogenous delivery of chaperonin subunit fragment ApiCCT1 modulates mutant Huntingtin cellular phenotypes. *Proc Natl Acad Sci U S A* *110*, 3077–3082. 10.1073/pnas.1222663110.
 37. Shahmoradian, S.H., Galaz–Montoya, J.G., Schmid, M.F., Cong, Y., Ma, B., Spiess, C., Frydman, J., Ludtke, S.J., and Chiu, W. (2013). TRiC's tricks inhibit huntingtin aggregation. *Elife* *2*, e00710. 10.7554/eLife.00710.
 38. Guo, Q., Lehmer, C., Martinez–Sanchez, A., Rudack, T., Beck, F.,

- Hartmann, H., Perez-Berlanga, M., Frottin, F., Hipp, M.S., Hartl, F.U., et al. (2018). In Situ Structure of Neuronal C9orf72 Poly-GA Aggregates Reveals Proteasome Recruitment. *Cell* *172*, 696-705 e612. 10.1016/j.cell.2017.12.030.
39. Chen, X.Q., Fang, F., Florio, J.B., Rockenstein, E., Masliah, E., Mobley, W.C., Rissman, R.A., and Wu, C. (2018). T-complex protein 1-ring complex enhances retrograde axonal transport by modulating tau phosphorylation. *Traffic* *19*, 840-853.
 40. Sot, B., Rubio-Munoz, A., Leal-Quintero, A., Martinez-Sabando, J., Marcilla, M., Roodveldt, C., and Valpuesta, J.M. (2017). The chaperonin CCT inhibits assembly of alpha-synuclein amyloid fibrils by a specific, conformation-dependent interaction. *Sci Rep* *7*, 40859. 10.1038/srep40859.
 41. Hong, S., Choi, G., Park, S., Chung, A.S., Hunter, E., and Rhee, S.S. (2001). Type D retrovirus Gag polyprotein interacts with the cytosolic chaperonin TRiC. *J Virol* *75*, 2526-2534. 10.1128/JVI.75.6.2526-2534.2001.
 42. Knowlton, J.J., Fernandez de Castro, I., Ashbrook, A.W., Gestaut, D.R., Zamora, P.F., Bauer, J.A., Forrest, J.C., Frydman, J., Risco, C., and Dermody, T.S. (2018). The TRiC chaperonin controls reovirus replication through outer-capsid folding. *Nat Microbiol* *3*, 481-493. 10.1038/s41564-018-0122-x.
 43. Zhou, H., Xu, M., Huang, Q., Gates, A.T., Zhang, X.D., Castle, J.C., Stec, E., Ferrer, M., Strulovici, B., Hazuda, D.J., and Espeseth, A.S. (2008). Genome-scale RNAi screen for host factors required for HIV replication. *Cell Host Microbe* *4*, 495-504. 10.1016/j.chom.2008.10.004.
 44. Spiess, C., Miller, E.J., McClellan, A.J., and Frydman, J. (2006). Identification of the TRiC/CCT substrate binding sites uncovers the function of subunit diversity in eukaryotic chaperonins. *Mol Cell* *24*, 25-37. 10.1016/j.molcel.2006.09.003.
 45. Trinidad, A.G., Muller, P.A., Cuellar, J., Klejnot, M., Nobis, M., Valpuesta, J.M., and Vousden, K.H. (2013). Interaction of p53 with the CCT complex promotes protein folding and wild-type p53 activity. *Mol Cell* *50*, 805-817. 10.1016/j.molcel.2013.05.002.
 46. Kasembeli, M., Lau, W.C., Roh, S.H., Eckols, T.K., Frydman, J., Chiu, W., and Tweardy, D.J. (2014). Modulation of STAT3 folding and function by TRiC/CCT chaperonin. *PLoS Biol* *12*, e1001844. 10.1371/journal.pbio.1001844.
 47. Wang, D.Y., Kamuda, K., Montoya, G., and Mesa, P. (2020). The TRiC/CCT Chaperonin and Its Role in Uncontrolled Proliferation. *Adv Exp Med Biol* *1243*, 21-40. 10.1007/978-3-030-40204-4_2.
 48. Lin, P., and Sherman, F. (1997). The unique hetero-oligomeric nature of the subunits in the catalytic cooperativity of the yeast Cct chaperonin complex. *Proc Natl Acad Sci U S A* *94*, 10780-10785.
 49. Balchin, D., Milicic, G., Strauss, M., Hayer-Hartl, M., and Hartl, F.U. (2018). Pathway of Actin Folding Directed by the Eukaryotic Chaperonin TRiC. *Cell* *174*, 1507-1521 e1516.

- 10.1016/j.cell.2018.07.006.
50. Joachimiak, L.A., Walzthoeni, T., Liu, C.W., Aebersold, R., and Frydman, J. (2014). The structural basis of substrate recognition by the eukaryotic chaperonin TRiC/CCT. *Cell* *159*, 1042–1055. 10.1016/j.cell.2014.10.042.
 51. Llorca, O., Smyth, M.G., Marco, S., Carrascosa, J.L., Willison, K.R., and Valpuesta, J.M. (1998). ATP binding induces large conformational changes in the apical and equatorial domains of the eukaryotic chaperonin containing TCP-1 complex. *J Biol Chem* *273*, 10091–10094. 10.1074/jbc.273.17.10091.
 52. Ditzel, L., Lowe, J., Stock, D., Stetter, K.O., Huber, H., Huber, R., and Steinbacher, S. (1998). Crystal structure of the thermosome, the archaeal chaperonin and homolog of CCT. *Cell* *93*, 125–138.
 53. Shomura, Y., Yoshida, T., Iizuka, R., Maruyama, T., Yohda, M., and Miki, K. (2004). Crystal structures of the group II chaperonin from *Thermococcus* strain KS-1: steric hindrance by the substituted amino acid, and inter-subunit rearrangement between two crystal forms. *J Mol Biol* *335*, 1265–1278.
 54. Dekker, C., Roe, S.M., McCormack, E.A., Beuron, F., Pearl, L.H., and Willison, K.R. (2011). The crystal structure of yeast CCT reveals intrinsic asymmetry of eukaryotic cytosolic chaperonins. *EMBO J* *30*, 3078–3090. 10.1038/emboj.2011.208.
 55. Munoz, I.G., Yebenes, H., Zhou, M., Mesa, P., Serna, M., Park, A.Y., Bragado-Nilsson, E., Beloso, A., de Carcer, G., Malumbres, M., et al. (2011). Crystal structure of the open conformation of the mammalian chaperonin CCT in complex with tubulin. *Nat Struct Mol Biol* *18*, 14–19. 10.1038/nsmb.1971.
 56. Martin-Benito, J., Grantham, J., Boskovic, J., Brackley, K.I., Carrascosa, J.L., Willison, K.R., and Valpuesta, J.M. (2007). The inter-ring arrangement of the cytosolic chaperonin CCT. *EMBO Rep* *8*, 252–257. 10.1038/sj.embor.7400894.
 57. Kalisman, N., Adams, C.M., and Levitt, M. (2012). Subunit order of eukaryotic TRiC/CCT chaperonin by cross-linking, mass spectrometry, and combinatorial homology modeling. *Proc Natl Acad Sci U S A* *109*, 2884–2889. 10.1073/pnas.1119472109.
 58. Zang, Y., Jin, M., Wang, H., Cui, Z., Kong, L., Liu, C., and Cong, Y. (2016). Staggered ATP binding mechanism of eukaryotic chaperonin TRiC (CCT) revealed through high-resolution cryo-EM. *Nat Struct Mol Biol* *23*, 1083–1091. 10.1038/nsmb.3309.
 59. Gestaut, D., Roh, S.H., Ma, B., Pintilie, G., Joachimiak, L.A., Leitner, A., Walzthoeni, T., Aebersold, R., Chiu, W., and Frydman, J. (2019). The Chaperonin TRiC/CCT Associates with Prefoldin through a Conserved Electrostatic Interface Essential for Cellular Proteostasis. *Cell* *177*, 751–765 e715. 10.1016/j.cell.2019.03.012.
 60. Meyer, A.S., Gillespie, J.R., Walther, D., Millet, I.S., Doniach, S., and Frydman, J. (2003). Closing the folding chamber of the eukaryotic chaperonin requires the transition state of ATP hydrolysis. *Cell* *113*, 369–381. 10.1016/s0092-8674(03)00307-6.

61. Jin, M., Han, W., Liu, C., Zang, Y., Li, J., Wang, F., Wang, Y., and Cong, Y. (2019). An ensemble of cryo-EM structures of TRiC reveal its conformational landscape and subunit specificity. *Proc Natl Acad Sci U S A* *116*, 19513–19522. 10.1073/pnas.1903976116.
62. Jiang, Y., Douglas, N.R., Conley, N.R., Miller, E.J., Frydman, J., and Moerner, W.E. (2011). Sensing cooperativity in ATP hydrolysis for single multisubunit enzymes in solution. *Proc Natl Acad Sci U S A* *108*, 16962–16967. 10.1073/pnas.1112244108.
63. Reissmann, S., Joachimiak, L.A., Chen, B., Meyer, A.S., Nguyen, A., and Frydman, J. (2012). A gradient of ATP affinities generates an asymmetric power stroke driving the chaperonin TRiC/CCT folding cycle. *Cell Rep* *2*, 866–877. 10.1016/j.celrep.2012.08.036.
64. Vainberg, I.E., Lewis, S.A., Rommelaere, H., Ampe, C., Vandekerckhove, J., Klein, H.L., and Cowan, N.J. (1998). Prefoldin, a chaperone that delivers unfolded proteins to cytosolic chaperonin. *Cell* *93*, 863–873.
65. Leroux, M.R., Fandrich, M., Klunker, D., Siegers, K., Lupas, A.N., Brown, J.R., Schiebel, E., Dobson, C.M., and Hartl, F.U. (1999). MtGimC, a novel archaeal chaperone related to the eukaryotic chaperonin cofactor GimC/prefoldin. *EMBO J* *18*, 6730–6743. 10.1093/emboj/18.23.6730.
66. Siegert, R., Leroux, M.R., Scheufler, C., Hartl, F.U., and Moarefi, I. (2000). Structure of the molecular chaperone prefoldin: unique interaction of multiple coiled coil tentacles with unfolded proteins. *Cell* *103*, 621–632. 10.1016/s0092-8674(00)00165-3.
67. Gestaut, D., Zhao, Y., Park, J., Ma, B., Leitner, A., Collier, M., Pintilie, G., Roh, S.H., Chiu, W., and Frydman, J. (2022). Structural visualization of the tubulin folding pathway directed by human chaperonin TRiC/CCT. *Cell* *185*, 4770–4787 e4720. 10.1016/j.cell.2022.11.014.
68. Hansen, W.J., Cowan, N.J., and Welch, W.J. (1999). Prefoldin-nascent chain complexes in the folding of cytoskeletal proteins. *J Cell Biol* *145*, 265–277.
69. Dekker, C., Stirling, P.C., McCormack, E.A., Filmore, H., Paul, A., Brost, R.L., Costanzo, M., Boone, C., Leroux, M.R., and Willison, K.R. (2008). The interaction network of the chaperonin CCT. *EMBO J* *27*, 1827–1839. 10.1038/emboj.2008.108.
70. Wells, C.A., Dingus, J., and Hildebrandt, J.D. (2006). Role of the chaperonin CCT/TRiC complex in G protein betagamma-dimer assembly. *J Biol Chem* *281*, 20221–20232. 10.1074/jbc.M602409200.
71. Pines, A., Dijk, M., Makowski, M., Meulenbroek, E.M., Vrouwe, M.G., van der Weegen, Y., Baltissen, M., French, P.J., van Royen, M.E., Luijsterburg, M.S., et al. (2018). TRiC controls transcription resumption after UV damage by regulating Cockayne syndrome protein A. *Nat Commun* *9*, 1040. 10.1038/s41467-018-03484-6.
72. Miyata, Y., Shibata, T., Aoshima, M., Tsubata, T., and Nishida, E. (2014). The molecular chaperone TRiC/CCT binds to the Trp-Asp 40 (WD40) repeat protein WDR68 and promotes its folding, protein

- kinase DYRK1A binding, and nuclear accumulation. *J Biol Chem* *289*, 33320–33332. 10.1074/jbc.M114.586115.
73. Roh, S.H., Kasembeli, M., Galaz-Montoya, J.G., Trnka, M., Lau, W.C., Burlingame, A., Chiu, W., and Tweardy, D.J. (2016). Chaperonin TRiC/CCT Modulates the Folding and Activity of Leukemogenic Fusion Oncoprotein AML1-ETO. *J Biol Chem* *291*, 4732–4741. 10.1074/jbc.M115.684878.
 74. Cuellar, J., Vallin, J., Svanström, A., Maestro-Lopez, M., Bueno-Carrasco, M.T., Ludlam, W.G., Willardson, B.M., Valpuesta, J.M., and Grantham, J. (2022). The molecular chaperone CCT sequesters gelsolin and protects it from cleavage by caspase-3. *Journal of molecular biology* *434*, 167399.
 75. Douglas, N.R., Reissmann, S., Zhang, J., Chen, B., Jakana, J., Kumar, R., Chiu, W., and Frydman, J. (2011). Dual action of ATP hydrolysis couples lid closure to substrate release into the group II chaperonin chamber. *Cell* *144*, 240–252. 10.1016/j.cell.2010.12.017.
 76. Geissler, S., Siegers, K., and Schiebel, E. (1998). A novel protein complex promoting formation of functional alpha- and gamma-tubulin. *EMBO J* *17*, 952–966. 10.1093/emboj/17.4.952.
 77. Lewis, S.A., Tian, G., and Cowan, N.J. (1997). The alpha- and beta-tubulin folding pathways. *Trends Cell Biol* *7*, 479–484. 10.1016/S0962-8924(97)01168-9.
 78. Nithianantham, S., Le, S., Seto, E., Jia, W., Leary, J., Corbett, K.D., Moore, J.K., and Al-Bassam, J. (2015). Tubulin cofactors and Arl2 are cage-like chaperones that regulate the soluble alphabeta-tubulin pool for microtubule dynamics. *Elife* *4*. 10.7554/eLife.08811.
 79. Frydman, J., and Hartl, F.U. (1996). Principles of chaperone-assisted protein folding: differences between in vitro and in vivo mechanisms. *Science* *272*, 1497–1502. 10.1126/science.272.5267.1497.
 80. Gao, Y., Thomas, J.O., Chow, R.L., Lee, G.H., and Cowan, N.J. (1992). A cytoplasmic chaperonin that catalyzes beta-actin folding. *Cell* *69*, 1043–1050. 10.1016/0092-8674(92)90622-j.
 81. Stuart, S.F., Leatherbarrow, R.J., and Willison, K.R. (2011). A two-step mechanism for the folding of actin by the yeast cytosolic chaperonin. *J Biol Chem* *286*, 178–184. 10.1074/jbc.M110.166256.
 82. van den Ent, F., Amos, L.A., and LoÈwe, J. (2001). Prokaryotic origin of the actin cytoskeleton. *Nature* *413*, 39–44.
 83. Chapman, E., Farr, G.W., Usaite, R., Furtak, K., Fenton, W.A., Chaudhuri, T.K., Hondorp, E.R., Matthews, R.G., Wolf, S.G., Yates, J.R., et al. (2006). Global aggregation of newly translated proteins in an *Escherichia coli* strain deficient of the chaperonin GroEL. *Proc Natl Acad Sci U S A* *103*, 15800–15805. 10.1073/pnas.0607534103.
 84. Nowak, E., Strzelecka-Golaszewska, H., and Goody, R.S. (1988). Kinetics of nucleotide and metal ion interaction with G-actin. *Biochemistry* *27*, 1785–1792. 10.1021/bi00405a060.
 85. Altschuler, G.M., Klug, D.R., and Willison, K.R. (2005). Unfolding energetics of G-alpha-actin: a discrete intermediate can be re-folded to the native state by CCT. *J Mol Biol* *353*, 385–396.

10.1016/j.jmb.2005.07.062.

86. Kuznetsova, I.M., Stepanenko, O.V., Stepanenko, O.V., Povarova, O.I., Biktashev, A.G., Verkhusha, V.V., Shavlovsky, M.M., and Turoverov, K.K. (2002). The Place of Inactivated Actin and Its Kinetic Predecessor in Actin Folding– Unfolding. *Biochemistry* *41*, 13127–13132.
87. Bertazzon, A., Tian, G., Lamblin, A., and Tsong, T.Y. (1990). Enthalpic and entropic contributions to actin stability: calorimetry, circular dichroism, and fluorescence study and effects of calcium. *Biochemistry* *29*, 291–298.
88. Kuznetsova, I.M., Biktashev, A.G., Khaitlina, S.Y., Vassilenko, K.S., Turoverov, K.K., and Uversky, V.N. (1999). Effect of self-association on the structural organization of partially folded proteins: inactivated actin. *Biophys J* *77*, 2788–2800. 10.1016/S0006-3495(99)77111-0.
89. Kinoshita, H., Selden, L., Estes, J., and Gershman, L. (1993). Nucleotide binding to actin. Cation dependence of nucleotide dissociation and exchange rates. *Journal of Biological Chemistry* *268*, 8683–8691.
90. Rommelaere, H., Waterschoot, D., Neiryneck, K., Vandekerckhove, J., and Ampe, C. (2003). Structural plasticity of functional actin: pictures of actin binding protein and polymer interfaces. *Structure* *11*, 1279–1289. 10.1016/j.str.2003.09.002.
91. Neiryneck, K., Waterschoot, D., Vandekerckhove, J., Ampe, C., and Rommelaere, H. (2006). Actin interacts with CCT via discrete binding sites: a binding transition–release model for CCT-mediated actin folding. *J Mol Biol* *355*, 124–138. 10.1016/j.jmb.2005.10.051.
92. Cuellar, J., Ludlam, W.G., Tensmeyer, N.C., Aoba, T., Dhavale, M., Santiago, C., Bueno-Carrasco, M.T., Mann, M.J., Plimpton, R.L., Makaju, A., et al. (2019). Structural and functional analysis of the role of the chaperonin CCT in mTOR complex assembly. *Nat Commun* *10*, 2865. 10.1038/s41467-019-10781-1.
93. Willardson, B.M., and Howlett, A.C. (2007). Function of phosducin-like proteins in G protein signaling and chaperone-assisted protein folding. *Cell Signal* *19*, 2417–2427. 10.1016/j.cellsig.2007.06.013.
94. Blaauw, M., Knol, J.C., Kortholt, A., Roelofs, J., Ruchira, Postma, M., Visser, A.J., and van Haastert, P.J. (2003). Phosducin-like proteins in *Dictyostelium discoideum*: implications for the phosducin family of proteins. *EMBO J* *22*, 5047–5057. 10.1093/emboj/cdg508.
95. McLaughlin, J.N., Thulin, C.D., Hart, S.J., Resing, K.A., Ahn, N.G., and Willardson, B.M. (2002). Regulatory interaction of phosducin-like protein with the cytosolic chaperonin complex. *Proc Natl Acad Sci U S A* *99*, 7962–7967. 10.1073/pnas.112075699.
96. Lukov, G.L., Hu, T., McLaughlin, J.N., Hamm, H.E., and Willardson, B.M. (2005). Phosducin-like protein acts as a molecular chaperone for G protein betagamma dimer assembly. *EMBO J* *24*, 1965–1975. 10.1038/sj.emboj.7600673.
97. Howlett, A.C., Gray, A.J., Hunter, J.M., and Willardson, B.M. (2009).

- Role of molecular chaperones in G protein beta5/regulator of G protein signaling dimer assembly and G protein betagamma dimer specificity. *J Biol Chem* *284*, 16386–16399. 10.1074/jbc.M900800200.
98. Wilkinson, J.C., Richter, B.W., Wilkinson, A.S., Burstein, E., Rumble, J.M., Balliu, B., and Duckett, C.S. (2004). VIAF, a conserved inhibitor of apoptosis (IAP)-interacting factor that modulates caspase activation. *J Biol Chem* *279*, 51091–51099. 10.1074/jbc.M409623200.
 99. Li, M., Chen, Y., Ou, J., Huang, J., and Zhang, X. (2022). PDCL2 is essential for spermiogenesis and male fertility in mice. *Cell Death Discov* *8*, 419. 10.1038/s41420-022-01210-2.
 100. McCormack, E.A., Altschuler, G.M., Dekker, C., Filmore, H., and Willison, K.R. (2009). Yeast phosducin-like protein 2 acts as a stimulatory co-factor for the folding of actin by the chaperonin CCT via a ternary complex. *J Mol Biol* *391*, 192–206. 10.1016/j.jmb.2009.06.003.
 101. Stirling, P.C., Cuellar, J., Alfaro, G.A., El Khadali, F., Beh, C.T., Valpuesta, J.M., Melki, R., and Leroux, M.R. (2006). PhLP3 modulates CCT-mediated actin and tubulin folding via ternary complexes with substrates. *J Biol Chem* *281*, 7012–7021. 10.1074/jbc.M513235200.
 102. Flanary, P.L., DiBello, P.R., Estrada, P., and Dohlman, H.G. (2000). Functional analysis of Plp1 and Plp2, two homologues of phosducin in yeast. *J Biol Chem* *275*, 18462–18469. 10.1074/jbc.M002163200.
 103. Fei, X., Ye, X., LaRonde, N.A., and Lorimer, G.H. (2014). Formation and structures of GroEL:GroES2 chaperonin footballs, the protein-folding functional form. *Proc Natl Acad Sci U S A* *111*, 12775–12780. 10.1073/pnas.1412922111.
 104. Park, J., Kim, H., Gestaut, D., Lim, S., Leitner, A., Frydman, J., and Roh, S.H. (2023). A structural vista of phosducin-like PhLP2A-chaperonin TRiC cooperation during the ATP-driven folding cycle. *bioRxiv*. 10.1101/2023.03.25.534239.
 105. Liu, C., Jin, M., Wang, S., Han, W., Zhao, Q., Wang, Y., Xu, C., Diao, L., Yin, Y., and Peng, C. (2023). Pathway and mechanism of tubulin folding mediated by TRiC/CCT along its ATPase cycle revealed using cryo-EM. *Communications Biology* *6*, 531.
 106. Ashkenazy, H., Abadi, S., Martz, E., Chay, O., Mayrose, I., Pupko, T., and Ben-Tal, N. (2016). ConSurf 2016: an improved methodology to estimate and visualize evolutionary conservation in macromolecules. *Nucleic Acids Res* *44*, W344–350. 10.1093/nar/gkw408.
 107. Altschuler, G.M., and Willison, K.R. (2008). Development of free-energy-based models for chaperonin containing TCP-1 mediated folding of actin. *Journal of the Royal Society Interface* *5*, 1391–1408.
 108. Villebeck, L., Persson, M., Luan, S.L., Hammarstrom, P., Lindgren, M., and Jonsson, B.H. (2007). Conformational rearrangements of tail-less complex polypeptide 1 (TCP-1) ring complex (TRiC)-bound actin. *Biochemistry* *46*, 5083–5093. 10.1021/bi062093o.
 109. Zivanov, J., Nakane, T., Forsberg, B.O., Kimanius, D., Hagen, W.J.,

- Lindahl, E., and Scheres, S.H. (2018). New tools for automated high-resolution cryo-EM structure determination in RELION-3. *Elife* *7*. 10.7554/eLife.42166.
110. Punjani, A., Rubinstein, J.L., Fleet, D.J., and Brubaker, M.A. (2017). cryoSPARC: algorithms for rapid unsupervised cryo-EM structure determination. *Nat Methods* *14*, 290–296. 10.1038/nmeth.4169.
 111. Zheng, S.Q., Palovcak, E., Armache, J.P., Verba, K.A., Cheng, Y., and Agard, D.A. (2017). MotionCor2: anisotropic correction of beam-induced motion for improved cryo-electron microscopy. *Nat Methods* *14*, 331–332. 10.1038/nmeth.4193.
 112. Zhang, K. (2016). Gctf: Real-time CTF determination and correction. *J Struct Biol* *193*, 1–12. 10.1016/j.jsb.2015.11.003.
 113. Rohou, A., and Grigorieff, N. (2015). CTFFIND4: Fast and accurate defocus estimation from electron micrographs. *Journal of structural biology* *192*, 216–221.
 114. Bepler, T., Morin, A., Rapp, M., Brasch, J., Shapiro, L., Noble, A.J., and Berger, B. (2019). Positive-unlabeled convolutional neural networks for particle picking in cryo-electron micrographs. *Nat Methods* *16*, 1153–1160. 10.1038/s41592-019-0575-8.
 115. Kidmose, R.T., Juhl, J., Nissen, P., Boesen, T., Karlsen, J.L., and Pedersen, B.P. (2019). Namdinator – automatic molecular dynamics flexible fitting of structural models into cryo-EM and crystallography experimental maps. *IUCrJ* *6*, 526–531. 10.1107/S2052252519007619.
 116. Afonine, P.V., Poon, B.K., Read, R.J., Sobolev, O.V., Terwilliger, T.C., Urzhumtsev, A., and Adams, P.D. (2018). Real-space refinement in PHENIX for cryo-EM and crystallography. *Acta Crystallogr D Struct Biol* *74*, 531–544. 10.1107/S2059798318006551.
 117. Adib, R., Montgomery, J.M., Atherton, J., O’Regan, L., Richards, M.W., Straatman, K.R., Roth, D., Straube, A., Bayliss, R., and Moores, C.A. (2019). Mitotic phosphorylation by NEK6 and NEK7 reduces the microtubule affinity of EML4 to promote chromosome congression. *Science signaling* *12*, eaaw2939.
 118. Croll, T.I. (2018). ISOLDE: a physically realistic environment for model building into low-resolution electron-density maps. *Acta Crystallographica Section D: Structural Biology* *74*, 519–530.
 119. Pintilie, G., Zhang, K., Su, Z., Li, S., Schmid, M.F., and Chiu, W. (2020). Measurement of atom resolvability in cryo-EM maps with Q-scores. *Nat Methods* *17*, 328–334. 10.1038/s41592-020-0731-1.
 120. Pettersen, E.F., Goddard, T.D., Huang, C.C., Couch, G.S., Greenblatt, D.M., Meng, E.C., and Ferrin, T.E. (2004). UCSF Chimera—a visualization system for exploratory research and analysis. *J Comput Chem* *25*, 1605–1612. 10.1002/jcc.20084.
 121. Pettersen, E.F., Goddard, T.D., Huang, C.C., Meng, E.C., Couch, G.S., Croll, T.I., Morris, J.H., and Ferrin, T.E. (2021). UCSF ChimeraX: Structure visualization for researchers, educators, and developers. *Protein Sci* *30*, 70–82. 10.1002/pro.3943.
 122. Mirdita, M., Schutze, K., Moriwaki, Y., Heo, L., Ovchinnikov, S., and

- Steinegger, M. (2022). ColabFold: making protein folding accessible to all. *Nat Methods* *19*, 679–682. 10.1038/s41592-022-01488-1.
123. Dey, K.K., Xie, D., and Stephens, M. (2018). A new sequence logo plot to highlight enrichment and depletion. *BMC Bioinformatics* *19*, 473. 10.1186/s12859-018-2489-3.
124. Crooks, G.E., Hon, G., Chandonia, J.M., and Brenner, S.E. (2004). WebLogo: a sequence logo generator. *Genome Res* *14*, 1188–1190. 10.1101/gr.849004.
125. Notredame, C., Higgins, D.G., and Heringa, J. (2000). T-Coffee: A novel method for fast and accurate multiple sequence alignment. *J Mol Biol* *302*, 205–217. 10.1006/jmbi.2000.4042.
126. Hall, B.G. (2013). Building phylogenetic trees from molecular data with MEGA. *Mol Biol Evol* *30*, 1229–1235. 10.1093/molbev/mst012.
127. Finn, R.D., Clements, J., and Eddy, S.R. (2011). HMMER web server: interactive sequence similarity searching. *Nucleic Acids Res* *39*, W29–37. 10.1093/nar/gkr367.
128. Price, M.N., Dehal, P.S., and Arkin, A.P. (2010). FastTree 2--approximately maximum-likelihood trees for large alignments. *PLoS One* *5*, e9490. 10.1371/journal.pone.0009490.
129. Huson, D.H., and Scornavacca, C. (2012). Dendroscope 3: an interactive tool for rooted phylogenetic trees and networks. *Syst Biol* *61*, 1061–1067. 10.1093/sysbio/sys062.
130. Capra, J.A., and Singh, M. (2007). Predicting functionally important residues from sequence conservation. *Bioinformatics* *23*, 1875–1882. 10.1093/bioinformatics/btm270.
131. Waterhouse, A., Bertoni, M., Bienert, S., Studer, G., Tauriello, G., Gumienny, R., Heer, F.T., de Beer, T.A.P., Rempfer, C., Bordoli, L., et al. (2018). SWISS-MODEL: homology modelling of protein structures and complexes. *Nucleic Acids Res* *46*, W296–W303. 10.1093/nar/gky427.
132. Booth, C.R., Meyer, A.S., Cong, Y., Topf, M., Sali, A., Ludtke, S.J., Chiu, W., and Frydman, J. (2008). Mechanism of lid closure in the eukaryotic chaperonin TRiC/CCT. *Nat Struct Mol Biol* *15*, 746–753. 10.1038/nsmb.1436.
133. Kelly, J.J., Tranter, D., Pardon, E., Chi, G., Kramer, H., Happonen, L., Knee, K.M., Janz, J.M., Steyaert, J., Bulawa, C., et al. (2022). Snapshots of actin and tubulin folding inside the TRiC chaperonin. *Nat Struct Mol Biol* *29*, 420–429. 10.1038/s41594-022-00755-1.
134. Punjani, A., and Fleet, D.J. (2021). 3D variability analysis: Resolving continuous flexibility and discrete heterogeneity from single particle cryo-EM. *J Struct Biol* *213*, 107702. 10.1016/j.jsb.2021.107702.
135. Lou, X., Bao, R., Zhou, C.Z., and Chen, Y. (2009). Structure of the thioredoxin-fold domain of human phosphatidylethanolamine transferase. *Acta Crystallogr Sect F Struct Biol Cryst Commun* *65*, 67–70. 10.1107/S1744309108037342.
136. Plimpton, R.L., Cuellar, J., Lai, C.W., Aoba, T., Makaju, A., Franklin, S., Mathis, A.D., Prince, J.T., Carrascosa, J.L., Valpuesta, J.M., and Willardson, B.M. (2015). Structures of the Gbeta-CCT and PhLP1-

- Gbeta-CCT complexes reveal a mechanism for G-protein beta-subunit folding and Gbetagamma dimer assembly. *Proc Natl Acad Sci U S A* *112*, 2413–2418. 10.1073/pnas.1419595112.
137. Wang, S., Sass, M.I., Kwon, Y., Ludlam, W.G., Smith, T.M., Carter, E.J., Gladden, N.E., Riggi, M., Iwasa, J.H., Willardson, B.M., and Shen, P.S. (2023). Visualizing the chaperone-mediated folding trajectory of the G protein beta5 beta-propeller. *Mol Cell* *83*, 3852–3868 e3856. 10.1016/j.molcel.2023.09.032.
 138. Reissmann, S., Parnot, C., Booth, C.R., Chiu, W., and Frydman, J. (2007). Essential function of the built-in lid in the allosteric regulation of eukaryotic and archaeal chaperonins. *Nat Struct Mol Biol* *14*, 432–440. 10.1038/nsmb1236.
 139. Andreu, J.M., Oliva, M.A., and Monasterio, O. (2002). Reversible unfolding of FtsZ cell division proteins from archaea and bacteria. Comparison with eukaryotic tubulin folding and assembly. *J Biol Chem* *277*, 43262–43270. 10.1074/jbc.M206723200.
 140. Erickson, H.P., Anderson, D.E., and Osawa, M. (2010). FtsZ in bacterial cytokinesis: cytoskeleton and force generator all in one. *Microbiol Mol Biol Rev* *74*, 504–528. 10.1128/MMBR.00021-10.
 141. Aylett, C.H.S., and Duggin, I.G. (2017). The Tubulin Superfamily in Archaea. *Subcell Biochem* *84*, 393–417. 10.1007/978-3-319-53047-5_14.
 142. Nogales, E., Wolf, S.G., and Downing, K.H. (1998). Structure of the alpha beta tubulin dimer by electron crystallography. *Nature* *391*, 199–203. 10.1038/34465.
 143. Yutin, N., and Koonin, E.V. (2012). Archaeal origin of tubulin. *Biol Direct* *7*, 10. 10.1186/1745-6150-7-10.
 144. Janke, C., and Bulinski, J.C. (2011). Post-translational regulation of the microtubule cytoskeleton: mechanisms and functions. *Nat Rev Mol Cell Biol* *12*, 773–786. 10.1038/nrm3227.
 145. Skiniotis, G., Cochran, J.C., Muller, J., Mandelkow, E., Gilbert, S.P., and Hoenger, A. (2004). Modulation of kinesin binding by the C-termini of tubulin. *EMBO J* *23*, 989–999. 10.1038/sj.emboj.7600118.
 146. Aldaz, H., Rice, L.M., Stearns, T., and Agard, D.A. (2005). Insights into microtubule nucleation from the crystal structure of human γ -tubulin. *Nature* *435*, 523–527.
 147. Löwe, J., and Amos, L.A. (1998). Crystal structure of the bacterial cell-division protein FtsZ. *Nature* *391*, 203–206.
 148. Duggin, I.G., Aylett, C.H., Walsh, J.C., Michie, K.A., Wang, Q., Turnbull, L., Dawson, E.M., Harry, E.J., Whitchurch, C.B., Amos, L.A., and Lowe, J. (2015). CetZ tubulin-like proteins control archaeal cell shape. *Nature* *519*, 362–365. 10.1038/nature13983.
 149. Hoshino, S., and Hayashi, I. (2012). Filament formation of the FtsZ/tubulin-like protein TubZ from the *Bacillus cereus* pXO1 plasmid. *J Biol Chem* *287*, 32103–32112. 10.1074/jbc.M112.373803.
 150. Wang, Y., Tian, G., Cowan, N.J., and Cabral, F. (2006). Mutations affecting beta-tubulin folding and degradation. *J Biol Chem* *281*, 13628–13635. 10.1074/jbc.M513730200.

151. Miles, M.F., Barhite, S., Sganga, M., and Elliott, M. (1993). Phosducin-like protein: an ethanol-responsive potential modulator of guanine nucleotide-binding protein function. *Proc Natl Acad Sci U S A* *90*, 10831–10835. 10.1073/pnas.90.22.10831.
152. Lolley, R.N., Brown, B.M., and Farber, D.B. (1977). Protein phosphorylation in rod outer segments from bovine retina: cyclic nucleotide-activated protein kinase and its endogenous substrate. *Biochem Biophys Res Commun* *78*, 572–578. 10.1016/0006-291x(77)90217-0.
153. Chen, D.H., Madan, D., Weaver, J., Lin, Z., Schroder, G.F., Chiu, W., and Rye, H.S. (2013). Visualizing GroEL/ES in the act of encapsulating a folding protein. *Cell* *153*, 1354–1365. 10.1016/j.cell.2013.04.052.
154. Fenton, W.A., and Horwich, A.L. (1997). GroEL-mediated protein folding. *Protein Sci* *6*, 743–760. 10.1002/pro.5560060401.
155. Motojima, F. (2015). How do chaperonins fold protein? *Biophysics (Nagoya-shi)* *11*, 93–102. 10.2142/biophysics.11.93.
156. Huecas, S., Canosa-Valls, A.J., Araujo-Bazan, L., Ruiz, F.M., Laurents, D.V., Fernandez-Tornero, C., and Andreu, J.M. (2020). Nucleotide-induced folding of cell division protein FtsZ from *Staphylococcus aureus*. *FEBS J* *287*, 4048–4067. 10.1111/febs.15235.
157. Han, W., Jin, M., Liu, C., Zhao, Q., Wang, S., Wang, Y., Yin, Y., Peng, C., Wang, Y., and Cong, Y. (2023). Structural basis of plp2-mediated cytoskeletal protein folding by TRiC/CCT. *Sci Adv* *9*, eade1207. 10.1126/sciadv.ade1207.
158. Savage, J.R., McLaughlin, J.N., Skiba, N.P., Hamm, H.E., and Willardson, B.M. (2000). Functional roles of the two domains of phosducin and phosducin-like protein. *J Biol Chem* *275*, 30399–30407. 10.1074/jbc.M005120200.
159. Park, J., Kim, H., Gestaut, D., Lim, S., Opoku-Nsiah, K.A., Leitner, A., Frydman, J., and Roh, S.H. (2024). A structural vista of phosducin-like PhLP2A-chaperonin TRiC cooperation during the ATP-driven folding cycle. *Nat Commun* *15*, 1007. 10.1038/s41467-024-45242-x.
160. Russmann, F., Stemp, M.J., Monkemeyer, L., Etchells, S.A., Bracher, A., and Hartl, F.U. (2012). Folding of large multidomain proteins by partial encapsulation in the chaperonin TRiC/CCT. *Proc Natl Acad Sci U S A* *109*, 21208–21215. 10.1073/pnas.1218836109.

Abstract

단백질 접힘(Protein folding)은 세포 내에서 단백질 항상성을 유지하는데 중요한 과정이며, 분자 샤페론(Molecular chaperone)은 올바른 접힘을 보장하는 데 중요한 역할을 한다. 그러나 접힘 과정의 이질성과 복잡성으로 인해 분자 수준에서 단백질 접힘의 화학적 과정을 연구하고 분자 샤페론의 역할을 규명하는 것은 매우 어렵다. 이 연구에서 나는 분자 샤페론인 TRiC/CCT (이하 TRiC)와 그 보조 샤페론(Cochaperone)이 도와주는 단백질 접힘 메커니즘을 구조적으로 조사하는 것을 목표로 하였다. 샤페론인 TRiC가 매개하는 접힘 과정은 크게 세 단계로 나눌 수 있다: 1) 기질 전달 2) 보조 샤페론 협력 3) 기질 접힘. 각 접힘 과정을 *in vitro*에서 재구성한 후, cryo-EM을 통한 이질성 분석을 통해 복합체의 구조적 역학을 규명하였다. 기질 전달 과정에서는 PFD가 TRiC의 중앙 챔버로 기질을 전달한다. 보조 샤페론과의 협력 단계에서는 PhLP2A가 TRiC와 함께 상호작용하며 ATP 의존적 사이클에 따라 큰 위치적 재배치를 겪는다. 마지막으로 기질 접힘 단계에서는 TRiC의 서브유닛(subunit)과 기질 간의 도메인 특이적 상호작용을 통해 기질 접힘 과정을 유도하며, PhLP2A는 TRiC 챔버 내부에서 기질과의 추가적인 상호작용을 통해 접힘 과정에 참여한다. 종합적으로, 이 연구를 통해 TRiC와 그 보조 샤페론의 구조적 역동성을 밝혀내었으며, 기질 접힘 메커니즘에 대한 이해를 높이는 데 기여하였다.

Student Number : 2019-29532